UNIVERSITÀ
DEGLI STUDI
DI PADOVA

Administrative office:
Università degli Studi di Padova

Department:
Physics and Astronomy Galileo Galilei

XXXII series PhD course in Physics

Study of light driven phenomena for optofluidic applications in Lab-on-a-chip platforms in lithium niobate

Coordinator:
Ch.mo Prof. FRANCO SIMONETTO

Supervisor:
Prof. CINZIA SADA
Co-supervisor:
Prof. CHAUVET MATHIEU

PhD Candidate
RICCARDO ZAMBONI

To Gino and Emilio

"Measure what is measurable, and make measurable what is not so."

Galileo Galilei

"What we can do in technology is defined by our tools.
If we want new possibilities we need to create new tools"

Greg Nordin

Abstract

Since the growing interest in Lab-On-a-Chip (LOC) applications, the demand for a high multifunctional and portable devices in order to increase the achievement of complex laboratories analysis on a small size chips. This need pushed the research to integrate in the substrates several tools with different tasks, and consequently, the requirements of the material exploited become rapidly more restricted. In particular, the performances of multiple toolkit device are related to its capabilities of combining and matching stages, thus avoiding any detrimental interferences between the material properties needed for their realization.

During the last 20 years, several materials have been proposed for the combination of different tools on the same device. Only recently our group proposed Lithium Niobate ($LiNbO_3$) as a valid alternative for a monolithic substrate in LOC application. This material is well-known in the field of integrated optics, due to its interesting optical properties, that brought it to be the main component in optical modulators in the telecom devices. The excellent performances in this field can be combined to the microfluidic for the realization of reliable optofluidic stages for LOC application. Moreover, $LiNbO_3$ was demonstrated as a substrate for several micro-manipulation tools, exploiting its further properties, such as photovoltaic tweezers of micro-sized objects, nano-droplets pipetting with pyroelectric induced field, acoustic driven particle transports via piezoelectric generated surface acoustic wave respectively. For these reasons, the merge of all these tools on the same monolithic substrate could represent the optimal improvement to push even further the LOC technology.

This thesis aimed to demonstrate that a multifunctional opto-microfluidic platform can be realized in one monolithic substrate of lithium niobate, achieving properties that can be properly exploited for LOC application. In particular, the attention was focused on combining integrated optics and microfluidics in a unique platform, where light is confined in an optical waveguide and crossed a microfluidic channel allowing for a transmission detection. The realization of microchannel for the coupling with microphotonic structures is presented: so in particular channel configurations, such as droplet generator, are characterized and compared to those achieved with other standard material, in order to show the better performances provided by $LiNbO_3$. In this platform the crucial aspect

was played by the optical quality of the lateral walls of the microfluidic channel in order to guarantee an optimized optical coupling of the integrated optical waveguide and the microchannel. Such an optical grade quality allows for the integration of microchannels with Ti-indiffused waveguide, in an unexplored way alternative to the standards in optofluidics. This optofluidic coupling is performed by crossing the waveguide with an engraved microfluidic channel. This configuration enables the analysis of the transmitted light guided by the first half of the waveguide to the second half of it. The self-aligned geometry allows for the traveling of the light beam from one waveguide (input waveguide) across the channel until it recouples in the other part of the waveguide (output waveguide). This optical transmission signal of the medium inside the channel is exploited for LOC applications, such as optical measurements of the droplet geometrical properties (such as frequency, length, volume), and controlled microfluidic pH titration, which allows for the pH determination and the neutralization of strong acidic or basic solution, and finally as an optical multiplexer actuated microfluidically. In all these applications, the devices showed not only high level of integration and accurate response, but also superior performances than the standard procedures and materials. Moreover, a further tool was integrated to this optofluidic platform: a photovoltaic tweezers, exploiting the lithium niobate capability of photoinducing electric field on its surfaces. These multifunctional stages are proposed for the effectively manipulation of the orientation liquid crystal inside a microchannel, and the consequent polarization control waveguide transmission beam.

Contents

Introduction

The lab-on-a-chip technology is changing the way of doing analysis in several application fields, from biology to chemistry. Like the evolution from phone booths to smartphones changed the concept of communication, the idea of holding a laboratory in our hands is representing a major technological breakthrough. Indeed, the possibility of having a diagnostic tool in our pockets could have a great impact on the life quality in the future. Lab-on-a-chip can be described as a miniaturized device, where multiple tools are synergistic integrated onto a single chip. Like in laboratories, these devices can perform several analyses and operations depending on the tools available.

The development of these devices is driven by the numerous advantages provided by this technology compared to standard ones. Among these, one of the most evident is the compactness of a few centimeters chip in comparison to bulky laboratory instruments, guaranteeing less handling and complex operations and also an improved portability. In parallel to the small sizes, these devices are much more affordable than a laboratory setup, not only in terms of size and cost, but also in terms of reagents consumptions and consumables in general. Moreover, lab-on-a-chips are usually highly automated, thus reducing the eventual sources of human errors. These features make lab-on-a-chips really appealing for several applications, in some of them they even showed superior performances than conventional systems. Actually, the commercialization of devices have been already started for instance for glucose monitoring, HIV detection and heart attack diagnostics and it is clear that this is only the beginning.

Since ″everything that glitters ain't gold″, many lab-on-a-chips still have to be optimized to become commercially available. Efforts are required to achieve a convenient transfer from research laboratories to the hands of people. Most of the promises given by researchers have still to be fulfilled, because of the lack of a reliable synergetic integration of multiple tools on the same substrate. In this framework, this thesis aimed to investigate the possibility of realizing a valuable substrate for lab-on-a-chip application in lithium niobate $LiNbO_3$. This material is well-known for its optical successful applications due to its properties, such as the commercial diffusion of optical modulators in the telecom field and the second harmonic generation devices (i.e. periodic poled lithium niobate PPLN), and recently it has been proposed for interesting micro-manipulation purpose for biological application, such as photovoltaic [1] and pyroelectric tweezers [2, 3], and also acoustofluidic tools by means of surface acoustic waves [4]. Surprisingly, it has been never proposed as a monolithic lab-on-a-chip, despite these burgeoning premises. Indeed, $LiNbO_3$ has never been exploited as a substrate for the integration of a microfluidic circuit, except for recent work published by our group [5–7]. This thesis investigated the combination of all these three tools on the same monolithic substrate of lithium niobate. Firstly, in the following the engraving of microfluidic channels in lithium niobate will be presented exploiting several fabrication methods, evidencing the drawbacks and advantages of each one. The characterization of such a micro channels will be reported and in particular droplet generator circuits in lithium niobate will be compared with standard scaling laws and compared with conventional ones. These fabrication techniques took into account also the possibility of an eventual coupling with standard micro-photonic structures, such as integrated Ti-indiffusion waveguide. This conjunction is also presented in this work, where the fabrication of both z-propagating Ti-indiffused waveguides and micro channels on the same substrate are reported. $5\,\mu m$ waveguide were diffused into a sample of lithium niobate, where afterwards the microchannles were engraved perpendicularly to the propagation direction of the waveguides. The channel crossed the waveguides orthogonally to the light propagation direction, thus dividing the waveguides in two parts. The light from one waveguide travels across the channel interacting with the medium inside it, and finally recouples in the other part. The optical transmission signal is therefore collected and analyzed at the end of the second part of the waveguide output. This optofluidic coupling is completely new configuration and never explored before. Indeed, most of the standard optofluidic devices for lab-on-a-chip applications relies on the fiber embedding [8–13], which presents several fabrication disadvantages, such as alignment and gluing. Although several interesting results have been achieved with these devices in terms lab-on-a-chip applications [14–16], those advantages curb an high parallelization and a reliable commercialization. This technique can be a promising way of the realization an optofluidic device in lithium niobate, avoiding any alignment procedures and exploiting standard fabrication techniques used for MEMS devices. Such an optofluidic platform allows for a transmission optical analysis of the microchannels, and consequently for several interesting optofluidic applications. Among the others, in this work an example of optical trigger for flowing objects in the channel will be given. If the objects flowing inside the channel are droplets, the optical trigger can offer a way for the measurements of droplets volume, frequency and lengths. An improvement of the waveguides design, made of a single or parallel array of independent waveguides, has been achieved by realizing a Mach Zehnder interferometer configuration. This in fact enables the detection of the flowing object velocities illuminating the channel with two reference points instead of just one. The measurements of flowing objects properties in a integrated device represents a valid alternative to standard imaging systems such as microscopes and cameras. This feature is fundamental for removing the chip out of the laboratories and also in some cases this device can provide superior performance and high versatility due to the local probing. Another application, showed for the first time in this work, is the pH titration, which is a technique used for the pH measurements and the neutralization of high acidic or basic solutions, exploiting the abrupt optical absorbance transition of peculiar molecules, called pH indicator. The device provides a dynamic measurements of this optical property inside a microchannel by the transmission optical signal from the waveguide, and also high durability thanks to the high chemical resistance of lithium niobate.

Finally, a third stage has been integrated in the $LiNbO_3$ device, implementing with an iron doped lithium niobate cover, which allows for the generation of photoinduced electric charge inside the channel. This manipulation stage is demonstrating to actuate matters inside the microfluidic channel, in particular in this work Liquid Crystals orientation inside the microfluidic channel was simultaneously monitored by the optofluidic system and actuated by means of the photoinduced electric field.

The topics herein presented are divided in the following chapters:

Chapter 1 discusses the potentialities of optofluidic in lab-on-a-chip applications, taking into account the contribution that lithium niobate can provide. In particular, this chapter describes briefly the material and its properties, evidencing the recent results in manipulation stages.

Chapter 2 proposes how microfluidic droplet generators can be realized, from their fabrication to their performances. Each step is described in details: the state of the art of micro machining techniques in lithium niobate, pointing out the major advantages of each in the realization of microchannels, the sealing procedures, the functionalization of the channels, and finally, the characterization of T-junction and cross-junction configuration for droplet production, and their comparison with theoretical scaling laws and other materials devices.

Chapter 3 aims to show the optofluidic lithium niobate device, and in particular how waveguides structures can be integrated in a lithium niobate microfluidic chip. Moreover, all the optical characterization of the waveguide are described with and without the channels.

Chapter 4 describes the optofluidic coupling in lithium niobate platforms exploited for several applications. Among the others, the device is presented as a reliable substitution of a microscope setup, measuring several properties of objects flowing inside the microchannel. Also the material showed good performances as a optical multiplexer actuated microfluidically and for the pH titration.

Chapter 5 presents a photovoltaic tweezing stage integrated in the optofluidic platform. The iron doping of the lithium niobate cover of the device enhances the photovoltaic properties. The doping procedure is described and in particular the physical principle behind the photoinducing of electric fields. Finally, the capabilities of this device are showed in the application on liquid crystals controlled orientation inside the microchannel.

Chapter 1

Lithium niobate as a valuable substrate for lab-on-a-chip applications

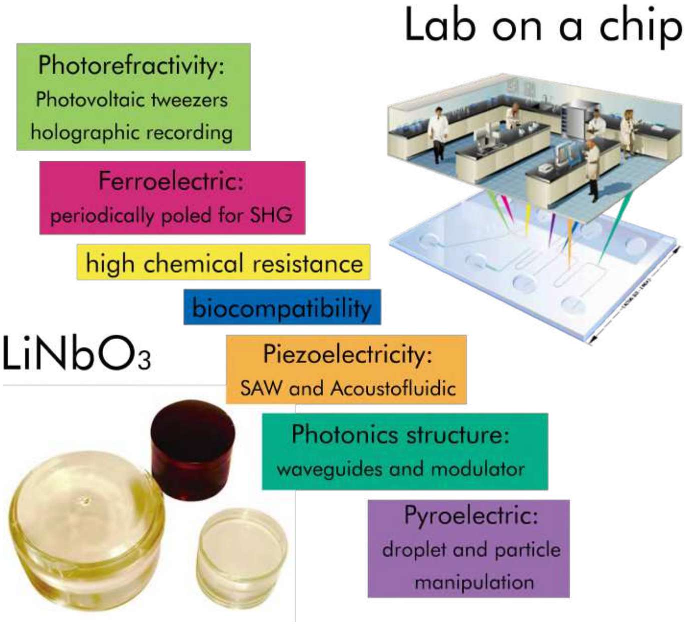

Figure 1.1. Some of the properties which make $LiNbO_3$ *an optimal candidate for the realization of multiple stages lab on a chip.*

Since its discovery, lithium niobate $LiNbO_3$ is one of the most exploited material as a substrate for photonics devices [17]. Its success was gained by large variety of optical properties [18], which allow for realizing platforms useful in a wide applications range. This material, recently, attracted the attention of researchers belonging to other scientific areas, in particular for optofluidic applications [7, 19–21]. The combination of its well-known optical properties with the microfluidic tools can pull the trigger for prosperous development of new $LiNbO_3$ devices exploiting its potentialities (figure 1.1). These chips could not only take advantages of the optical integration of different micro photonic structures on this material, but also of the recent demonstration of tools for liquid manipulation based on piezoelectric [4], photovoltaic [22] and pyroelectric properties [23]. Optofluidics fast development, indeed, has carried to the realization of several lab-on-a-chips, which require the integration of multiple stages on the same compact substrate. This feature can be satisfied by a monolithic $LiNbO_3$ substrate by the synergistic conjunction of all the characteristic previously described. In this context, this thesis aims to give a demonstration of these possibilities. In particular, this chapter will give a brief review of each key point, that pushed for a lab-on-a-chip realized in a monolithic substrate of $LiNbO_3$:

1.1 the first section of this chapter is dedicated to highlight the newborn field of optomicrofluidic, and its powerful tools provided for lab-on-a-chip application;

1.2 in this second section a complete overview of the $LiNbO_3$ properties is given;

1.3 finally, in this last section some key applications of this material in lab-on-a-chip systems are described.

1.1 Optofluidics: an emerging field

”Optofluidics” is recently attracting a growing interest by the scientific community, as demonstrated by the surge of citations in scientific publications since 2005 (figure 1.2). The introduction of this term in a scientific paper was in 1985 by Jones [24], where the author described a fiber optics based sensor including the control of pneumatic valves. However, only 20 years later the publications with this term started to have a considerable increase with the simultaneous burgeoning development of lab-on-a-chip and microfluidics (figure 1.2).

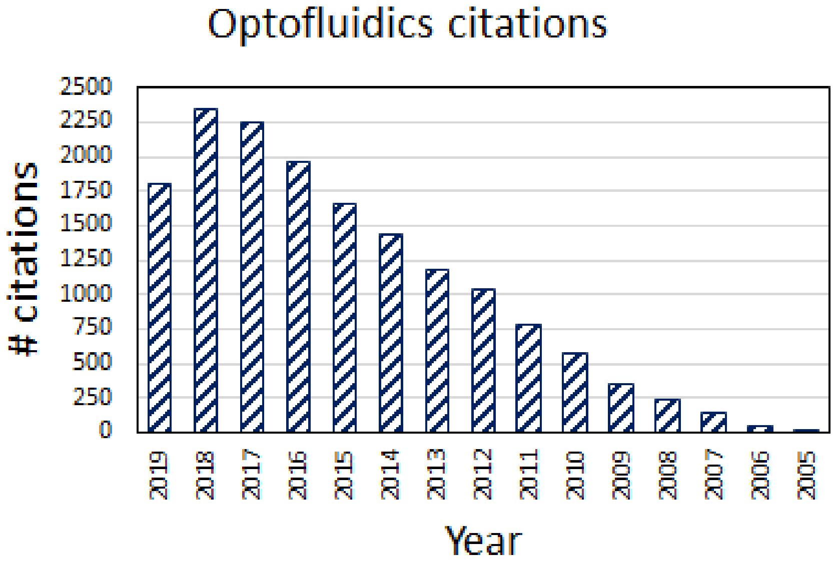

Figure 1.2. Optofluidics publications for each year. The data were taken from web of science.

Several definitions have been given for Optofluidics such as ”the marriage between optics and fluidics” [25] or ”the combination of the integrated optical and fluidic components in the same miniaturized system” [26], but the field is still evolving due to its dynamic and multidisciplinary nature. The optofluidic devices and applications rely on the synergistic conjunction of Microfluidics and Optics components. The mutual interaction between these two technologies offers to the optical applications an unexplored reconfigurability [27], thanks to nature of fluids media, and to the microfluidic an incomparable optical toolkit [28], such as probes or manipulation tools. This combination represented a technological breakthrough in both fields and opened for a development of a large variety of devices with different applications [25, 29]: thanks to the advantages provided by the integration of both optical and microfluidic stages on the same chip. One class of devices exploited the microfluidic tools as a new versatile mechanism for the optical integrated platform [14, 30]. Indeed, microfluidic stages have the ability to change the optical properties of the fluid medium in reliable and fast way, by the replacement of one fluid, or the control of the interface between two fluids. Among the others, the most successful integrations of microfluidic for optical application are: the micro-optofluidic lenses [31], where micro lenses properties are controlled by the liquids ones; optofluidic laser [32]; reconfigurable liquid waveguides [33], where the liquids with different index of refraction are manipulated to confine light in the desired directions; and optofluidic controlled photonic band gap structure [34].

Furthermore, the development of optofluidic devices gave a technological boost to the lab-on-a-chip performances [35, 36] and micro total analysis system [37, 38] for the realization of novel integrated platforms with application in chemical synthesis, biotechnology, and analytical chemistry. The increasing development of optofluidic was concomitantly with the emerging of lab-on-a-chip technology, due to the capabilities provided by this optical and microfluidic merge. Many of the current works and efforts in optofluidic are focused in integrating the optical devices that are usually implemented in biological and chemical detection schemes (like optical light sources and photodetectors) onto compact and planar optofluidic platforms [39]. A broad range of novel optofluidic based lab-on-a-chip paved the way for high functionality degree devices, such as integrated flow cytometers [15, 16]. In parallel, the introduction of optofluidic allows for an extension of the application range of lab-on-a-chip concept in other areas never explored before (figure 1.3), such as in energy field [40, 41].

The toolkit provided by the optofluidics to lab-on-a-chip applications represents an invaluable technological breakthrough, among them one of the most exploited and successful class are the optically controlled photonic devices for the manipulation of microscale dielectric objects. The Nobel prize in 2018 to the pioneering work of Arthur Ashkin on the exploitation of optical forces for the manipulation of particle [42] and single cells [43], gave the evidence of this success. From those forerunner works, the development of such manipulation stages achieved never reached levels of control [44], such as optical tweezers [45, 46], optical sorters [47], optical stretchers [48] and optical driven pumps [49].

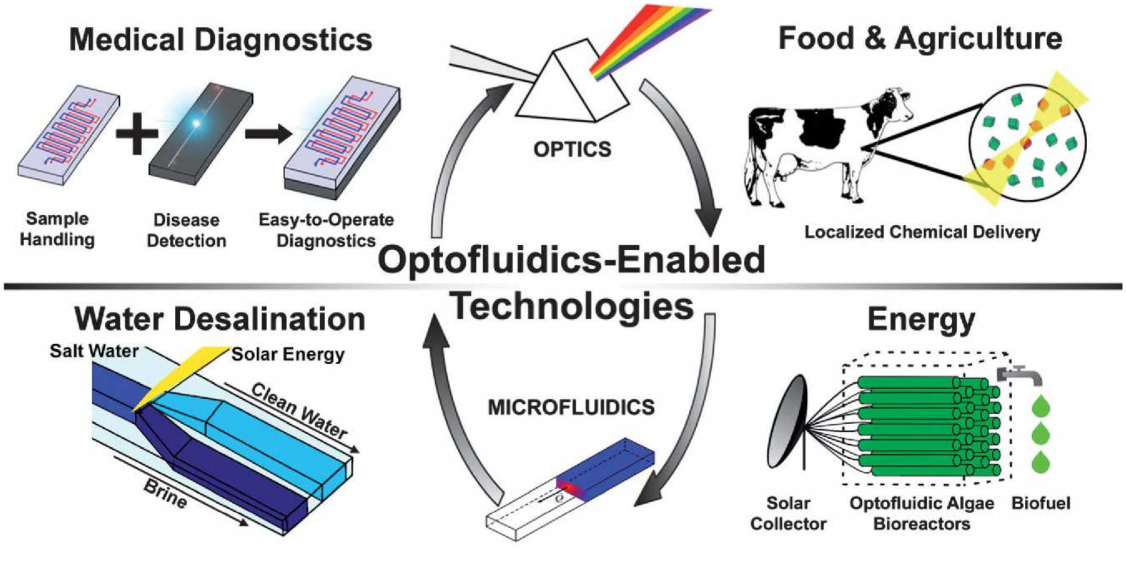

Figure 1.3. Diagrams of actual application of the combination of optical and microfluidic tools on the same substrate. Image is taken from [41].

The cited applications and devices are only the first successful results obtained during this last 10 years. The possibilities of this newborn field are limitless thanks to the burgeoning microfluidic and optical technology. Moreover, the combination of different material and fabrication technique will open even more the already wide range of optofluidic application devices. Among the others, $LiNbO_3$ represents an interesting substrate for new developments, due to its multiple properties.

1.2 Lithium niobate properties

Lithium niobate ($LiNbO_3$) is an artificial ferroelectric crystal, synthesized for the first time by Zacharisen in 1928 and then widely investigated in Bell Laboratories 20 years later. It belongs to compound classes of the pseudo-binary system Li_2O-Nb_2O_5. Figure 1.4 shows the phase diagram of this system: the variability in lithium niobate composition in solid solution, in particular for $T > 1150\,°C$ it ranges for $6\,\mathrm{mol\%}$. The maximum of the liquid-solid line corresponds to the *congruent composition* (Li:Nb=48.5), corresponding to a lithium deficiency compared to the stoichiometric composition ($50\,\mathrm{mol\%}$ Li_2O). At its congruent composition, solid and liquid phases present the same Li:Nb ratio. For this reason, a uniform growth by standard Czochralsky technique is only achievable in congruent composition.

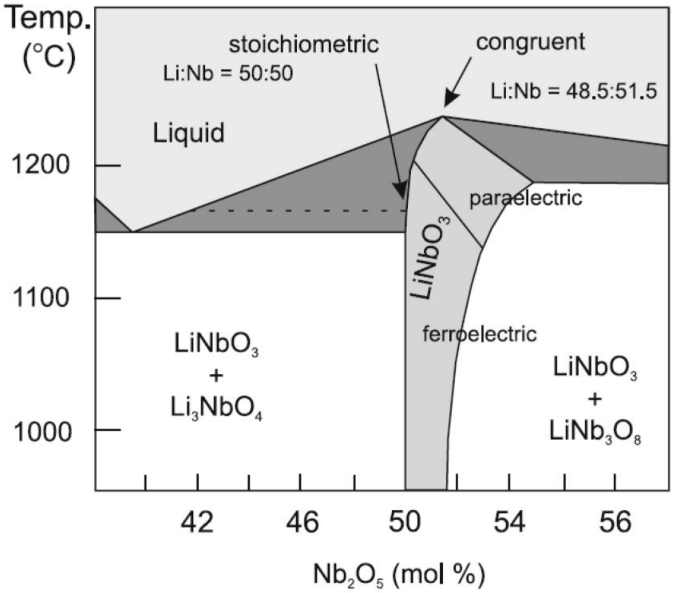

Figure 1.4. Phase diagram of the Li_2O-Nb_2O_5 pseudo-binary system [50].

The ferroelectric nature of the crystal affects directly its structure (figure 1.5): lithium, niobium sites change positions respect to the oxygen atoms accordingly if the temperature is higher or lower than Curie's Temperature ($T_c \simeq 1140\,°\mathrm{C}$). Oxygens are distributed in a planar sheets in a slightly distorted hexagoal close-packed configuration. The octahedral interstices formed by the oxygen are equally filled by lithium, niobium and vacancy. In the paraelectric phase, above T_c, Li ions are aligned with the oxygen plans, niobiums are instead in the middle of the octahedras and the material does not exhibit polarity. While a spontaneous polarization switches below T_c in the ferroelectric phase, where Li ions move $44\,\mathrm{pm}$ in the direction orthogonal to the oxygens planes, in the same direction Nb ones moves to the $27\,\mathrm{pm}$ respectively.

In particular, in the ferroelectric phase this material belongs to trigonal space group *R3c*, with point *3m*. Indeed, it exhibits a mirror symmetry about three planes, that are $60°$ apart perpendicular to the oxygens planes, and it presents a three-fold rotation symmetry around the axis obtained by intersection between the three planes. There are three different cells describing the $LiNbO_3$ crystal structure: rhombohedral, hexagonal and orthohexagonal. Among them, the most widespread one is the orthohexagonal. Tensors components of the material prop-

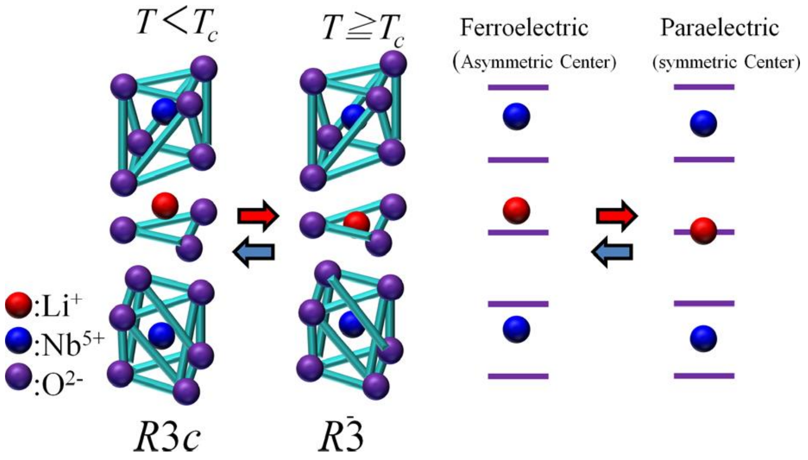

Figure 1.5. Structure of lithium niobate in the two phases. The horizontal purple lines on the right represent the oxygens planes.Image taken from [51]

erties follow usually the three axis *x*,*y*,*z* of this cell. The three axes are orthogonal and *z*-axis, or also called *c*-axis corresponds to the intersection between the three symmetry planes.

1.2.1 Physical properties

The peculiar structure of Lithium niobate brings out a lot of physical properties. In particular, its optical unique features make it a well-known and widely exploited material in the field of optics. Pure material is almost transparent in the spectral region from $0.35\,\mu\mathrm{m}$ to $5\,\mu\mathrm{m}$. In the standard orthohexagonal cell reference framework, the permittivity tensor points out its birefringence:

$$\bar{\bar{\epsilon}} = \begin{bmatrix} \epsilon_{11} & 0 & 0 \\ 0 & \epsilon_{11} & 0 \\ 0 & 0 & \epsilon_{33} \end{bmatrix} \tag{1.1}$$

where the two indices of refraction follows: the ordinary $n_o = \sqrt{\frac{\epsilon_{11}}{\epsilon_0}}$, that is the index of refraction seen by light polarized in any direction perpendicular to the c-axis, and the extraordinary $n_e = \sqrt{\frac{\epsilon_{33}}{\epsilon_0}}$ seen by c-axis polarized light. Both indices depend strongly on extrinsic impurities, and this feature makes lithium niobate a flexible optical material with tailored properties. As optical material, the dispersion relationship of both index of refraction can be approximated by the Sellmeier equation. The accuracy depends on the range of the wavelength and the composition respectively. The most used approximation is the following [52]:

$$\begin{aligned} n_i^2 =& \frac{50 + C_{Li}}{100} \frac{A_{0,i}}{(\lambda_{0,i} + \mu_{0,i} F)^{-2} - \lambda^{-2}} \\ &+ \frac{50 - C_{Li}}{100} \frac{A_{1,i}}{(\lambda_{1,i} + \mu_{1,i} F)^{-2} - \lambda^{-2}} + A_{UV} - A_{IR,i}\lambda^2 \end{aligned} \tag{1.2}$$

$$\begin{aligned} F =& f(T) - f(T_0) \\ f(T) =& (T + 273)^2 + 4.0238 \cdot 10^5 \left[\coth\left(\frac{261.6}{T + 273}\right) - 1\right] \end{aligned}$$

where $T_0 = 24.5\,°\mathrm{C}$, λ is in nanometers, C_{Li} is the composition of $\mathrm{LiO_2}$ expressed in $mol\%$ and $i = (o, e)$ is related to refractive index. The approximation has an accuracy of 0.005 in index of refraction for a range of $47{:}50\,\mathrm{mol\%}$ in Li concentration, of $400{:}1200\,\mathrm{nm}$ for wavelength and $50{:}600\,\mathrm{K}$. An example of the constant for the Sellmeier equation is reported in table 1.1 for $\lambda = 632.8\,\mathrm{nm}$ and at room temperature.

Parameter	**Ordinary**	**Extraordinary**
A_0	$4.5312 \cdot 10^{-5}$	$3.9466 \cdot 10^{-5}$
λ_0	223.219	218.203
A_1	$2.7322 \cdot 10^{-5}$	$8.3140 \cdot 10^{-5}$
λ_1	260.26	250.847
A_{IR}	$3.6340 \cdot 10^{-8}$	$3.0998 \cdot 10^{-8}$
A_{UV}	2.6613	2.6613
μ_0	$2.1203 \cdot 10^{-6}$	$7.5187 \cdot 10^{-6}$
μ_1	$-1.8275 \cdot 10^{-4}$	$-3.8043 \cdot 10^{-5}$
n	**2.2866**	**2.2028**

Table 1.1. Values of fitted parameters for the Sellmeier equation [52] (A_0 for Nb on Nb site, A_1 for Nb on Li site, A_{UV} for high energy oscillators like plasmons, A_{IR} for phonons, μ are the temperature coefficients). The two indices of refraction are the values obtained at room temperature for a wavelength of $\lambda = 632.8\mathrm{nm}$.

Electro-optic effect

Both indices of refraction of the material can be modified by applying an electric field. The effect is described by a variation in the second order tensor $\Delta\left(\frac{1}{n^2}\right)_{ij}$:

$$\Delta\left(\frac{1}{n^2}\right)_{ij} = \sum_k r_{ijk}E_k + \sum_{k,l} s_{ijkl}E_kE_l + \dots \tag{1.3}$$

the two tensors r_{ijk} and s_{ijkl} depend on the material, i.e. structure and they refer to the linear or quadratic behavior of the material, usually called *Pockels* and *Kerr-effect*, respectively. Lithium niobate exhibits only the Pockels effect and the Pockels' tensor can be simplified, due to its symmetric structure, as follows:

$$r = \begin{bmatrix} 0 & -r_{22} & r_{13} \\ 0 & r_{22} & r_{13} \\ 0 & 0 & r_{33} \\ 0 & r_{42} & 0 \\ r_{42} & 0 & 0 \\ -r_{22} & 0 & 0 \end{bmatrix} \tag{1.4}$$

where the values of the coefficients are showed in table 1.2

r_{13}	$8.6 \cdot 10^{-12}\,\mathrm{m\,V^{-1}}$
r_{22}	$3.4 \cdot 10^{-12}\,\mathrm{m\,V^{-1}}$
r_{33}	$30.8 \cdot 10^{-12}\,\mathrm{m\,V^{-1}}$
r_{42}	$28.0 \cdot 10^{-12}\,\mathrm{m\,V^{-1}}$

Table 1.2. Values of coefficients of the Pockels' tensor r, data taken from [53]

The combination of these properties and the waveguide made the material be really interesting since early 1970 for the modulator application, especially in the telecom spectral range [54].

Pyroelectric effect

The peculiar structure of lithium niobate is really sensitive to the temperature, as long as the position of Li and Nb sites are temperature dependent. The spontaneous polarization (ΔP) of the material changes accordingly with temperature

(ΔT):

$$\Delta P = \hat{p}\Delta T \quad \text{with} \quad \hat{p} = \begin{pmatrix} 0 \\ 0 \\ p_3 \end{pmatrix} \tag{1.5}$$

where $p_3 = -4 \cdot 10^{-5}\ \mathrm{C\,m^{-2}\,K}$ [55] and $\hat{p}$ is called the pyroelectric tensor. As expected, the only non-negligible component is the one corresponding to the direction where Li and Nb can easily shift respect to the paraelectric phase.

Piezoelectric effect

The spontaneous polarization $\vec{P}$ can also change by applying a stress. It emerges that (considering the orthogonal cell system):

$$P_i = \sum_{j,k} d_{ijk}\sigma_{jk} \quad \text{with} \quad d = \begin{bmatrix} 0 & 0 & 0 & 0 & d_{15} & -2d_{22} \\ -d_{22} & d_{22} & 0 & d_{15} & 0 & 0 \\ d_{31} & d_{31} & d_{33} & 0 & 0 & 0 \end{bmatrix} \tag{1.6}$$

where P_i is the induced polarization in the i direction, σ_{jk} is the stress tensor and d_{ijk} is the piezoelectric one, which has only 4 independent components, due to the LiNbO$_3$ symmetry. The tensor d describes also the converse effect: i.e. the crystal shows a strain under the application of an external electric field.

Photovoltaic effect

The non-centrosymmetric structure leads typically to a photovoltaic effect, that is the current from the electrons excited from absorbing center in the material by way of optical interaction, and their movement to the neighboring ions in a preferential direction. The photovoltaic effect in LiNbO$_3$ was discovered in 1974, observing a stationary current in the material exposed to light [56]. This current is proportional to the light intensity,the absorption coefficient and to the wavelength:

$$j_{phv,i} = \beta_{ijk} e_j e_k^* I = \alpha k_{G,ijk} e_j e_k^* I \tag{1.7}$$

where β_{ijk} is the complex photovoltaic tensor ($\beta_{ijk} = \beta_{ijk}^*$), e is the versor of the light field.

Photorefractive effect

The combination of electro-optic and photovoltaic effects leads the material to exhibit the peculiar mechanism of photorefractivity. This phenomenon consists in the change of the index of refraction of a material exposed to light illumination. This effect was originally called optical damage, since it leads to defocussing effects in a propagating light beam, either detrimental results especially in the collimation of laser beam. However, after the discovery of optical holography in 1962 [57], the capability of this effect was recognized. In fact if the material is illuminated by a non-uniform pattern of light, the photoinduced carries can freely move in the material. These carriers can be trapped in the interbands levels, like intrinsic or extrinsic impurities, resulting in a non uniform charge distribution, which leads to the rising up of an internal space-charge electric field. This photoinduced electric field modulates consequently the index of refraction by means of the electro-optic effect. The key role in observing this effect is therefore played by donor and acceptor centers in the material.
In lithium niobate the niobium antisite has the double role of donor state, since Nb^{4+} acts as a donor state and Nb^{5+} as a acceptor state. Indeed, it is crucial the presence of intrinsic or extrinsic impurities with two valence states for photorefractivity. One of the most common doping to enhance the effect is iron with the two states Fe^{2+} as a donor and Fe^{3+} as an acceptor.

1.3 Lithium niobate in lab-on-a-chip applications

The introduction of lithium niobate in lab-on-a-chip devices was driven by the needs of simple and efficient micro-manipulation stages. Three main stages in $LiNbO_3$ were mainly exploited: photovoltaic tweezers [23], pyroelectric tweezers [22] and surface acoustic waves (SAW) system [4]. The first one relies on the photoinduction of electric field by means of the photoexcitation of electrical carrier in iron doped lithium niobate (1.6), due to its outstanding photovoltaic properties. In this scenario, the field pattern is related to the light pattern, thus the limitations of the tweezers are limited to the light pattern resolution. These stages were demonstrated to manipulate either charged or neutral particles by dielectrophoretic or electrophoretic forces, respectively, but also with droplet (even water droplet [58]) and biological samples [1]. The photovoltaic tweezers was reported to effectively sorting bubbles in a microfluidic Y-junction channel realized in a hybrid Fe:$LiNbO_3$-PDMS device [21].

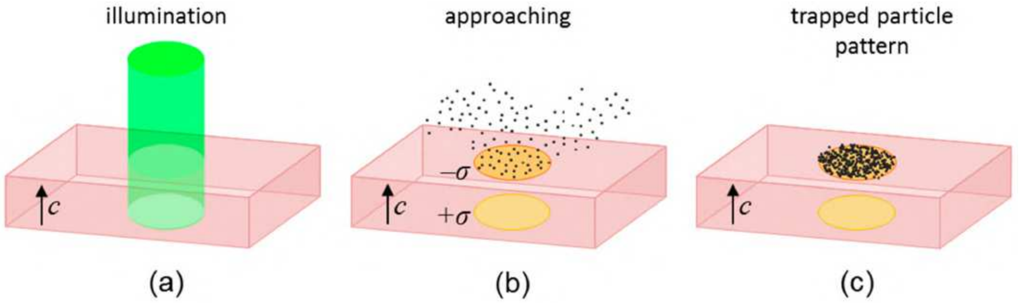

Figure 1.6. Working principle of PT: a) the electric field are photoinduced by an illumination pattern, b) the particle interact with the electric field either by dielectrophoresis or electrophoresis, and finally c) they are trapped. Image is taken from [23].

The same electric field pattern can be obtained by the exploitation of pyroelectric effect, in this case a thermal treatment allows for the generation of an electric field pattern, determined by the geometry of material poling domain (figure 1.7)

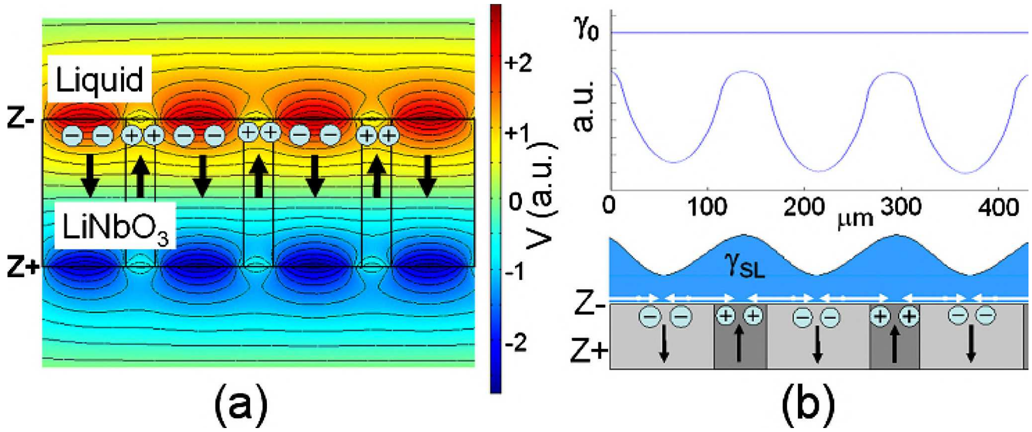

Figure 1.7. Working principle of Pyroelectric electric field pattern generation, the pattern in this case is defined by the poling domains instead of light pattern. Image is taken from [3].

The reported applications were similar to the photovoltaic tweezers, particle trapping by electro and dielectrophoresis, in addition electrowetting actuated micro lenses [19] and nano pico-droplets pipetting were achieved exploiting lithium niobate [2, 59].

The effective manipulation of particles can be achieved also with the acoustic wave generated by electrodes on a piezoelectric substrate [60] like $LiNbO_3$. These systems were reported in many lab-on-a-chip devices [61, 62]: for mixing applications in microfluidic channel [63], for droplets transport [64], for manipulation of micro-objects [65, 66] and for pumping applications [67]. The working principle is based on the generation of pressure waves by means of voltage variations on electrodes deposited on piezoelectric substrate: these waves travel on the substrate surfaces and interact with object desired. In several application the $LiNbO_3$ were coupled with PDMS microfluidic structure [64].

Chapter 2

Microfluidics in $LiNbO_3$ devices: a new perspective

The integration of a microfluidic stage is crucial for almost every applications of lab-on-a-chip, since many of biological and chemical application have liquid analytes. The realization of microfluidic channel in $LiNbO_3$ is the first step to reach levels of integration further beyond to particle manipulation presented in the previous chapter. The achievements of a reliable way to produce microchannels on $LiNbO_3$ could open to the powerful combination of large toolkit on same substrate, exploiting all the aforementioned properties of the material.
Such an integration could be obtain only if a core microfluidic stages can be realized and coupled with others, and recently our group presented some examples [5–7], a picture of the system is given in figure 2.1.

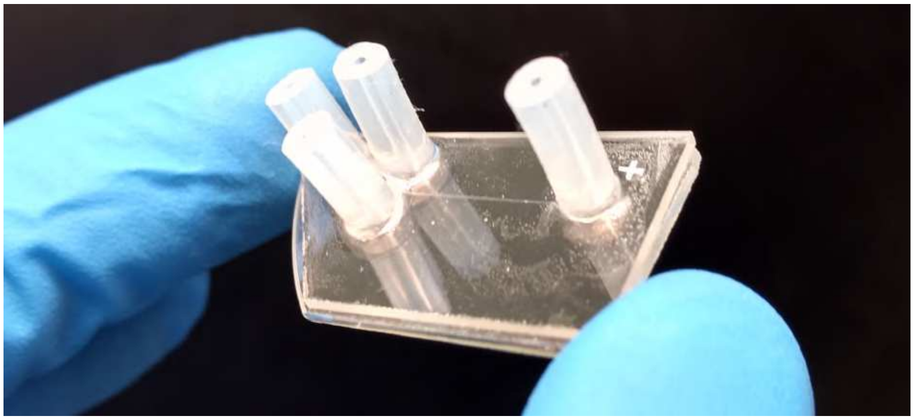

Figure 2.1. the picture report an example of a lithium niobate chip, where a droplet generator circuitry is engraved by mean of a self-polishing saw technique, as described in [7].

In this chapter an overview of possible solution for the realization fo micrometer sized microchannel on $LiNbO_3$ is reported, evidencing the possible integration with other stages.

Among the possible microfluidic circuits that can be realized, this thesis demonstrated the realization of a droplet generator. It is a peculiar microfluidic structure, that allows for the realization of small volume (i.e. droplet) of the so called dispersed phase isolated and surrounded by the so called continuous phase. The achievements of such complex microfluidic circuit is necessary goal for lab-on-a-chip application, since droplet microfluidics is a crucial technology for several applications [68, 69]. Indeed, each single droplets represent an isolated environment, which can be easily controlled, merged and separated. These features make droplets as perfects carriers for biological sample or chemical reactors, improving the safeness, control and the throughput of analysis and operations. Moreover, the droplet microfluidic is one of the best solution for mixing, in fact the flow profile inside a droplet moving along a channel promotes the mix of the liquid inside it, on the contrary in one phase microfluidic where the flow is always laminar.

In this chapter two droplet generators in $LiNbO_3$ substrates will be described, their fabrication steps by steps and then their performances:

2.1 in this section a state of the art of microfabrication techniques is presented, then a deeper investigation is proposed for the self-polishing engraving, which is the technique used for the samples of this work. An overview on the sealing procedures followed is also given, and finally the wettability and the functionalization of the channel is discussed.

2.2 At the beginning of this section there is a description of all different technique for droplet generation in microfluidic. Secondly, this work focuses on two possible passive configurations: the T-junction and the cross-junction. For the first one, the theory behind the scaling law typically used for this configuration is provided together with the experimental setup and the results, which are already published in [6]. The same is made for the second case: discussion of data and acquisition system were here tested more in detail, since the results are completely new and unpublished.

2.1 Microfluidic circuit fabrication in lithium niobate

2.1.1 State of the art

Microfabrication technique has been always being a crucial step in the development of new devices both for photonics and lab-on-a-chip application. In particular, lithium niobate micromachining typically requires big efforts, since this material has strong chemical resistance, it is anisotropic, highly pyroelectric and presents low toughness. This hard manipulation made $LiNbO_3$ used traditionally as an inert substrate integrated with other material as it presented in the section 1.3. However, its machining could open new unexplored possibilities in the realization of versatile lab-on-a-chip exploiting its superior physical, optical and electronic properties, and also could increase the efficiency of the well-known application of this material in this field. Depending on the structure to realize, each technique can have several advantages. As a matter of fact the removal rate, the surface quality and the resolution can vary significantly on the technique used for the microfabrication.

Lots of efforts were done with laser ablation technique on lithium niobate using both micro and nanoseconds pulsed laser [70], and femtosecond laser [71, 72]. This latter improved significantly the process, since it reduces the redeposition due to ultrashort lasing pulses. Laser ablation techniques have a huge advantages in their flexibility, basically any kind of three dimensional structure can be realized and in the literature both microfluidic [6] and photonics [73] structure were realized with this technique. However, this process suffers from low removal rate and most of the time it needs an extra HF bath to remove the imperfections. This drawback limits the application of this technique to the realization of microfluidic structure without any optical stage integration, due to the poor quality of the surfaces. Indeed, after the laser ablation a thin amorphous layer usually characterized the surface [74], which compromises any optofluidic coupling with microchannels. Nevertheless, the flexibility on the structure and the resolution of this technique make it be widely exploited for applications requiring a particular design, with finely tuned and resolved feature.

Similarly to the laser ablation, focused ion beam (FIB) milling suffers from low removal rate, since the aspect ratio of the structure slows the removal rate [75]. This technique is suitable only for low aspect ratio structure. Higher removal rate can be achieved using deep reactive ion etching (DRIE), thanks to the fact that the sample is both chemically etched by the plasma ions and bombarded by the directional ions accelerated by a DC bias [76]. However, this technique requires a previous photolitography process in order to define the structure geometry. All these steps make DRIE expensive and long, thus not flexible and not suggested for any prototyping.

Although all the aforementioned techniques have been successfully demonstrated for the realization of several different applications, their drawbacks, such as the low removal rate, do not allow an effective realization of the microstructured channel of the order of 100 µm. Such dimensions can only be achieved by means of mechanical micromachining. Three main techniques were reported for the milling of $LiNbO_3$: microdrilling [77], microengraving [78, 79] and microcutting [6]. The first one consists in a CNC machine in combination with a tool of 0.5 mm diameter cubic boron nitride square end mill. It works as a microdriller, and it achieved at best a roughness greater than 500 nm. The second one is the engraving of structure exploiting a single crystal diamond tool. Even if this technique obtained at best a roughness of 10 nm, it is only feasible for small depth cut lower than 100 µm. Nevertheless for photonics structure, such as ridge waveguide, this technique leads to good quality and flexible structure waveguides [79, 80]. The last one consists in the realization of controlled cuts on the lithium niobate samples using a CNC saw. This technique is optimal for the realization on microfluidic channel for optofluidic application such as droplet optical trigger [7] or polarization separators [81] or index of refraction sensor [20]. Since this technique is the one used for the realization of the samples of this work, it is described in details in the next section.

2.1.2 Self-polishing saw

The microchannels of this work are all realized with the same machine DISCO DAD 3350 precision saw (Disco Corporation, Tokyo, Japan), in collaboration with Femto-St Institute and University of Franche-Comté in Besançon. The machine can be equipped with different blade depending on the material to cut. Several study have been done by our group in [6], where the machine was equipped with a polymeric blade coated with diamond particle with 56 mm of diameter and 200 µm of thickness. The best surface quality was achieved with a rotation speed of 10 000 rpm. In the following only the best performing results will be presented, excluding the discussion of all the systematic work performed to achieve the best preparation condition. Both optical microscopy and atomic force microscope (AFM) measurements were done to check the quality of the edges and to measure the roughness. The images in 2.2 show sharp edges, even in corners of the cross which is the most stressed part. The bottom part, instead, presents the typical sinusoidal pattern of few microns due to the blade cut, however for the later presented optofluidic applications only the roughness of the side wall are matter of concern.

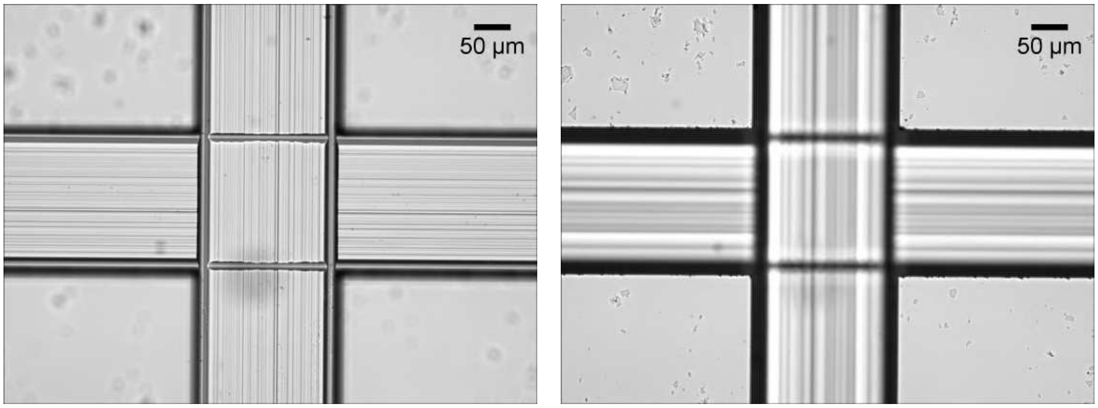

(a) Bottom view (b) Top view

Figure 2.2. Image of the engraved cross junction taken with an inverted microscope Nikon Ti-E with a plan 10x/0.10 objective. On the left bottom surfaces are focused, while on the right the edges.

The Roughness R was measured sampling areas of $10\text{x}10\,\mu\text{m}^2$ across the surface by means of a Veeco CP-II atomic force microscope (AFM, Camarillo, CA, USA) and calculating the average over each area. In figure 2.3 an example of these measurements are reported for both bottom surfaces and lateral walls respectively. These analyses [6] provided an average resulting roughness of $R = 23 \pm 7\,\text{nm}$ for the bottom surface, and $R = 8.5 \pm 0.9\,\text{nm}$ for the lateral surface. These results demonstrated to be accurate and precise enough for optofluidic applications, especially the lateral roughness, since it granted an optical grade polishing necessary for the coupling of waveguides. Moreover, it showed a remarkable improvement compare to laser ablation, which achieved in best condition $R = 65 \pm 4\,\text{nm}$ for the lateral surfaces [6].

All the previous analyses were realized on x-cut $LiNbO_3$. However, Z-cut samples micromaching has already studied for the realization of microchannel with optofluidic application in [20, 81], thus showing same optical grade quality of the lateral surface and the feasibility of the technique in z-cut. The engraving direc-

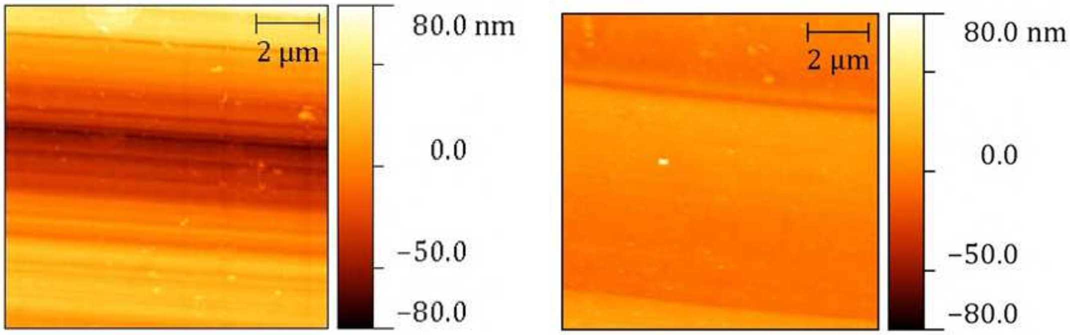

(a) Bottom surfaces (b) Lateral walls surfaces

Figure 2.3. $10x10\,\mu m^2$ *AFM analysis of the surfaces of the test channels: on the left for the bottom one and on the right the lateral one. The color scale is the same for both of the images to allow for a better comparison.*

tions can also affect the quality of the channel due to the complex crystal structure of the material. The channel presented previously was z or y, which can limit the desired geometry. In fact specific applications can require others cutting directions, such as different angles respect to y for exploiting refraction, as showed later in section 4.5. A further investigation was made to study the effect, that the engraving angle respect to the y direction, would have on the channels edge. These tests were performed varying both the angle comp from $0°$ to $32°$ and the thickness of the blade $50\,\mu m$ and $200\,\mu m$, again only the best performances will be presented. In figure 2.4 microscope images of these angled cut are compared depending on the angle and same $50\,\mu m$ thick blade. Same size cuts ($1\,cm$ long and $50x50\,\mu m^2$ of section) are engraved on different sample form the same crystal wafer. The worst quality of the edges is clearly at $30°$, then from $26.5°$ to $15.5°$ the sharpness definitely increase and getting worst decreasing again below $15°$. This behavior seems to be caused by the peculiar crystal structure, which should exhibit different brittleness on different directions. However, same cuts for the worst results were performed with the $200\,\mu m$ thickness blade in the last image of figure 2.4, and it clearly shows that same chipping effect is not visible anymore. Probably this is because the thinner blade can be more affected on lateral vibrations and the different of brittleness of the material can generate this vibrations. Moreover, this effect is also confirmed by the profilometer analysis made by means of surface profilometer P-10 (KLA Tencor, California, USA), since the width of 50 blade width results $10\,\mu m$ larger than the thickness of the blade value, while for $200\,\mu m$ it was compatible. The profiles allow for the measurements of both width and depth of the channel and for statistical significance measurements were done on 10 different channels and 10 different profile for each. Both the averages of the depth for the two blade are compatible with the nominal value with a semidispersion of 1 µm, which is also the semidispersion for the width measurements.

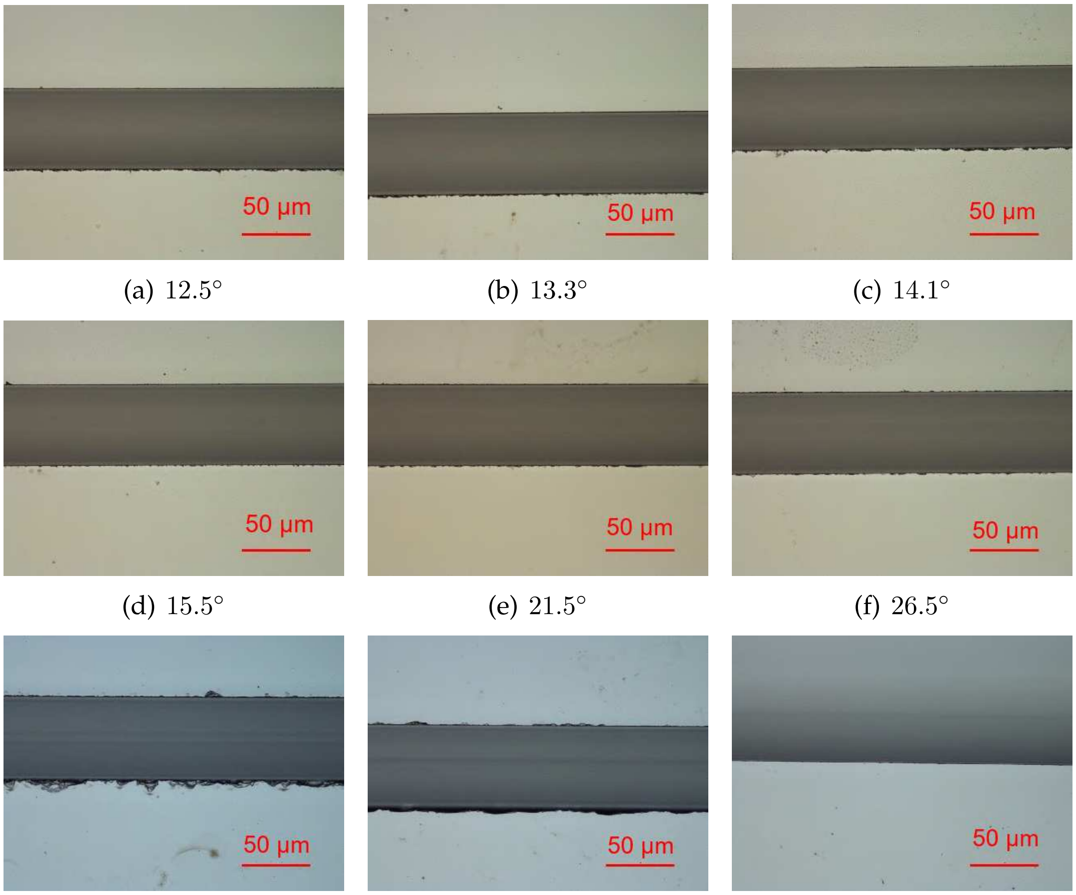

(a) 12.5° (b) 13.3° (c) 14.1°

(d) 15.5° (e) 21.5° (f) 26.5°

(g) 30° (h) 32° (i) 30° (200 µm thick blade)

Figure 2.4. Microscope images of the different angled microchannels (angle values on the bottom of images). All channels are realized with a 50 µm *thick blade, expect for the last one done with* 200 µm *one. The microscope used was a inverted Nikon Ti-E equipped with a 50 times magnification objective.*

2.1.3 Sealing procedures

After engraving channel, the LiNbO$_3$ samples have to be sealed with a top cover, which should allow the connection of fluidic inlets/outlets. The cover material needs specific requirements: firstly, it must be compatible with LiNbO$_3$ substrate, secondly it has to transparent in visible range for applications the imaging system, and thirdly it should be compatible with standard microfluidic fluids. Different solutions were tested in this work, and checking each drawback and advantage in order to match best sealing procedure to the addressed application.

Oxygen plasma treated PDMS bond

This technique is based of the well-known procedure in microfluidics, i.e. the bonding of PDMS (Polydimethylsiloxane[1]) with other material by means of oxygen plasma treatment. In the field this technique is typically employed for the sealing of PDMS devices on a substrate [82]. The steps for PDMS-$LiNbO_3$ bonding is the same as others material. Firstly a layer (1x10 mm depending on the application) of PDMS Sylgard® 184 (Dow Corning, Midland, Michigan, United States) on flat and clean surface is cured at 80 °C for 2 h. Then, it is cut in the proper shape by means of scalpel. Before the plasma exposure of both PDMS cover and $LiNbO_3$ substrate, this latter is properly cleaned with sequential rinses with acetone, ethanol and distilled water. Once cleaned, the substrate is exposed to oxygen plasma for 15 minutes at power of 600 W in a flow rate of 10 sscm using a FEMTO plasma chamber treatment, in order to expose the hydroxyl groups [2] on the material surface. Right after the 15 minutes, the PDMS is added in the chamber, and the same treatment is done for 48 seconds. This process time was defined after a systematic calibration, optimizing both time and power of the plasma exposure, respectively. Such a treatment for PDMS develops silanol group Si−OH on its surface [83]. Then the two substrates are squeezed together in the right position. At this point, the two hydroxyl groups on both surfaces starts to react, creating a strong covalence bound O−Si−O. In figure 2.5 it is reported an example of a final device with PDMS cover.

The fluidic inlets/outlets for this kind of cover are relatively easy to connect, since PDMS is easy to handle both before and after curing. Another advantage of this sealing procedure is the reversibility, indeed, even if the bond itself is strong, $LiNbO_3$ has high chemical resistance, while PDMS has not. Despite this interesting feature, the PDMS cover has several crucial drawbacks, which makes this

---

[1] PDMS: $(C_2H_6OSi)_n$, CAS number: 63148-62-9.

[2] The effects of the Oxygen Plasma exposition are described in terms of free reactive Oxygens promotion on the surface and their recombination with H to give OH group that mainly comes from environmental humidity as well as H adsorbed component. Only in less extent native Hydrogen within the matrix can contribute due to the low diffusion coefficient at room temperature ??.

Figure 2.5. $LiNbO_3$ optofluidic device sealed with a cover of PDMS by means of oxygen plasma treatment. The fluidic connections in this case have been done using 1 mm *outer diameter steel capillary.*

technique unsuitable for certain applications. In particular, the material suffers of aging problem and swelling ones with the contact of standard microfluidic oils, such as mineral oil and hexadecane. The first drawback results in a progressive degradation of the material after several months, thus limiting the huge durability of lithium niobate. The second one is affecting the section of the channel, since the rigidity of substrate forces the expansion of PDMS inside the channel, thus throttling the channel. In particular in optofluidic applications when light is coupled into channel, the swelled PDMS can scatter laser light in unpredictable ways. In conclusion, this technique is optimal for prototyping stages, due to its reversibility. However, it is not suitable for many application, which require oil inside channel.

UV curable glue mediated bonding

Another sealing technique commonly used in microfluidic is the employment of a UV curable glue to bond a cover with the substrate, in particular with $LiNbO_3$ substrates [7, 84]. This technique is based on the presence of a thin layer of glue between two substrate to keep them bonded as depicted on the left in figure 2.6. Since the cured glue layer is rigid materials, this method is more suited for the bonding of two rigid material, such as $LiNbO_3$ or glass. In particular, in this work both $LiNbO_3$-glass and $LiNbO_3$-$LiNbO_3$ were achieved. The procedure is well described by Langelier in [84]:

1. first of all, two substrates are cleaned with standard rinses with solvents (usually sequentially acetone, ethanol and isopropanol),

2. then the two are kept into tight contact using compressive load, which in this work is applied using two point clamps,
3. the glue is distributed all around the contact perimeter using a syringe, and the thin air gap between the two substrates is loaded by the glue via capillary pressure-driven flow.
4. Finally, the bond is formed by cross-linking the UV-curable glue, once glue substituted completely the air.

Herein, the glue used was the UV-curable epoxy resin NOA 68[3] (Norland Optical Adhesive, Cranbury, New Jersey USA), which is colorless polymer liquid photopolymer. It becomes solid after curing under UV light and it has a high chemical resistance to acid solutions and common solvents. This choice was made on the basis of high viscosity, which avoids the drop inside the microchannels, and the chemical resistance. Other resins could work equally well for this application, and the properties of the glue should be chosen depending on the requirements of the application, such as the low shrinkage of NOA 61 used in [84] for acoustofluidic devices. An example of a final device for optofluidic application is presented on the right in figure 2.6. This device presents a cover of silica, where 4 holes are micro drilled in order to allow the fluidic connection made by silicone tubing. In conclusion, this bonding technique does not suffer of aging or swelling problem,

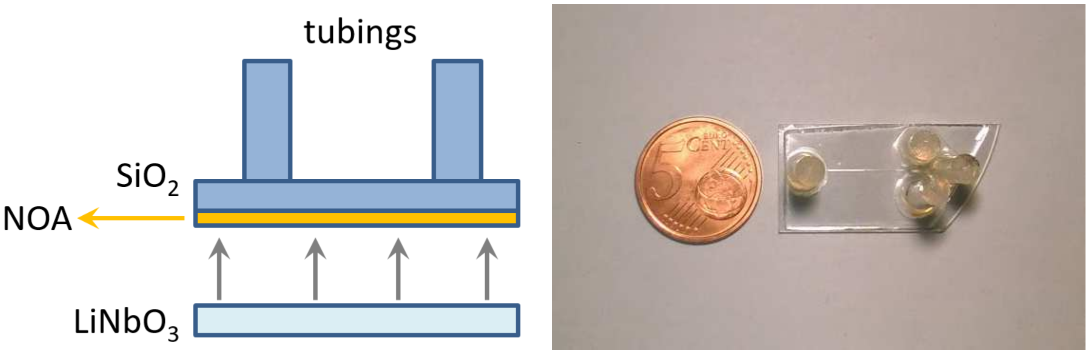

(a) Scheme of the bonding layers (b) Example of final device

Figure 2.6. On the left a scheme of the three layer needed for this bondig procedure is depicted. On the right there is an example of $LiNbO_3$ optofluidic device sealed with a cover of silica by means of NOA 68 glue. The fluidic connections are provided by Masterflex® silicone tubing glued on the silica cover.

---

[3] NOA 68: viscosity 4500-5500 cP, refractive index of cured state 1.54, modulus of elasticity 20 000 psi, tensile strength 2500 psi.

like the previous one, it provides high rigidity to the final device, which is crucial for monodispersity droplet microfluidic applications. Another advantage is the flexibility provided by the choice of the glue depending on the application. However, it requires long processing time compare to PDMS ones, and the reversibility it is not so straightforward. Indeed, the detaching process of the two substrates requires a bath of Chloroform at 60 °C for more than 1 h for NOA 68.

$LiNbO_3$-$LiNbO_3$ direct bonding

Bonding can be defined as a microsystem technology procedure, that aims to permanent seal in a solid-state manner two flat and smooth surfaces [85]. Every bonding procedure consists in three main steps: cleaning and activation of the two surfaces, alignment and pre-bonding details, final sealing. The bonding physical nature can be Van der Waals interaction or chemical bonds, such as hydrogen bonds, depending on the nature of the surfaces. Since the two surfaces have to be placed in close contact due to the chemical nature of this sealing, flatness and smoothness of the surfaces are crucial as well as their cleanliness. Four parameters are typically defined to quantify these latter conditions for the flatness:

total thickness variation (TTV) for flatness, it is the maximum height difference on the surface;

bow for flatness, it is the maximum deviation of the wafer surface (the sum of both side distances) from a reference plane, which is usually considered as a flat surface, on which the wafer lays;

warp for flatness, similarly to bow, it is the same maximum deviation of the wafer surface to a reference plane linearly corrected by the bow;

roughness for smoothness, it is usually considered as the standard height deviation of a surface scan on a wafer.

Typically if the microroughness is higher than 0.2 µm, the surface cannot be bondable [86]. Several procedures have been developed by scientists to achieve the these bonds, depending on the surfaces and physical nature of the sealing to achieve. The most common example are direct bonding [86, 87], anodic bonding [88], solder bonding [89] eutectic bonding [90]. In this work direct bonding of $LiNbO_3$-$LiNbO_3$ is the only tested, in order to verify the feasibility of such

techniques for optofluidic application. Indeed, this technique is not suitable for research purposes, since the irreversibility nature of this procedure.
The samples used for these tests are square of $1x1\,\mathrm{cm}$ from double sided polished wafer from Gooch & Housego (Ilminster, UK) with a nominal $TTV < 10\,\mu\mathrm{m}$, $R_a = 0.2\,\mathrm{nm}$ and $warp < 50\,\mu\mathrm{m}$ with different crystallographic cut direction (z-cut and x-cut). Two cleaning procedures are the most common for $LiNbO_3$ before bonding procedures. The first one involves standard sonic bath and a soak in a boiling solution of NH_4OH-H_2O_2-H_2O (1:1:5):

1. ultrasonic bath in acetone for $10\,\mathrm{min}$;
2. ultrasonic bath in ethanol for $10\,\mathrm{min}$;
3. rinse with distilled water;
4. soak in NH_4OH-H_2O_2-H_2O (1:1:5) for $20\,\mathrm{min}$ at $70\,^{\circ}\mathrm{C}$ (only for the first recipe);
5. rinse with distilled water and drying with nitrogen;

The second includes also Piranha solution H_2SO_4-H_2O (1:3) soak in between steps 3 and 4 for for $30\,\mathrm{min}$ at $70\,^{\circ}\mathrm{C}$. The procedures efficiency was evaluated by measuring the contact angle (CA) of water droplet in order to check improvements. Contact angles for each surface ($\pm z$ and $\pm x$) were measured before and after the treatments, for both recipes in several repeated experiments. As reported in figure 2.7, there is no significant difference between two procedures. Moreover, in both cases a strong hydrophilicity ($CA < 10°$) is achieved.

Once cleaned all the different bond configurations have been tested, but no bond was obtained. However, in literature direct bonding have been already reported [91] using two z surfaces of $LiNbO_3$, $LiNbO_3$ and Si or SiO_2. This unexpected results could be due to either the low atmospheric cleanliness during each steps, or to the lack of plasma activation treatment. A thermal treatment was added in order to achieve bond. An optimal bond was obtained between -z surfaces after $1\,\mathrm{h}$ in O_2 atmoshpere ($50\,\mathrm{N\,L\,h^{-1}}$) at $1000\,^{\circ}\mathrm{C}$. The bond was tested by cutting and lapping, both stressful treatments did not affect the bond.
In conclusion, this procedure could represent the best option to seal definitively a device. If a reproducible bonding protocol could be precisely defined it would be possible to create a microfluidic device that resists to pressure. However, this technique still lacks of reproducibility for a standard protocol, moreover it is not

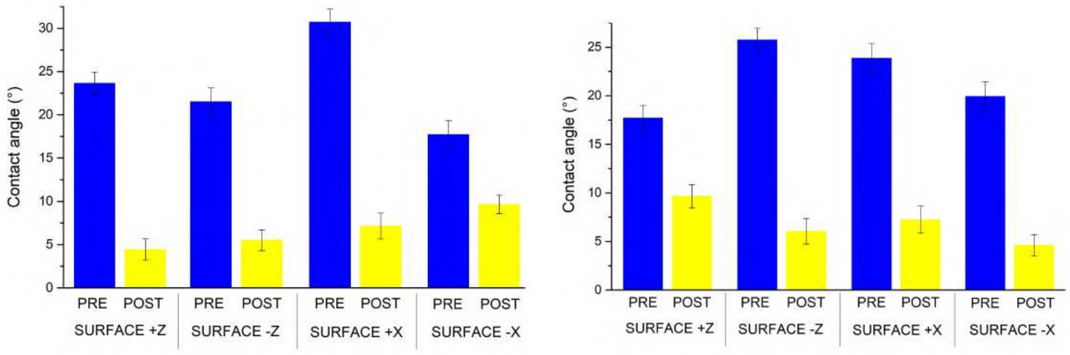

(a) without step 5

(b) All steps

Figure 2.7. Contact angles results for both recipes before cleaning (in blue) and after (in yellow) of 1 µL *water droplet. The error is calculated by the standard deviation over 6 different droplet measurements.*

well suited for prototyping, due to the high level of complexity compare to the others already presented.

Wettability

The realization of microfluidic device was presented in the previous sections, in most of microfluidic application another step is usually required in order to control the wettability of the microchannel, i.e. the interaction between the fluids and the surfaces of the material. In particular, the droplet generation application requires specific wettability properties of the surfaces of the channels depending on the two phases used for the droplet generation. In lab-on-a-chips applications the interest is mainly focused on the generation of water droplet in oil. A complete wettability study of lithium niobate was realized in [92] by means of measurements on the static contact angles of small droplet of liquid used. Bettella et coworkers [92] measured the average water contact angle as $62 \pm 1°$ and the average hexadecane one (which is the oil used in the several applications and also in this one) always less than $10°$. As explained in [92], the moderate hydrophobicity is not enough for the droplet generations, as showed in 2.8, but he proposed a functionalization aimed to increase the contact angle of water. Moreover, a functionalization is also needed for an homogenization of the wettability properties of channels surfaces, since microfludic channels could expose different material on the walls as showed before in this section (top PDMS or glass and other three $LiNbO_3$).

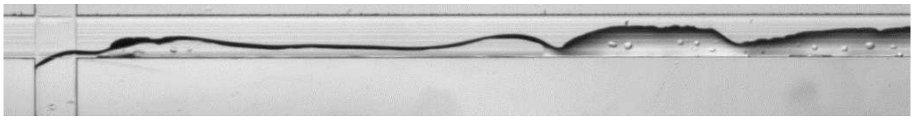

(a) before OTS treatment

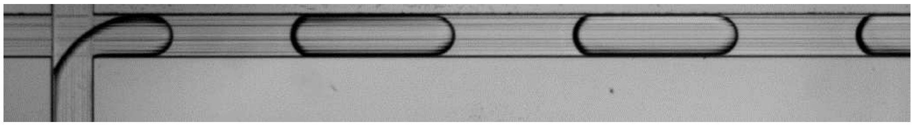

(b) After OTS treatment

Figure 2.8. Examples of droplet production in T-junction configuration, using hexadecane with SPAN® as continuous phase and water as dispersed one. On the top, no droplet are produced because of the absence of OTS functionalization, while on bottom thanks to OTS droplet are prperly produced.

In [93] authors presented two possible functionalizations of lithium niobate, which lead to an increase of CA of almost $30°$ exploiting trichlorosilane molecules. Moreover this self-assembled monolayer technique has been proven also for other materials used in this work, such as silica [94] or PDMS or NOA [95]. In this PhD thesis, devices were functionalized using a self assembled monolayer of octadecyltrichlorosilane[4] (OTS), which is the one also proposed by Bettella [92]. OTS was dissolved in a solution of toluene at a concentration of $100\,\mu\mathrm{M}$, then this solution was fluxed inside the channel for $20\,\mathrm{min}$. During this time, OTS bonds with the channels surfaces of $LiNbO_3$, due to the formation of a siloxy-niobate (–Si–O–Nb–) bond via a condensation reaction between –Si–Cl and niobate hydroxide (–NbOH) [93]. Then the residual OTS-toluene was cleaned by rinsing pure toluene and a thermal treatment at $80\,°\mathrm{C}$. The improvement of this functionalization treatment in terms of water contact angle is on average up to $101 \pm 1°$, and in terms of droplet generation the results can be appreciated in figure 2.8.

2.2 Droplet generator configurations

Since the early years of the microfluidic growth, several droplet generators configurations have been developed and studied: they can be divided in two main general categories the active and passive generators [96] (figure 2.9). The firsts require an external source to achieve the complete droplet break-up, the seconds do

---

[4] octadecyltrichlorosilane: $CH_3(CH_2)_{17}SiCl_3$, CAS number 112-04-9, Mm: $387.93\,\mathrm{g\,mol^{-1}}$, density: $0.984\,\mathrm{g\,mL^{-1}}$.

not, and they are based only on geometry, fluxes and properties of the fluids. In most of the cases active generators are based on a passive ones with an additional active control, in order to enable additional handles for on-demand droplet generation. This section is focused on the demonstration of the droplet generation capabilities of the microfluidic circuitry on lithium niobate, for this reason only passive generator is considered. The extension to an active version from a passive generator device is straightforward, in particular in lithium niobate which offers several properties for this purpose, such as piezoelectricity [97] or inducing field properties [98].

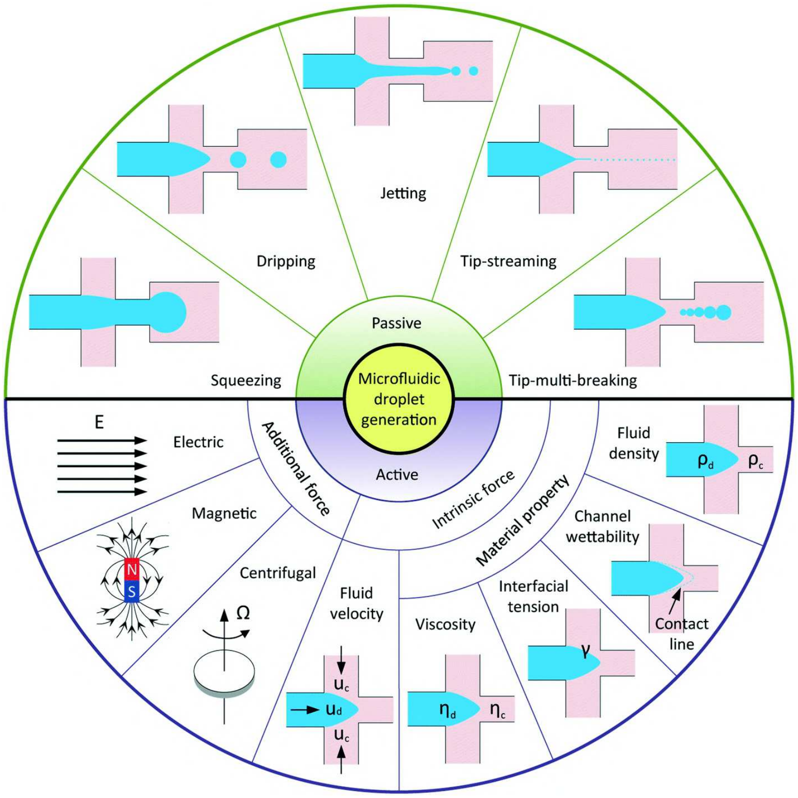

Figure 2.9. Overview of droplet generators: passive and active. Active ones are based on several external input, such as either electric field or magnetic,to allow further handling on the droplet properties. The image is taken from [96].

The most characteristic feature of a passive droplet generator is its geometry, which is commonly base on a junction where the interface between two immiscible fluids reaches the Rayleigh-Plateau instability [99, 100] and the break-up of the droplet happens. The two liquids are usually referred as dispersed phase, which is the droplet liquid, and the continuous phase. For the rest of this work

the *c, d* subscriptions refer respectively to these two phases.
The most used geometries are reported in [101], while figure 2.10 represents an overview of most common configurations:

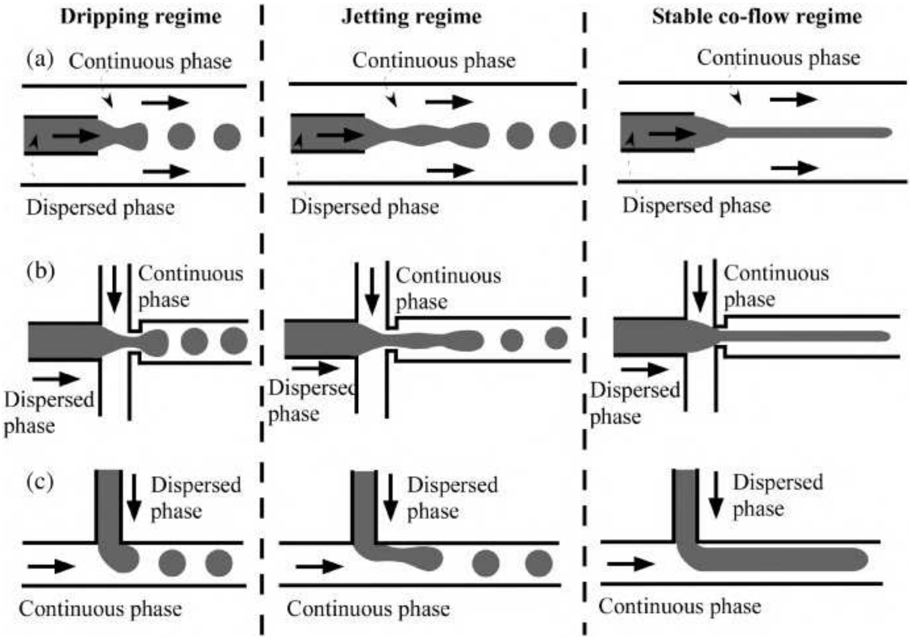

Figure 2.10. The three main passive droplet generators geometries, a) is the co-flowing, b) is the flow-focusing and c) cross flowing. For each of the three junction the three regimes are reported. The image is taken from [101].

co-flowing the two liquids interact by means of two coaxial tube. This is one of first method ever proposed, however nowadays it is not so spread because it cannot be integrated in a chip in a straightforward way as other configurations.

cross-flow the break-up is forced in this geometry by a T-junction, the dispersed phase obstructs the channel shrinking the continuous phase stream. This configuration is one of the simplest to be integrable, due to its simple geometry.

flow-focusing the dispersed phase stream is squeezed by the continuous liquid in two orthogonal channels, in a cross junction configuration. In this case the total flux of the continuous phase Q_c is divided in two halves, one for each channel $Q_c/2$.

The two configurations tested in lithium niobate, herein, are the flow-focusing using a cross junction and the cross-flow using a T-junction. For every passive configuration there are two interesting properties of the droplet, that have to be handle: the frequency and the volume. Both depend on several parameters of the system, such as the densities (ρ_d, ρ_c), viscosities (μ_d, μ_c), interfacial tension (σ) and fluxes (Q_c, Q_d) of continuous and dispersed phases respectively. These parameters influence drastically the droplet break-up as far as the Rayleigh-Plateau instability. Three main working regimes (fig. 2.10) can be identified:

co-flow in this regime, neither the Rayleigh-Plateau instability nor droplet break-up occur. Two phases flow parallel to each other. This regime is usually characterized by small fluids velocities, high interfacial tension, which makes unfavorable the creation of new interface, and similar viscosities of fluid to decrease any drag.

jetting the main feature of this regime is a dispersed phase thread, that connects the junction to the droplet breakup. The Rayleigh-Plateau instability occurs far from the junction. Typically this regime is not the most stable, due to the thread instability. However fast production frequency can be achieved.

dripping this is the standard regime for droplets production. Droplets breakup occurs at the junction. The performance of such regime is optimal for most of the applications, in terms of monodispersity of the droplets and production frequency respectively.

Moreover, other two regimes can be considered:

squeezing This is an extension of the dripping regime [102]. If the droplet break-up is dominated by the drag forces and the droplet does not fill completely the exit channel during the detachment, the regime is still called dripping regime. Whilst, if the pressure dominates in the break-up and the droplet clogs the output channel.

balloon This is a novel regime discovered by Tarchichi [103]. It is a peculiar regime of the T-junction configuration at low velocity of the continuous phase, and the droplet generation depends mainly on the geometry features of the junction and not on the velocities of the two phases.

Each one of these 5 regimes is the results of a complex hydrodynamic system involving small geometries, its wetting interaction with both fluids and their mutual interaction. First approximation that can be made in such system is the continuum hypothesis for the fluids, that is the assumption of the continuity in space of quantities of interest, such as velocity, density and pressure [99, 100]. The molecular nature of the fluid in this assumption is neglected, thus considering the spatial scale higher than the density fluctuation due to the molecular structure. This approximation is a well respected hypothesis in microfluidics, for instance in $10\,\mu\mathrm{m}$ channel there are approximately $30\,000$ water molecule [100], and in particular for device presented here (i.e. $50\,\mu\mathrm{m}$ of minimum geometrical feature). Therefore, it is possible to define a fluid particle small enough to describe in a continuous manner our system, and at the same time large enough to avoid misleading value of properties (i.e. velocity, density and pressure) due to molecular fluctuations. Each liquid fluid particles can be described by the hydrodynamic equation of motion:

$$\rho\frac{Du_i}{Dt} = F_i + \frac{\partial \sigma_{ij}}{\partial x_j} \tag{2.1}$$

where ρ is the density, u_i is the velocity of the *i*-fluid particle, F_i is the external forces applied on the *i*-fluid particle, σ_{ij} is the stressor tensor and $\frac{D}{Dt} = \frac{\partial}{\partial t} + u_j\frac{\partial}{\partial x_j}$ is the material derivative. The equation 2.1 can be written in the standard form of Navier-Stokes equation taking into account:

i) the mass conservation $\frac{D\rho}{Dt} + \rho\frac{\partial u_i}{\partial x_i} = 0$;

ii) the incompressibility $\nabla \cdot \vec{u} = 0$;

iii) the Stoke's law for Newtonian fluid (as liquids of this thesis)$\sigma_{ij} = \mu\left(\frac{\partial u_i}{\partial x_j} + \frac{\partial u_j}{\partial x_i}\right) - \frac{2}{3}\delta_{ij}\frac{\partial u_m}{\partial x_m}$, where μ is the dynamic viscosity:

$$\frac{D\vec{u}}{Dt} = -\frac{1}{\rho}\nabla P + \frac{\mu}{\rho}\nabla^2\vec{u} + \frac{\vec{F}}{\rho} \tag{2.2}$$

where P is the pressure applied to the liquid and $\vec{F}$ is the forces per unit volume. The right side $-\frac{1}{\rho}\nabla P + \frac{\mu}{\rho}\nabla^2\vec{u} + \frac{\vec{F}}{\rho}$ represents the force densities: $-\nabla P$ is pressure driven term, $\frac{\mu}{\rho}\nabla^2\vec{u} = \nabla \cdot \bar{\bar{\sigma}}$ is the diffusion term, which is related with the viscous stresses $\bar{\bar{\sigma}}$ and $\vec{F}$ is the external forces, for the passive generators it is equal to gravity $\frac{\vec{F}}{\rho} = \vec{g}$. Instead, the left side $\frac{D\vec{u}}{Dt}$ is the inertial acceleration, consisting of two terms: time dependent acceleration $\frac{\partial \vec{u}}{\partial t}$ and convective acceleration $(\vec{u} \cdot \nabla)\vec{u}$.

For the case of two fluids two Navier-Stokes equations have to be solved inside the two space domains, considering the following boundary conditions:

i) continuity of the normal velocity on the interface:
$\vec{u}_c \cdot \vec{n} = \vec{u}_d \cdot \vec{n}$

ii) the viscous stress tangent to the interface must be the same for both phases:
$\bar{\bar{\sigma}}_c \cdot \vec{t} = \bar{\bar{\sigma}}_d \cdot \vec{t}$

iii) the normal stress ($\bar{\bar{T}} = P\mathbb{1} + \bar{\bar{\sigma}}$) difference is balanced by the capillary pressure:
$\bar{\bar{T}}_c \cdot \vec{n} - \bar{\bar{T}}_d \cdot \vec{n} = -\gamma k$
where γ is the interfacial tension and $k = R_1^{-1} + R_2^{-2}$ twice the mean radius of the curvature.

As can be seeing, these four forces were mentioned in the equation 2.2: inertial, viscous, and capillary forces and gravity. The latter can be neglected in the droplet formation process, since in the confined geometry it is negligible compared to the viscous forces. Even if the equation can be simplified at Reynolds number $Re = \frac{\rho u L}{\mu}$ smaller than 1 (i.e. the case of microfluidic since $L \approx 100\,\mu\mathrm{m}$), the presence of three interfaces and two liquids makes the system complex and without a unique solution. The standard approach is to describe the physical behavior of the system by identifying regimes, where a main force dominate over a competition between viscous, inertial and interfacial forces. The predominance of one physical effect over another is usually described with dimensionless number, such as Reynolds number $Re = \frac{\rho \mu L}{\eta}$, which is the comparison between inertial and viscous forces. The most commonly used dimensionless number in droplet generation is the Capillary one Ca, which expresses the comparison between viscous stress and capillary pressure, which are the two dominating forces in such small geometries:

$$Ca = \frac{u\mu}{\gamma} \tag{2.3}$$

where u is the velocity of the liquid, μ is the dynamic viscosity and γ is the interfacial tension. This dimensionless number allows for distinguishing the regimes of a droplet generator. Indeed, lower value of Ca corresponds to higher importance of the capillary forces, since the surface of the dispersed phase is lower. Whilst, higher value of Ca are given by the opposite mechanism and it is easier to increase dispersed phase surface. The predominance of one of the two effects in terms of droplet production can be expressed in terms of *scaling laws*. It is a "law of the variation of physical quantities with the size of the system or the object in question" [99]. In particular, in case of droplets two scaling-law are considered: one for the droplet lengths, which can be extended to the volume ($V \approx L$), and one for the frequency. Indeed, these two parameters are the ones interesting for applications of microfluidics, and the aims of the study of a scaling law is to give an instruments for the proper prototyping of a microfluidic device. In the following section scaling laws for both configuration will be described in details. Before that, it is worth mentioning that Navier-stokes equation for droplet generators has been solved using several numerical simulations technique, such as lattice Boltzmann [104]. However, these simulations demonstrated to be quite time consuming, since the complexity of the solutions is directly correlated to the complexity of the geometry and the system. Scaling laws guarantee, therefore, a valid method for prototyping purpose.

2.2.1 T-junction

Scaling laws:

The first scaling laws for this configuration was proposed by Thorsen *et al.* in 2001 [105], where authors gave a physical explanation of the scaling behavior of droplet volumes in a T-junction circuit. Their model was based on determination of droplets volume considering the competition between Laplace pressure and the shear stress acting on the dispersed stream inside the main channel. Five years later, Garstecki *et al.* [106] proposed a finer interpretation introducing a pressure term, which takes into account the resistance to the continuous phase flow by the growing continuous phase tip inside the main channel. The same paper was also the first statement of using Ca (eq. 2.3) as a key value for the distinction between two important regimes in T-junction: squeezing and dripping. These two regimes are characterized by the size of the droplet during the breakup. The squeezing regime feature is the complete obstruction of the main channel droplets before breakup and the pressure term is dominating in the break-up process. Whilst the dripping regime is the opposite, the droplet does not fill completely the channel, and the shear stress is the main reason for the detachments of droplet.

The final equation for the droplet lengths proposed in [106] is:

$$\frac{L}{w_c} = 1 + \alpha \frac{Q_d}{Q_c} \tag{2.4}$$

where $\frac{L}{w_c}$ is the droplet length normalized by the main channel width and α should be $\frac{w_d}{w_c}$ but authors left it as a fitting parameters. This law was confirmed by the same authors with experimental results [106] and by some computational calculation [107]. However, the equation 2.4 has good experimental comparison only in a small range of Ca values, only in squeezing regime. A valid extension to the describtion of the dripping regime, still based on physical consideration, have been done by Christopher [102], where the authors considered three forces acting on the emerging interface in figure 2.11. Since the comparison of the experimental data from the $LiNbO_3$ will be compared with this scaling law, the model will be described more in details. The model considers the break-up instant when the three forces are balanced:

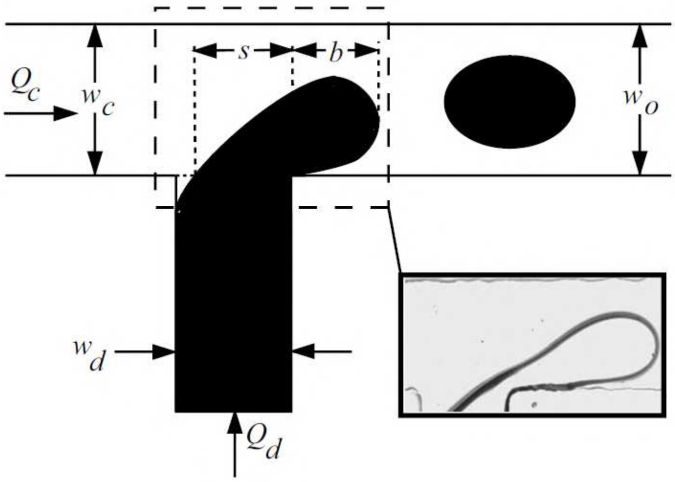

Figure 2.11. Sketch of the emerging droplet considered in the Christopher's model. Both s and b represent distances. The image is taken from [102].

$$F_\sigma + F_\tau + F_P = 0 \tag{2.5}$$

The three forces are:

Capillary force

$$F_\sigma \sim \left[-\sigma\left(\frac{2}{b}+\frac{2}{h}\right)+\sigma\left(\frac{1}{b}+\frac{2}{h}\right)\right] bh = -\sigma h \tag{2.6}$$

it is the difference between Laplace upstream $\sigma\left(\frac{1}{b}+\frac{2}{h}\right)$ and downstream $-\sigma\left(\frac{2}{b}+\frac{2}{h}\right)$ of droplet (with approximation of curvatures), multiplied by the area of interface bh.

Drag force

$$F_\tau \sim \eta_c \frac{u_c}{w_c - b} bh = \eta_c \frac{Q_c u_c}{(w_c - b)^2} \tag{2.7}$$

it is the force generated due to viscous shear applied from continuous phase flowing on the emerging dispersed phase. The shear stress rate is approximated as the average velocity of continuous phase u_c divided by gap size between wall and tip of droplet $w_c - b$.

Squeezing pressure force

$$F_p \sim \Delta p_c bh \sim \frac{\eta_c u_g a p}{w_c - b} \frac{b}{w_c - b} bh = \frac{\eta_c Q_c b^2}{(w_c - b)^3} \tag{2.8}$$

it is obtained from a lubrication analysis [108] for the pressure during flow in a thin gap with aspect ratio $(w_c - b)/b$.

The droplet length during the shrinking of neck (i.e the dispersed phase connection between the growing droplet inside the continuous channel and the dispersed connection, the s sized part in figure 2.11) is calculated substituting equations 2.6, 2.7 and 2.8 into 2.5. The contribution to the length after the neck shrinking is approximated by $u_{growth} \cdot t_{squeeze}$, where $t_{squeeze}$ is the time between the neck shrinking and the breakup $t_{squeeze} \approx \frac{w_d}{u_c} \approx \frac{w_d w_c h}{Q_c}$, and u_{growth} is the growth speed $u_{growth} = \frac{Q_d}{bh}$. Finally the length scaling law obtained by Christopher is:

$$\frac{L}{w_c} = \bar{b} + \frac{\Lambda}{\bar{b}} \phi \tag{2.9}$$

where $\bar{b} = \frac{b}{w_c}$, $\Lambda = \frac{w_d}{w_c}$ and $\phi = \frac{Q_d}{Q_c}$. The Λ parameter is the same α in the previous Garstecki's model (eq. 2.4), indeed for squeezing regime (where b is during detachment is close to the continuous channel width) the equation 2.9 leads to equation (eq. 2.4) if $\bar{b} \to 1$, as expected. With similar arguments they derived also the semi-empirical trend for frequency for constant values of ϕ:

$$\bar{f} = \frac{\eta_c w_c}{\sigma} f \propto Ca^\alpha \tag{2.10}$$

where $\bar{f} = f t_{cap}$, f is the frequency of the droplet production, $t_{cap} = \frac{\mu_c w_c}{\sigma}$, α is a parameter determined experimentally to be 1.31 ± 0.03.

Other several theoretical models have been proposed, however most of them just added further parameters to better follows experimental data without any others theoretical considerations. Instead, Van Steijn [109] followed other approach based on geometrical consideration, and found similar results to the previous one by Christopher.

Experimental

The feasibility of a T-junction realization in $LiNbO_3$ was proven recently by our group in [6, 7, 92, 110]. The T-junction on $LiNbO_3$ consists of two channels both of $h = 100\,\mu\mathrm{m}$ and $w = 200\,\mu\mathrm{m}$ crossing each other ortoghonally, as reported in figure 2.2. The cover was a glass cover and with four connections, but one of the four has been sealed in order to work as a T-junction. The two liquids were: MilliQ® water for the dispersed phase, and hexadecane [5], which was added with interfacial tension γ between two fluids is increased adding surfactant (SPAN®80)[6] in continuous phase at $0.08\,\%$ (w/w). The interfacial tension of the hexadecane with the surfactant was measured using a pendant drop system, using the procedure described in [111]. The results plotted in figure 2.12 confirm the well-known value for the critical micelle concentration CMC of $0.03\,\%$, indeed from the linear interpolations the value obtained is $0.032 \pm 0.002\,\%$. The interfacial tension for the continuous phase with a nominal concentration of $0.08\,\%$ was $\gamma = 4.11 \pm 0.29\,\mathrm{mN\,m^{-1}}$. The liquids were pumped into the channels using two syringe pump PHD 2000 (Harvard Apparatus, Holliston, Massachusetts, USA)[7], and the video recording was made by a camera Phantom VRI v7.3[8] (Phantom, New jersey, USA) connected to an inverted microscope Nikon Eclipse Ti-E (Nikon Corporation, Tokyo, Japan) equipped with a plan 4x/0.1 objective.

Results and discussions

The performance of such $LiNbO_3$ T-junction were deeply tested in [6, 92, 110] in squeezing regime, where it is reported a monodispersity on the droplet lengths always less than $3\,\%$, and for the velocity less than $10\,\%$ (in [6, 92, 110] Δt, the

---

[5] Hexadecane: $CH_3(CH_2)_{14}CH_3$, CAS number: 544-76-3, $M = 226.44\,\mathrm{g\,mol^{-1}}$, viscosity $3\,\mathrm{cP}$, density $0.77\,\mathrm{g\,cm^{-1}}$ at $25\,°\mathrm{C}$.

[6] SPAN®80: $C_{24}H_{44}O_6$, CAS number: 1338-43-8, Mm: $428.62\,\mathrm{g\,mol^{-1}}$

[7] accuracy: $0.2\,\%$

[8] resolution: $800\mathrm{x}600\,\mathrm{px}^2$, pixel size: $22\mathrm{x}22\,\mu\mathrm{m}^2$ and maximum frame rate at full resolution: $6688\,\mathrm{fps}$.

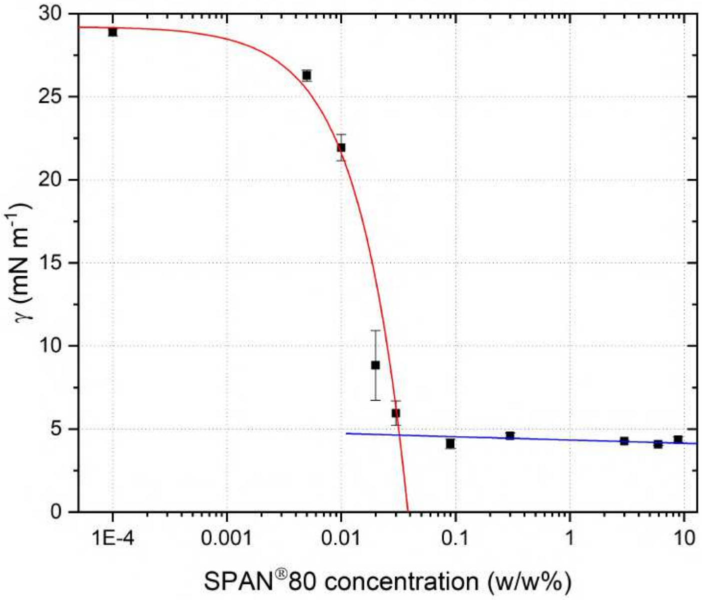

Figure 2.12. Plot of the measured value of the surface tension for different value of surfactant concentration. Each value was measured for five water droplets (nominal volume $0.5\,\mu\mathrm{L}$*) in hexadecane with different concentration of SPAN®80. Blue and red lines are the two linear interpolations for lower and higher value of the* CMC *respectively. The value obtained for the* CMC *from the intersection of the lines is* $0.032 \pm 0.002\,\%$*, which is in agreement with the nominal value of* $0.03\,\%$*.*

time interval between two droplets, is used, the velocity is directly proportional to it). The droplet length monodispersity in LiNbO$_3$ T-junction is agreement with those achieved in other materials ($5\,\%$ stainless steel [112], $2\,\%$ polyester [113], $3\,\%$ PDMS [109], $2\,\%$ glass [114], $2\,\%$ PMMA [115]).

Regarding the scaling laws, in figure 2.13 the length over ϕ is reported, the linearity is well respected by these data, thus confirming that LiNbO$_3$ T-junction follows standard material T-junction behavior.

The scaling laws comparison was also tested, in order to finally cross-checking the performance of the material and allowing future prototyping. Both the scaling laws of Christopher's model were compared: the equation 2.9 for droplet lengths and the equation 2.10 for the frequency. The comparison was done in a range of Q_c from $5\,\mu\mathrm{L}\,\mathrm{min}^{-1}$ to $40\,\mu\mathrm{L}\,\mathrm{min}^{-1}$, and $\phi = \frac{Q_d}{Q_c}$ from 0.3 to 1.5 In figure 2.13 the linear behavior of the data is clearly confirmed, all linear interpolations (gray lines) have $R^2 > 0.99$, thus confirming the linear model of Cristopher [102] (equation 2.9). Moreover, the lack in compatibility among the intercept and the value 1 suggests the better description given by the implementation of the Cristopher's model (equation 2.9) compare to Garstecki's one (equation 2.4). The other

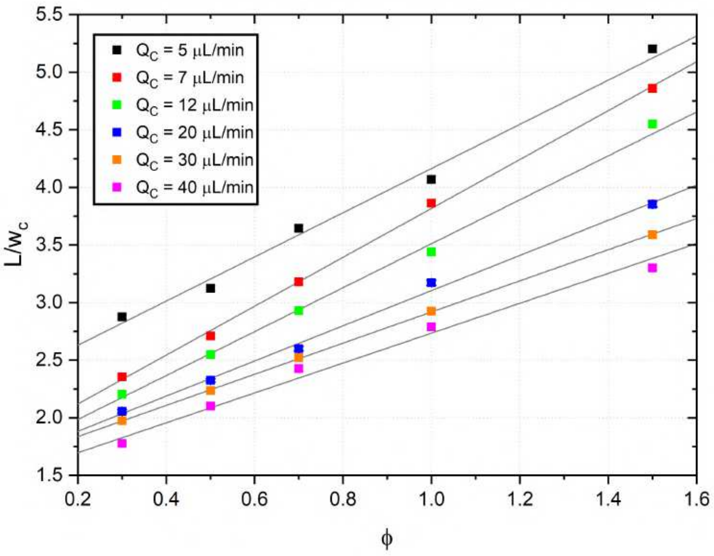

Figure 2.13. The graph represents the normalized length over $\phi = \frac{Q_d}{Q_c}$ data obtained from the video analysis for each data at Q_c fixed. The gray lines are the linear interpolation as suggested by data itself and scaling law from Christopher [102].

useful scaling law proposed by Christopher is the power behavior (equation 2.10) of the frequency $\bar{f}$ with the capillary number Ca_c . The same data were used for this comparison. In figure 2.14 the fits are showed, the data follows clearly a power law behavior. The fitting parameters for the exponent obtained are on average 1.30 ± 0.08, which is definitely comparable with the one measured by the Christopher 1.31 ± 0.03. These results represent a benchmark for the comparison between lithium niobate and other standard material, thus validating the reliability of a LiNbO$_3$ based microfluidic platform.

2.2.2 Cross-junction

Scaling laws:

Flow focusing devices can be divided in different categories, depending on their confinements during the break-up of the droplets. Indeed, the geometry of the device affects drastically the formation of droplets and its various regimes. For

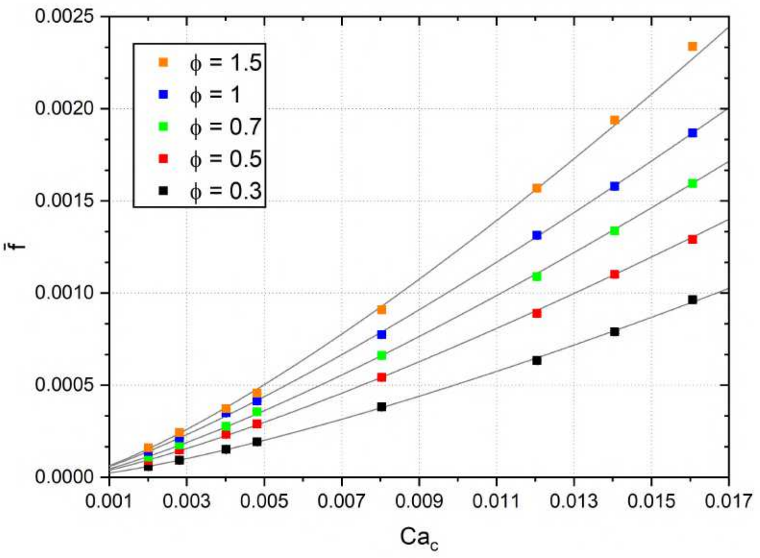

Figure 2.14. Plot normalized frequency $\bar{f}$ over capillary number Ca_c. Gray lines are the interpolations of power law $\beta {Ca_c}^{\alpha}$ for each set at constant value of $\phi = \frac{Q_d}{Q_c}$.

instance, the presence of an orifice just before the cross influences all the break-up process, and in particular its 3 dimensional shape and position can change the droplets generation. In this thesis, only the most simple geometry without orifice is considered as a proof of the feasibility of such configurations on LiNbO$_3$. Indeed, other geometrical features can be easily integrated afterwards, thanks to the aforementioned fabrication technique on LiNbO$_3$, they were therefore considered not necessary to validate the response of a LiNbO$_3$ platform. A complete study about this simple cross geometry were done by Cubaud and Mason [116], where they gave an overview of different working regimes and related scaling laws. The only suitable regime for stable and monodisperse droplets production is the dripping regime. In [116] the authors experimentally observed that the droplets formation weakly depends on the viscosity of dispersed phase, while it strongly depends on the viscosity of the continuous phase and the interfacial tension. Their simple approximation was to consider the droplet length L_d proportional to its velocity $u_d \sim (Q_c + Q_d)/S$ with S the section of the channel, and the time needed for the dispersed phase tip for pinching the cross T_{pinch}. This time is roughly approximated with the time needed by the dispersed phase to fill the volume of the cross $V_{cross} = h * w_c * w_d$ (w_c width of the continuous phase channel,

w_d for the dispersed one) divided by the capillary number Ca_c, $T_{pinch} = \frac{V_{cross}}{Q_c Ca_c}$. T_{pinch} is not proportional to $Ca_c = \frac{Q_c \mu_c}{S\gamma}$ since the stretching of the neck creates more interface. Indeed, the interfacial tension γ acts against the droplet formation and it increases the formation time, while the viscosity μ_c increases the drag force and thus the the dispersed phase tip filling. These considerations lead them to formulate the simplified scaling of:

$$d \propto (\alpha_c Ca_c)^{-1} \quad \text{where} \quad \alpha_c = \frac{Q_c}{Q_c + Q_d} \tag{2.11}$$

Then the authors fitted this model with data and evidenced two regimes, one when the droplet is longer than 2.5 times the channel height and the other, when is smaller. In the second one also the exponent was found different from -1, since small droplets present higher resistance to the side flow-induced break-up. Even if this model is really simple, it still gives an idea on the physical effects that have to be considered. Several others models have been developed in the next decade, some of them are based on the redefinition of the free parameters found by Cubaud's model, such as in [117, 118]. Others are the extension of such model, like in [119], which is still based on the growth time T_{pinch} of the droplet, but it considers the pinching phase as divided in two subphases. Others are related to sophisticated calculations of the volumes during the break-up [120], it gives a function for the frequency, volume of droplet with only one constrained fitting parameters. This model was confirmed by the authors with experiments varying several parameters, although using them only in small ranges. Among all the models developed, the one developed by Liu and Zhang [121] were the only one, which applied similar consideration proposed by Garstecki for the T-junction [106]. The authors developed an empirical relation for the droplet length based on two phases, growing of the tip and squeezing part:

$$\frac{L}{w_c} = (\epsilon + \omega\phi) Ca_c^{-m} \tag{2.12}$$

where $\phi = \frac{Q_d}{Q_c}$, ϵ, ω and m are fitting parameters, which depend on the geometry, such as $\Gamma = \frac{h}{w_c}$ and $\Lambda = \frac{w_d}{w_c}$, and viscosity ratio $\lambda = \frac{\eta_d}{\eta_c}$. The equation 2.12 was confirmed using both experimental and numerical simulations, through which the authors also obtained numerical values for the parameters. Among the others, this model had the highest experimental testing range. For these reasons, the droplets features generated by the cross-junction in LiNbO$_3$ of this thesis will be compared with it.

Experimental

The same structure described in the previous section can be used also as a Cross-junction droplet generator, exploiting the seal fluidic connection (see fig. 2.15). The only difference is the side in which the continuous phase is injected.

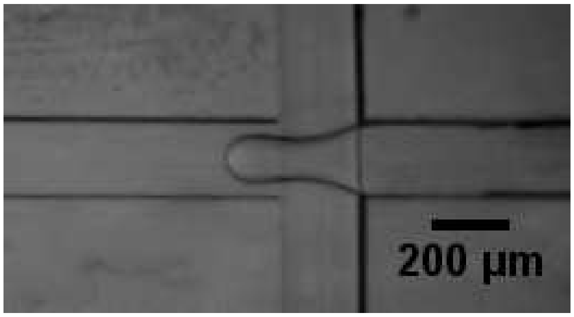

Figure 2.15. Example of the droplet formation in a flow-focusing configuration in lithium niobate based device. Both channels section is $200x100\,\mu m^2$*. Image was taken with the setup described in the experimental section of this chapter.*

The two phases were the same used for this characterization of the T-junction: MilliQ® water for the dispersed phase, and hexadecane with SPAN®80 as continuous phase at $3\,\%$ (w/w). The surface tension for this solution was $\gamma = 4.27 \pm 0.04\,mN\,m^{-1}$ (see fig. 2.12). The experimental setup was different from the previous case of T-junction. Two different configurations were tested. The pumps setup is depicted in figure 2.16: the pump consisted in OB1 MK3 pressure driver pump with 3 channels[9] with a range 0-$8\,bar$ (Elveflow, Paris, France). The flow control was obtained by a feedback system provided by the coupling of three flowmeters BFS Coriolis[10] (Bronkhorst, AK Ruurlo, Holland). Video recording was provided by a camera acA800-510um[11] (Basler, Ahrensburg, Germany) A magnification of 2.6 times was provide by an plan objective 10x, and the illumination by a backlight-collimated led.

Results and discussions

The range of fluxes tested were $Q_d = 5 : 40\,\mu L\,min^{-1}$ and $\frac{Q_c}{2} = 2.5 : 82.5\,\mu L\,min^{-1}$, which allowed for span from the squeezing to dripping regimes. Indeed, the

---

[9] resolution: $0.006\,\%$, stability: $0.005\,\%$, response time: $9\,ms$.

[10] accuracy: $0.2\,\%$, response time: $35\,ms$

[11] resolution: $800x600\,px^2$, pixel size: $4.8x4.8\,\mu m^2$ and max fps at full resolution: $511\,fps$.

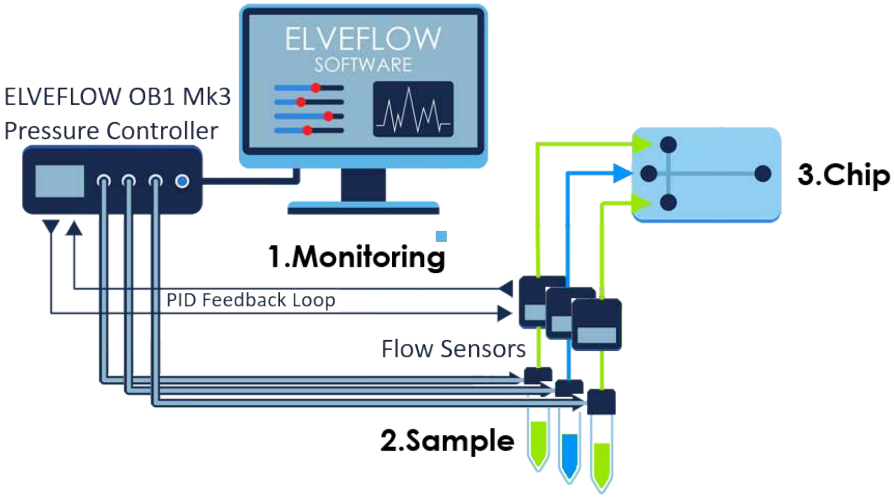

Figure 2.16. Experimental setup for the control of the flow inside the microchannels.

droplet lengths were varied from 1 to 4 times the channel width w_c. For each configuration the device was first filled with continuous phase to avoid any residual air inside, then the fluxes were set by the pump. Thanks to the feedback control guaranteed by the flowmeters, the stability of the flow was monitored, and only when the system was stable the camera started the recording. Typically, the videos of the droplets flowing in the main channel were recorded after 10 minutes from the turning on of the pump. This time was chosen from the interval needed to reach the desired flux by the feedback system of the pump (typically in the order of 1 min) and waiting eventual time due to the hydraulic capacitor of the microfluidic system after the flow meter. 10 minutes guarantee to the system to be in a stable condition, since all the microfluidic system is rigid, i.e. the chip is made by rigid material and the tubing by teflon. The time constant of all the setup should be less than the standard microfluidic one, which is typically in the order of 2 minutes. Moreover, each measurement of this work was realized filling first the fluidic system with the oil, and avoiding any possible residual of air.

The videos of the flowing droplets were taken in a position, which was approximately $5\,\mathrm{mm}$ from the junction. For each fluxes configuration hundred droplets were recorded with at least 10 frames for each droplet, in order to have statistical significance to measure speeds and lengths. Both these values were extrapolated from the frames of each video by means of an homemade tracking software. It measures the *i*-droplet length average $\bar{L}_i$ over all *j*-frame, where the *i*-droplet appears, as showed in figure 2.17. The video recording settings (i.e. the

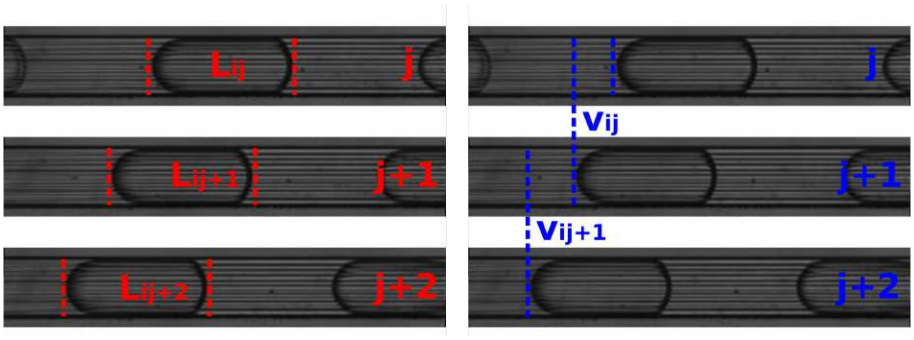

Figure 2.17. Sketch of the working principle of the tracking software: for each j-frame, it measures i droplet the length, on red color on the left, and the velocity, on blue color on the right.

number of frames per seconds and the exposure time) were tuned properly in order to have the same droplet in at least ten consecutive frame, allowing for averaging the quantity of interest for the single droplet. An analogous analysis was done for the velocity. In the following graphs 2.18 are reported an example of the results from the tracking script for $Q_c = 30\,\mu\mathrm{L\,min^{-1}}$ and $Q_d = 10\,\mu\mathrm{L\,min^{-1}}$.

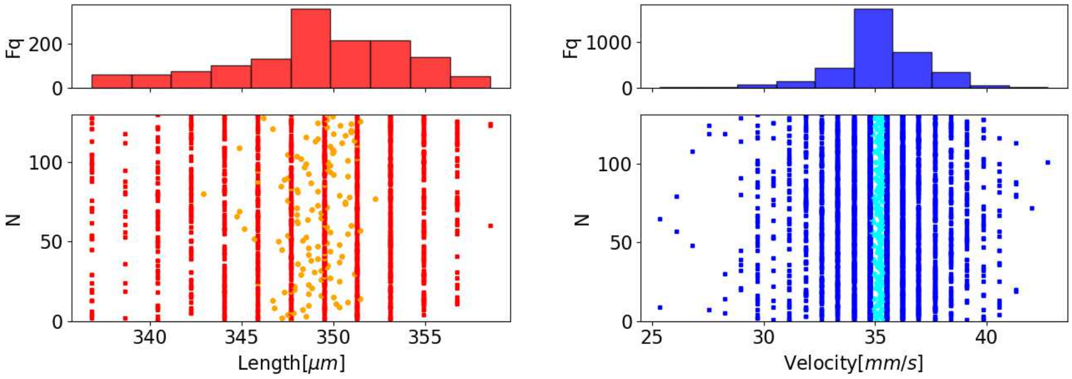

(a) Lengths

(b) Velocities

Figure 2.18. Two graphs report the results from the analysis of the video for $Q_c = 30\,\mu\mathrm{L\,min^{-1}}$ *and* $Q_d = 10\,\mu\mathrm{L\,min^{-1}}$. *On the bottom plots the red and blue points represent the droplet lengths* L_{ij}, *velocity* v_{ij} *for i-droplet and j-frame respectively. The orange and light blue points are the averages* $\bar{L}_i$, $\bar{v}_i$ *for i-droplet over all j-frames. On the top the two histograms are reported based on the overall values,* L_{ij} *on the right and* v_{ij} *on the left. The two mean values for velocity and length are calculated from the two histograms and results* $L = 348.9 \pm 4.8\,\mu\mathrm{m}$ *and* $v = 35.2 \pm 1.9\,\mathrm{mm/s}$.

The analysis of the average parameter for each droplet was implemented to cross-checking the stability during the measurements. As can be seen from figure 2.18 the averages of both lengths and velocities are stable for more than 100 consecutive droplets, this behavior confirmed the stability over time of the system and in particular the stability of the fluxes over time. For each video, the system calculates the average and the standard deviation[12] of the all the single parameters values, L_{ij} and v_{ij}. The device presents good performance in terms of monodispersity of droplet, over the all range tested the maximum, the percentage error range from 4 to $0.5\,\%$ with an average of $1.4\,\%$ for droplets lengths and from 8 to $0.5\,\%$ with an average of $2\,\%$ for droplets velocities. These values are in agreement with other devices presented in literature [122].

The unusual discretization of the measured L_{ij} and v_{ij} (the red and blue markers in 2.18) is due to the fact that the camera acquisition system has pixelization of the measurements. In order to increase the sensitivity and avoid this unpleasant effect, the magnification could be increased. However, an increasing of the magnification should be followed by a consequent increasing of the recording speed, since the field of view would decrease and the frame per seconds of the camera should be tuned properly to maintain the 10 consecutive images of the droplets. The setup was set in order to exploit all the possible range of the recording speed of the camera. A further upgrade of the system could be to use faster camera, but renouncing to the compactness of the video system. The choice would strongly compromise the future possible integration of other part to the setup exploiting other feature of LiNbO$_3$, such as a green beam line for the photovoltaic tweezers reported in the last chapter.
Finally, this data could be compared with the scaling law developed by Liu and Zhang (equation 2.12). The results are plotted in the graph 2.19. From the velocities the capillary number (equation 2.3) can be accurately calculated as:

$$Ca_c = \frac{\mu_c u_d}{\gamma} \tag{2.13}$$

where $\mu_c = 3\,\mathrm{cP}$ is the viscosity of hexadecane, $\gamma = 4.27 \pm 0.04\,\mathrm{mN\,m^{-1}}$ is the viscosity of hexadecane with $3\,\%$ surfactant.

The results of the device presented in this work agree with the model in a huge range of lengths, and even if the device did not have the same parameters Γ, Λ, λ tested experimentally in [121]. Indeed, the chip of this work has $\Gamma = 0.5$, $\Lambda = 1$, and $\lambda = 0.3$ and the interpolation of our data give $m = 0.219 \pm 0.004$, which are in the same order of the with the authors value. Nevertheless, in the graph

---

[12] in this case for a correct estimation $\sigma_x = \sqrt{\frac{\sum_{i=1}^{N}(x_i-\bar{x})^2}{N-1}}$ has been used where N is the number of the samples and $\bar{x} = \frac{\sum_{i=1}^{N} x_i}{N}$.

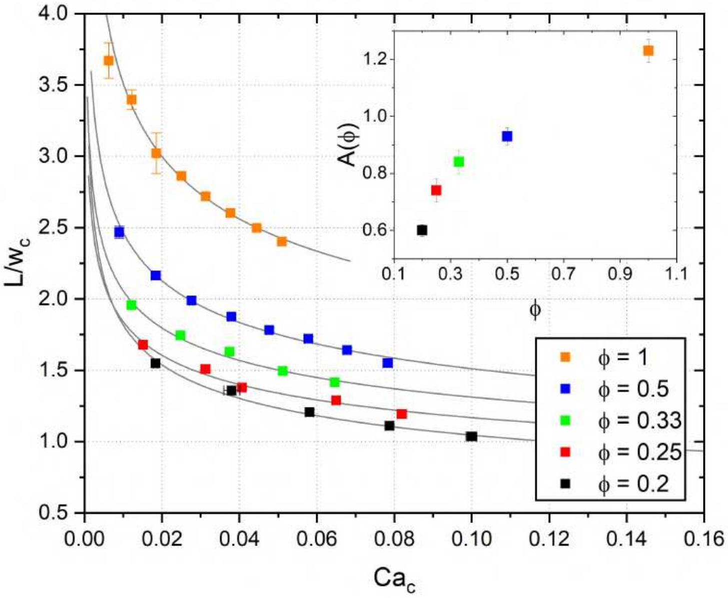

Figure 2.19. The graph represents the length over Ca data obtained from the video analysis and its comparison with the Liu's scaling law [121] (equation 2.12). The gray lines are the interpolations of data with $\frac{L}{w_c} = (A(\phi))Ca_c^{-m}$*, where* $A(\phi) = \epsilon + \omega\phi$*, for each set of data with constant values of* ϕ*. The inset reports the trend of the* A *parameter, which should be linear as predicted by the model for* $Ca < 0.01$*. In the case of these data, it is clear that the linear behavior cannot be clearly confirmed. However, only the point at* $phi < 0.2$ *deviate from the linear regression, these points corresponds to the series with highest values of* Ca*.*

in the inset the $A(\phi)$ value should follow a linear trend, which is only suggested by our data. However, Ca_c values are higher than the one tested in [121], the model, indeed, describes the squeezing regime. Since the data studied in this work were chosen in order to study the higher range as possible, in this case these measurements represent a further advance on the test of validity of the scaling laws, which was not explored at these parameters before.

Chapter 3

Integrated optics in $LiNbO_3$: a way to Opto-microfluidic

In the previous chapter the potentialities of $LiNbO_3$ as microfluidic substrate was demonstrated. In this chapter the attention will be focused on the optimal integration of optical stages on $LiNbO_3$ substrates already equipped with microfluidic circuitry. In particular, the coupling between photonic waveguides and the microchannel, on the same $LiNbO_3$ substrate, will be presented. This coupling consists in the configuration in figure 3.1, where waveguides are crossed by the microchannels, dividing them into two aligned optical units. These are the building blocks of an optical transmission probe: one optical unit working as input whilst the opposite being the output waveguide respectively. This optofluidic integration is particularly interesting, since this transmission optical signal contains several informations on the properties of the matter inside the channel.

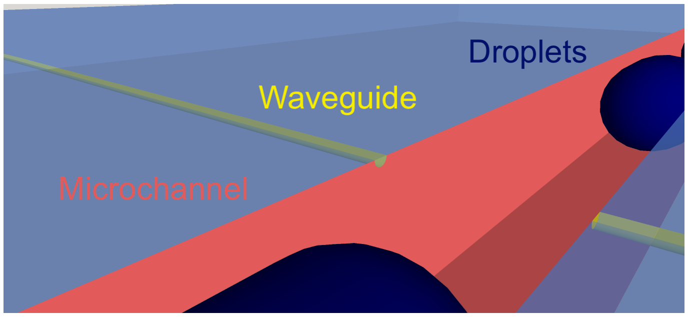

Figure 3.1. Scheme of the final optofluidic device integrated in $LiNbO_3$: the yellow channel represents the waveguides, which face the channel directly on the channels walls. An interesting application is the optical transmission signal of droplet inside the channels.

Until now, several opto-microfluidic devices have been proposed exploiting the interaction of light with microfluidic channel. Most of them relied on the embedding of optical fibers in polymeric substrate [9–13], starting from the pioneering work of Nguyen [8]. Despite the good performances of such devices, the fabrication process presented huge disadvantages compared to those achievable if an integrate optics stage is fully integrated in the same substrate, where the microfluidic one has been embedded. Indeed, the embedding of fibers into the grooves on the chip is a critical step, since the alignment of the two fibers can change a lot between two side grooves and the interlocking between fiber and groove is never $100\,\%$ matched. For these reasons, the process is unsuitable for industrialization purpose. Secondly, the fibers connection represents a weak point in terms of coupling with microfluidic structures. As a matter of fact, the gluing process of fibers onto optofluidic chips is still far from guaranteeing reproducible sealing performances, both in terms of leaking and air sacs formation. Thirdly, the typical diameter size for the fiber core is $100\,\mu m$, which assures in most of the time a complete illumination of all the microfluidic channel, but at the same time it can avoid any local measurements at a measurable level of $10\,\mu m$ into the channels. Few attemps were done also with the coupling waveguide-channel [48, 123–126]. However, in most cases the waveguides were far from the channels, because of a bad quality of the microchannel roughness. In this case waveguided light diffuse out the main direction, causing a lot of noise in the optical illumination. Moreover, some applications can require optical local investigation inside the channel, which cannot be achieved because of fanning process. Finally, most of these waveguides are based on silicon etching, which is a slow technique for microfluidic structures usually in range of hundred of micrometers.

On the contrary, a direct coupling channel-waveguide avoids any gluing process and does not need any grooves, and at the same time decreases the diffusion noise. Moreover, the small light spot in the channel represented by the waveguides output is an optimal source for local measurements. Even if the illuminated volume in the channel is limited by the geometrical features of the channel, the size and the position of the waveguide output, these properties can be tuned for the specific applications. In these terms the waveguide-channel coupling presented in this chapter represents an unexplored way to overcome several drawbacks of the standard optofluidic systems. The chapter is divided in three sections as follows:

3.1 A state of the art of waveguides realization in LiNbO$_3$ is presented, then a detailed description is given for Ti indiffusion technique, and in conclusion the procedure and all the parameters for the realization of the waveguides for this work are reported.

3.2 This second section is dedicated to the characterization of the waveguides. Firstly, the setup used for the coupling is described and the reason of the setup choice is justified by the comparison with other couplers. Secondly, the waveguide features are characterized in terms of modes and losses.

3.3 This section is a description of the features of the optofluidic response, giving particular attention to the affecting properties of coupling between waveguide and microchannels to the optical channel.

3.1 Waveguides for optofluidic application in lithium niobate

Since the pioneering investigations in Bell laboratories in 1950s, $LiNbO_3$ was rapidly recognized as a key material for photonic application, exploiting its functional properties for the realization of a multipurpose device, such as electro-modulators and switches, diffraction gratings and non linear frequency converters. This interest pushed to the development of fabrication methods of waveguides, which represent the basic interconnection for any optical integrated platform. Classical techniques were discovered and developed since late ’60s, such as local doping and proton exchange, and most of the integrated optical devices relied of those methods. However, there is no literature of any optofluidics application until 2015 [5], where Ti-indiffused waveguide are coupled with a microfluidic channel. Others unconventional techniques, such as self-written waveguides, were developed after ’60 to overcome some important issues and to satisfy the demand for better optical performances. In particular, the latter technique was demonstrated to be feasible for an optofluidic application recently in 2012 [20].

3.1.1 State of the art

Several techniques were developed for the realization of $LiNbO_3$ waveguide [127], the purpose of this section is to give a brief overview of the most used methods, explaining the working principle highlighting drawbacks and advantages for an optofluidic application, in particular the transmission of the light across a microchannel by means of a waveguide for both collection and illumination:

Ti-indiffusion It consists in the change of refraction index by means of local doping by means of the diffusion of Ti ions inside the material. This technique is the most studied and widespread in integrated optical application, since its flexibility, relative simplicity and at the same time good light confinements. Indeed, both ordinary and extraordinary refractive indices can be modified by the diffusion of the Ti ions, thus making feasible the propagation of both TE and TM modes [128]. Moreover, the material maintains its electro-optic property after the Ti-indiffusion, thus making this technique really appealing for the realization of optical modulators [129]. Depending on the wavelength and modes, the width of a Ti-waveguide can range from few microns to tens of microns. Such wide Ti-stripes are usually realized by standard photolitography lift-off technique and thermal treatments for the diffusion. The flexibility of photolitography technique opened an high range of application for Ti-indiffused waveguide. Among the others, the advantages ensured by the Ti-waveguides in optofluidic applications are the flatness of the substrate to ensure sealing procedure and flexibility on the geometry design of the waveguided configurations, such as bent structures. Furthermore, the feasibility of a fiber pigtailing connection [130] is necessary for achieving high portability for lab-on-a-chip application.

Proton-exchange In this method the specimen is immersed in a bath of hydrogen ions rich liquid at high temperature, during the process the protons substitute the Li ions inside the material. This replacement induces on the material a strong index change, only the extraordinary one, in general in the order of $\Delta n_e \sim 0.1$. Although this technique does not allow for any changes in the ordinary index, the strong confinement, high polarization rejection and resistance to optical damage are interesting features for specific optical applications, such as non linear application in combinations with a subsequent annealing process and such as visible range application due to its higher resistance to the optical damage. In terms of advantages for optofluidic applications this technique is comparable with the Ti-indiffusion, except for the cost of the loosing one polarization.

Ion-implantation The index of refraction changes can be obtained also by means of the bombardment of the material surface by accelerated ions. The ions release their energy to the crystal lattice through the nuclear collisions and the electronic excitations. Therefore, the penetration depth in the material depends on the ions mass and energy. The energies reported in literature [131] varies from few MeV to $20\,\mathrm{MeV}$, and the ions species implanted were different (H, C, B, O, F, Si, P, Ag). The damages to the crystal lattice on the crystal surface in the trajectories of the ions are usually recovered by a subsequent annealing process. The waveguide structure can be defined by using a photolitographic mask to protect part of the materials surfaces by the bombardment. Although photolitography technique provides same flexibility of the Ti-indiffusion, this technique requires bulky and expensive instruments for the acceleration of the ions, thus closing any extension for applications in fields with strong purpose of industrialization, such as lab-on-a-chip.

Laser writing this technique consists in inducing refractive index changes by means of illumination, either taking advantage from the photorefractive effect (see section 1.2), either damaging irreversibly the crystal structure. The first option requires continuous laser with a power in the rage of tens of mW, while the second needs high power femto seconds laser. Main advantage of these techniques is the extreme free choice on the waveguide 3D structure, since computer driven step motors usually moves the sample during the writing process of the waveguide. Moreover, the reversibility nature of the photorefractive effect allows even for a re-design of the waveguides. This technique advantages are particularly appealing from an optofluidic perspective, in particular the reconfigurability provided by the photorefractive effect. In 2012 Chauvet reported an optofluidic sensor based on this technique [20]. However, the waveguides has a limited life time, thus strongly comprising the portability of a device with laser-written waveguides.

Ridge waveguide Ridge waveguides exploit the index of refraction change between two materials, due to the realization of protruding microscopic structures. These structures can either realized by mechanical micromachining, as described in section 2.1, either by chemical etching, either by ion beam milling. A critical parameter for the losses of such waveguide is the roughness of the surfaces. Such a feature can gives high value of dispersion, which in some cases leads to losses not comparable with other technique, even if the index change ensures high confinement. The technique is not suitable for closed microfluidic device, since the protruding structure represents an obstacle for the sealing procedure.

In conclusion, the waveguides presented in this work were realized by the Ti-indiffusion. Among the suitable techniques for optofluidic application, the Ti-indiffusion provides good confinement in both index of refraction when combined with suitable photolitographic techniques, it allows versatility in terms of structure, such as Mach Zehnder interferometer (section 4.3) and the procedure guarantees high reproducibility for a future simple technology transfer. Finally, all the facilities requirements for the realization of such waveguide were fulfilled by the Department of Physics and Astronomy in Padova.

3.1.2 Ti-indiffused Waveguides

The Ti-indiffused on LiNbO$_3$ waveguides are realized by steps [127]:

1. A positive photoresist mask is realized on the substrate with the desired waveguide pattern, typically the waveguides widths vary from few $\mu\mathrm{m}$ up to tens $\mu\mathrm{m}$, depending on the wavelength and the modes guided.
2. The Ti layer is deposited on the substrate with the photoresist, typically by means of either heated evaporator, either E-beam, or sputtering. The thickness of the layer and the thermal treatment parameters define the depth of the diffusion, which usually ranges from tens up to hundreds of nm.
3. The lift-off process removes the photoresist, thus removing also the excess of the Ti on it, and leaving on the substrate a titanium layer with the pattern described by the mask.
4. Finally the diffusion of titanium is performed by a thermal treatment, usually at temperature between $980\,^{\circ}\mathrm{C}$ and $1050\,^{\circ}\mathrm{C}$ for time between $4\,\mathrm{h}$ and $12\,\mathrm{h}$, depending of the depth desired.

Generally this last step is realized in wet oxygen atmosphere. In particular, the oxygen is necessary, since Ti layer oxidizes into TiO$_2$ at high temperature, and then Ti^{4+} ions migrate inside the material, occupying vacant Nb and Li sites. Instead, the wet atmosphere neutralizes the Li^{+} ions into a LiOh layer on the surface, thus avoiding the out-diffusion of Li inside the TiO$_2$ layer. The diffusion of the Ti ions inside the material is described by the Fick's law:

$$\frac{\partial C(x,t)}{\partial t} = \frac{\partial}{\partial x}\left(D\frac{\partial C(x,t)}{\partial x}\right) \tag{3.1}$$

where x is the direction of diffusion, $C(x,t)$ is the concentration along x and time t dependent and D is diffusion coefficient, which can depend on the temperature and concentration. The concentration $C(x)$ is the interesting properties, since the index profile $n(x)$ is directly related to this properties. If D depends on the concentration the solution of the equation 3.1 is not so straightforward, for instance D is a function of C in case of high dopant concentration, thus leading to a solution that could not be analytical. Only in specific configuration of boundary conditions the equation 3.1 can be solved, using Matano Boltzmann law for description of the D dependencies. On the contrary, when $D(C)$ shows a weak dependence on C (such as for dilute system or C almost constant), D takes the role of an effective Diffusion constant and can be generally describe by the simple model for the Diffusion coefficient is the Arrhenius law $D = D_0 \exp(-Q_D/kT)$, where Q_D is the activation energy (i.e. the energy needed by Ti ions for the starting the diffusion). In the case of independence of D from C, two solutions are interesting for the study of the waveguides case depending on the presence or not of a residual titanium layer on the surface. If the titanium film is not completely diffused, the system can be approximated as a lithium niobate with a surface concentration equal to the saturation concentration C_s. In this configuration the interface is not considered and the titanium film provides a constant concentration C_s during the time of diffusion, it is modeled as an infinite source of Ti ions. This approximation leads to a solution of Fick's diffusion as:

$$C(x,t) = C_{surface}(t)\,\mathrm{erfc}(\frac{x}{\sqrt{4Dt}}) \tag{3.2}$$

However, this solution does not describes all the situation of a real diffusion, in particular the titanium film is completely diffused at some point. This situation can be modeled by a layer with negligible width and considering a reflection boundary conditions at the interface. The concentration of this layer is described by $C(x, t = 0) \neq 0$ only for $x = 0$. The solution of Fick's law for this model is a semi gaussian as described by [132]:

$$C(x,t) = \frac{C_t ot}{2(\pi Dt)^2} \exp(\frac{-x^2}{4Dt}) \tag{3.3}$$

where $C_{tot}(t)$ is the total amount of titanium deposited in the film. $\frac{C_t ot}{2(\pi Dt)^2}$ is the concentration of the imaginary film aforementioned. In the case of titanium waveguide the diffusion in the direction orthogonal to the interface can be modeled by the solution, since the titanium layer is completely exhausted at end of the thermal treatment. Indeed, the SIMS characterization presented later in the section the Ti profile inside $\mathrm{LiNbO_3}$ can be clearly fitted by a gaussian function. Moreover, from this profile the penetration depth can be estimated as the $\sigma = \sqrt{4Dt}$.

These two solutions can be combined to describe the case of a channel waveguide, in fact the Ti ions in this case diffuse in two directions: one normal to the surface and one parallel, due to the presence of a titanium stripe and not a layer. This case is described by two directions concentration $C(x, y, t)$, where x is the orthogonal diffusion direction, whereas y is parallel to the surface. The diffusion in each direction is correlated by the diffusion in the other, and the Fick's law is not separable equation. Nevertheless, a good approximation can be obtained from the combination of the two solutions aforementioned, the diffusion in x can be modeled as the solution 3.3, while along y the diffusion can be described by two solutions 3.2 as follows:

$$\begin{aligned} C(x,y,t) &= C(x,t)C(y,t) \\ &= \frac{C_{surface}}{2}\exp(\frac{-x^2}{4Dt})\left[\mathrm{erfc}(\frac{w/2-y}{\sqrt{(4Dt)}}) + \mathrm{erfc}(\frac{w/2+y}{\sqrt{4Dt}})\right] \end{aligned} \tag{3.4}$$

where w is the width of titanium stripe. This is an approximation from a simple model and consideration, but can still give an two dimensional distribution of the titanium concentration distributions inside Lithium niobate. This distribution is crucial to estimate the index of refraction profile change inside the material due to the diffusion process. The correlation between the Ti ions concentration and both index of refraction of LiNbO$_3$ was obtained phenomenologically in [133] as:

$$\Delta n_{e,o}(x,y) = A_{e,o}(C_{surface}, \lambda)[C(x,y)]^{\alpha_{e,o}} \tag{3.5}$$

$$A_{e,o}(C_{surface}) = \left(\frac{2C_{Ti}}{\sqrt{\pi}}\right)^{-\alpha_{e,o}}\left(B_{0;e,o}(\lambda) + B_{1;e,o}(\lambda)\frac{\sqrt{\pi}C_{surface}}{2C_{Ti}}\right)$$

where C_{Ti} is the Ti concentration in the stripe before diffusion, and $B_{0;e,o}$ and $B_{1;e,o}$ are phenomenological coefficient depending only on the wavelength λ as follows:

$$\begin{aligned} B_{0;o} &= 0.385 - 0.464\lambda + 0.171\lambda^2 \\ B_{1;o} &= 9.13 + 3.85\lambda - 2.49\lambda^2 \\ B_{0;e} &= 6.53\cdot 10^{-2} - 3.15\cdot 10^{-2}\lambda + 7.09\cdot 10^{-3}\lambda^2 \\ B_{1;e} &= 0.478 + 0.464\lambda - 0.348\lambda^2 \end{aligned} \tag{3.6}$$

Ti-induffused waveguide for optofluidics

The waveguides realized for the devices of this thesis are fabricated with the aforementioned process, in this paragraph more details will be given on the parameter used. Each process, showed in figure 3.2, was performed in a clean room

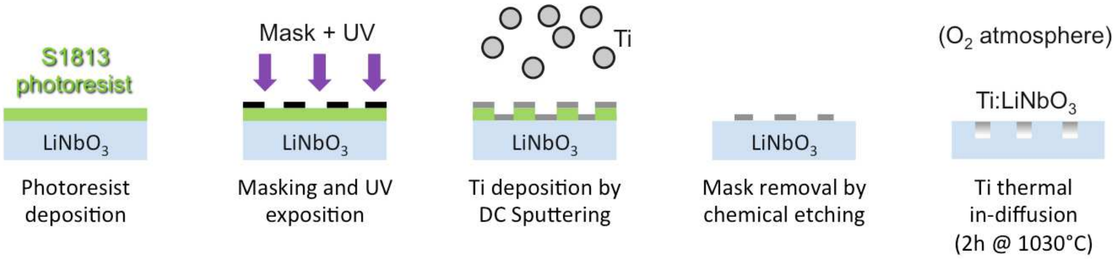

Figure 3.2. Sketches of the mains steps of the Ti-indiffused waveguides production, from left to right: S1813 (S1800 Series, Dow Chemical, Midland, Michigan, USA) photoresist deposition, Uv light exposure, Ti deposition via magnetron sputtering technique, lift-off, thermal treatment.

ISO 7. The photolitographic patterns were designed on the wafer using positive photoresist S1813 from the S1800 Series (Dow Chemical, Midland, Michigan, USA). Before the photoresist depositions, the substrates were coated with an hexamethyldisilizane (HDMS, Dow Chemical, Midland, Michigan, USA) based primer at $2000\,\mathrm{rpm}$ for $30\,\mathrm{s}$. Then, the S1813 was spinned at $6000\,\mathrm{rpm}$ for $60\,\mathrm{s}$ with an acceleration of $1000\,\mathrm{rpm\,s^{-1}}$. The layer thickness was measured with a point contact profilometer P-10 (KLA Tencor, California, USA), and the results was $1.1 \pm 0.1\,\mathrm{\mu m}$, compatible with the value given by the supplier. Before the UV exposure, the sample with the photoresist was soft baked at 60-80 °C for $10\,\mathrm{min}$. Although the supplier usually suggest higher temperature ($115\,^{\circ}\mathrm{C}$), $LiNbO_3$ suffers higher temperature changes, therefore the temperature of this step was decreased and time increased after a calibration. After $10\,\mathrm{min}$ of baking, a Chromium mask was aligned on the samples and pressed into steep contact on to the samples. Then, the samples were exposed at $9\,\mathrm{mW\,cm^{-2}}$ of UV light for $18\,\mathrm{s}$ and right after, another bake step was done at $80\,^{\circ}\mathrm{C}$ for $20\,\mathrm{min}$. The developments were performed by means of soak for $60\,$minute into the developer microposit MF-319 (Dow Chemical, Midland, Michigan, USA).

The following process was the Ti deposition, made by a magnetron-sputtering machine (Thin film technology). The sputtering chamber was evacuated at a $3 \times 10^{-6}\,\mathrm{mbar}$, then an atmosphere of Argon gas was maintained at $5 \times 10^{-3}\,\mathrm{mbar}$. The sputtering DC power was set at $40\,\mathrm{W}$ during the $5\,\mathrm{min}$ of presputtering time and $22\,\mathrm{min}$ of the sputtering time. The resulting Ti-layer had a thickness of $40\,\mathrm{nm}$ measured by means of AFM (Veeco CP-II, Camarillo, CA, USA).

The samples with photoresist and Ti layers were dipped into a solution of SVC(TM)-14 (Dow Chemical, Midland, Michigan, USA) at a temperature of $60\,^{\circ}\mathrm{C}$ until the photoresist was completely removed from the sample. In some cases for

large samples, such as $3\,\mathrm{inch}$ wafer, an ultrasonic treatment was needed to speed up the process. The samples holder kept the samples in vertical position during the soak, in order to avoid any redeposition of detached Ti on the substrate. After the lift-off process, every sample was rinsed with distilled water and checked by the microscope.
Once checked the quality of the Ti stripe structure, samples were put onto a quartz holder into a tubular furnace F-VS 100-500/13 (Carbolite Gero, Neuhausen, Germany). The thermal treatment for the Ti diffusion was performed with heating and cooling rate at $300\,°\mathrm{C}\,\mathrm{h}^{-1}$ and at a final temperature of $1030\,°\mathrm{C}$ for $2\,\mathrm{h}$. During the process, an oxygen gas was fluxed at $50\,\mathrm{N\,L\,h}^{-1}$ into the atmosphere, when temperature was higher then $500\,°\mathrm{C}$, in order to oxidize the Ti. Unfortunately, wet conditions were not reproducible as needed with available set-up so that optimal conditions were not reached. After the diffusion, one last step was needed to properly coupled light inside the waveguide, the cutting and polishing step. The lateral surfaces are lapped and polished with a polishing machine PM5 (Logitech, Glasgow, Scotland), in order to reach optical grade of the surfaces.

SIMS and RBS characterization

The titanium diffusion described before was characterized with standard technique Secondary Ions Mass Spectrometry (SIMS) and Rutherford Back Scattering (RBS), in order to investigate the titanium concentration profile inside $LiNbO_3$ substrates. In particular the Ti layer, before diffusion, were analyzed by an RBS system in Legnaro National Laboratories (LNL-INFN). A proton beam at $2\,\mathrm{MeV}$ hit the Ti layer and a solid state silicon detector with a detection angle of $1.966\,\mathrm{mrad}$ detected the signal at $170°$ respect to the beam. The RBS spectra for a $41 \pm 5\,\mathrm{nm}$ thick Ti layer is reported in figure 3.3. Since the aim was to investigate the Ti layer, the RBS measurements were performed on a substrate of SiO_2 instead of $LiNbO_3$, because the backscattering of SiO_2 pattern is well-known and it allows for a faster analysis. A gaussian interpolation of the clear peak about channel 370 , which is the one refers to Ti, was performed to obtain the Ti atoms concentration in the layer $C_{Ti} = (4.1 \pm 0.1) \times 10^{22}\,\mathrm{cm}^{-1}$.

The concentration profile of Ti inside $LiNbO_3$ substrate was measured by SIMS measurements. The SIMS was ims4f mass spectrometer (CAMECA, Gennevilliers, France) equipped with a Cs^+ beam at $10\,\mathrm{kV}$, which guaranteed an im-

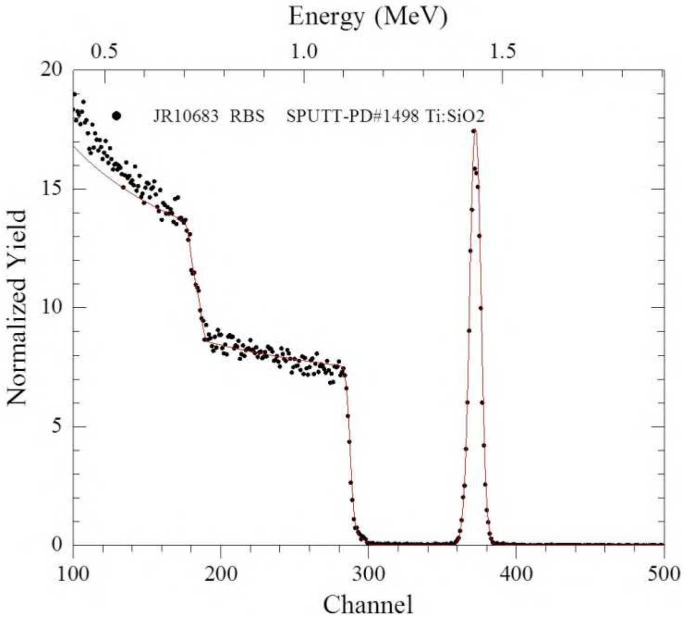

Figure 3.3. Experimental RBS spectra obtained from the measurement of a Ti layer on SiO_2: on the left there are the clear background of SiO_2 and around channel 370 *there is a clear backscattering of Ti peak.*

pact energy to the ions of $14.5\,\mathrm{kV}$ of impact energy, because of the $-4.5\,\mathrm{kV}$ of the sample holder. During the second ions detection an electron gun compensated the charge losses on $LiNbO_3$. The Ti ions extracted from the substrate were selected by an energy sector followed by a magnetic mass spectrometer, and the number of ions signal over time was, then converted into depth estimating the erosion speed of the Cs beam. In figure 3.4 there is a graph with the SIMS analysis obtained, which describes the Ti concentration over the depth of the $LiNbO_3$ substrate.

The resulting data from the SIMS were interpolated with a gaussian profile and the Diffusion constant can be estimated $D = \frac{\sigma^2}{2t} = 89 \pm 2\,\mathrm{nm}^2\,\mathrm{s}^{-1}$, where σ^2 is the gaussian variance and $t = 2\,\mathrm{h}$ is the diffusion time. Moreover, the $C_{surface}$ can be extrapolated from the data and it results $(1.06 \pm 0.04) \times 10^{21}\,\mathrm{cm}^{-1}$. In conclusion, from the values of D, $C_{surface}$ and C_{Ti} and the change in index of refraction for this work waveguide can be calculated from the equation 3.5 and result:

$$\begin{aligned} \Delta n_e &= 1.12 \pm 0.03 \cdot 10^{-2} \\ \Delta n_o &= 0.66 \pm 0.02 \cdot 10^{-2} \end{aligned} \tag{3.7}$$

The choice of these diffusion parameters (i.e. the t =2 h) with the $5\,\mu\mathrm{m}$ guarantee the single mode at $632.8\,\mathrm{nm}$. Although multimode waveguides usually provide

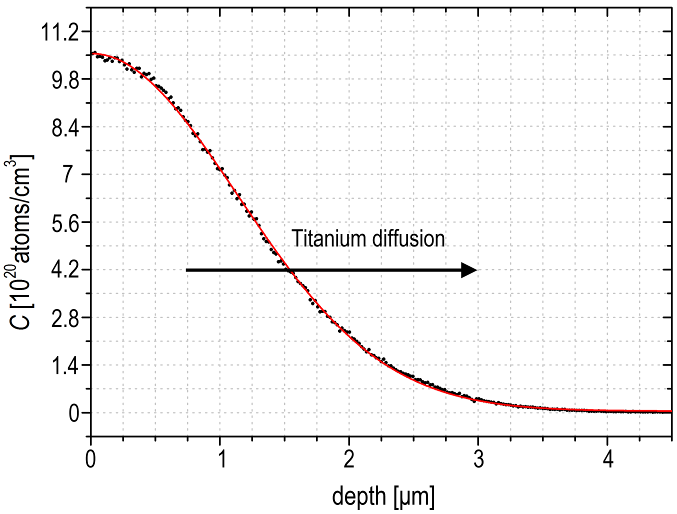

Figure 3.4. the graph represents the results of a SIMS analysis: the concentration profile of Ti inside a$LiNbO_3$ *substrate, obtained from the diffusion of a* $41 \pm 5\,\mathrm{nm}$ *titanium film on a x-cut* $LiNbO_3$ *substrate after diffusion in* O_2 *atmosphere at* $1030\,°\mathrm{C}$ *for* $2\,\mathrm{h}$.

higher light transmission, the single mode is the simplest one to study the interaction of the light from the waveguide with the channel. Moreover, it allows for simpler pigtailing coupling, even if the refraction index difference 3.7 cannot afford the best end-butt coupling. However, the Ti-indiffused single mode waveguides are the best solution for prototyping application, and in the future new technique and waveguides can be easily integrated.

3.2 Near field analysis

There are several techniques to couple laser light inside a waveguide (figure 3.5), such as prism couplers [134–136], transverse couplers [137, 138] (both direct focusing and end butt coupling), grating couplers [139, 140], and tapered couplers [141, 142]. Each of these coupling methods was initially developed for different characterizations and applications, for instance prism couplers for thin film characterization [136], or permanent pigtailing for stable realization of optical devices [138]. Among the others, the latter has the best features required for a lab-on-a-chip realized in $LiNbO_3$, since it is permanent, stable and portable. Nevertheless, it does not represent the optimal solution during the prototyping stages, since during testing phase cannot be flexible. A reliable alternative is represented by the direct coupling made by the objective in a near field setup. It allows an output mode characterization of the waveguides and a preliminary study for any transverse coupling method.

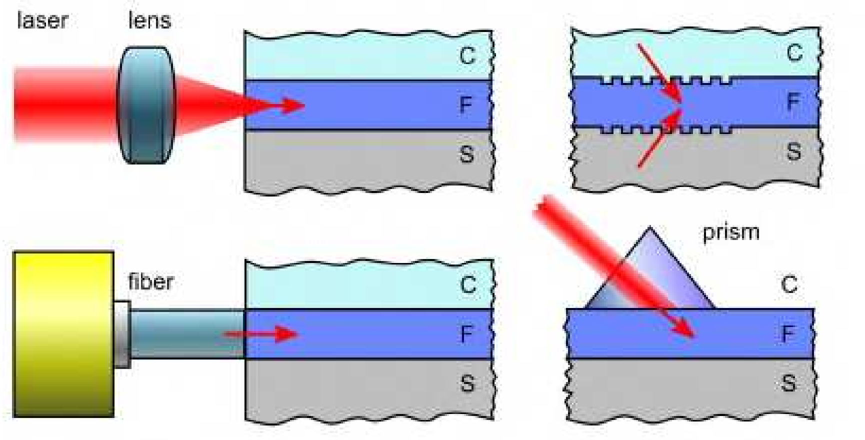

Figure 3.5. Sketch of most used waveguide coupling methods. Grey box S represents the substrate, C in light blue the clad and F in blue the core of the waveguide. On the left two different transverse coupling, where bottom one represents the pigtailing. On top right there is schematic representation of a grating coupler, and on the bottom left a prism coupler.

3.2.1 Experimental setup

In this section a description of the setup used to couple the light inside the waveguide will be given, since other parts of the setup, such as sources or detectors, depend on the application, it will be describes in the next chapter. As aforementioned, the coupling technique used is a transverse couplers using a double objective setup, one to focus the light inside the waveguide and the other to collect the light in a near field. Two objectives mounted on the setup are a 20X Objective for coupling light, and a 50X long working distance for recollecting the light. The coupling is maximized when the numerical aperture of the coupling objective is equal or smaller than the numerical aperture of the waveguide. The numerical aperture of the setup is measured by a CCD, coupling a $632.8\,\mathrm{nm}$ and measuring the profile depending on the distance from the objective [92]. In figure 3.6 the behavior of the waist in both direction over the distance is reported. From these data, the initial waist w_0 and Rayleigh length z_R were measured by the interpolation of $w(z) = w_0\sqrt(1 + (\frac{z}{z_R})^2)$, which are reported in the graphs in figure 3.6. The numerical aperture can be calculated as follows:

$$NA = \frac{w_0}{2z_R} = 0.09 \pm 0.01 \tag{3.8}$$

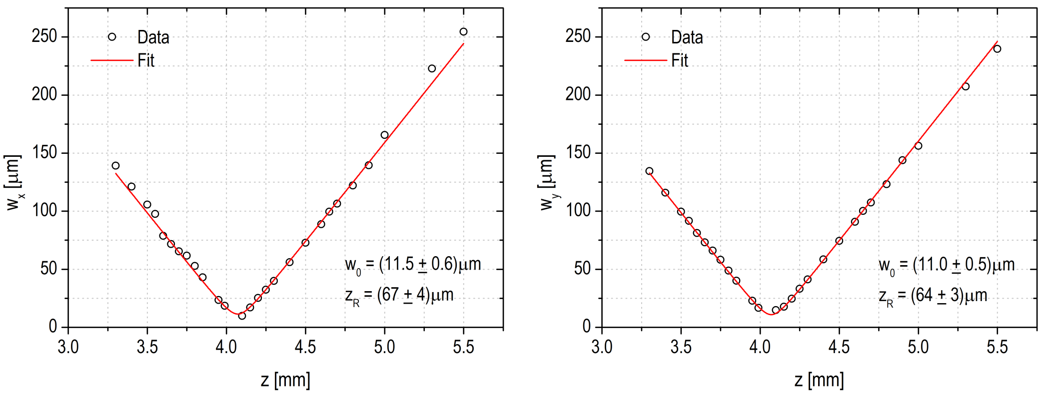

(a) (b)

Figure 3.6. Waists derived from the gaussian interpolation of the laser spot at different z distance from the objective. The red line represent the interpolation with gaussian beam dispersion $w(z) = w_0\sqrt{(1+(\frac{z}{z_R})^2)}$. *The Rayleigh lengths obtained from such interpolation are reported in bottom of the graphs.*

An estimation of the numerical aperture of the waveguide can be done as described by [143], where an effective value for a graded index z-propagation waveguide with asymmetrical 2 dimensional profile (standard case for Ti-indiffused waveguide) is calculated as follows:

$$NA_{eff} = \sqrt{(\frac{n_{max}^2 - n_{clad}^2}{2})} \quad \text{where for this work:} \quad NA_{eff} = 0.13 \qquad (3.9)$$

Thanks to this system, the setup can measure both the intensity and the output mode of waveguide, depending on the sensor. Two different laser light sources were coupled inside the waveguide: a continuous diode laser with power of $7.35\,\mathrm{mW}$ and a wavelength of $532\,\mathrm{nm}$ and a He-Ne laser with a wavelength of $632.8\,\mathrm{nm}$ and power of $4\,\mathrm{mW}$. An half plate and a polarizer can be then added in order to excite both the TE and TM mode of the waveguide.

3.2.2 Near field characterization

An output mode characterization can be obtained coupling a CCD LaserCam-HR II (Coherent, Santa Clara, California, USA), thus allowing for a near field study of the output modes from the waveguide. Such an analysis is required to investigate the waveguide quality and to provide the modal profile often needed in photonics applications as well as for pigtailing coupling. As a matter of fact, a future pigtailing coupling makes the device able to collect the signal in high integrated level. The analyses were done on eight x-cut samples for a total number of 40 z-propagating guides, which is the most common configuration used for the future presented applications. In particular, the characterization was done on Ti indiffused $5\,\mu\mathrm{m}$ wide waveguide, which exhibits only a mode with a gaussian mode excitation in the visible range [17]. Even if the infrared range is the most suitable for $LiNbO_3$ in terms of losses, the visible range has several interesting applications in lab-on-a-chip application, such as spectroscopic ones. Nevertheless, once demonstrated an application with visible range, the extension to a IR is straightforward.

An example of the shape of the output from a $5\,\mu\mathrm{m}$ wide waveguide is reported in figure 3.7.

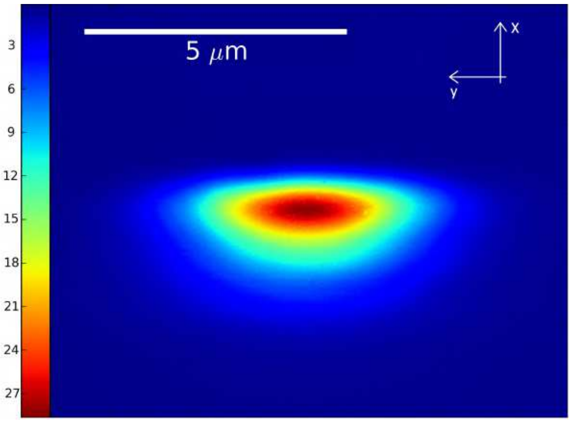

Figure 3.7. Example of a CCD image of a near field output from a $5\,\mu\mathrm{m}$ *wide Ti waveguide. The intensity scale is in arbitrary units. Two little arrows on the top are the reference frame according with the crystals axis.*

Figure 3.7 shows the expected confinement of the light due to the index profile, on the x axis the intensity is more confined due to the higher index contrast with air. The shape of the intensity confined in the waveguide gives a direct idea of the index profile and, consequently, of concentration of titanium, which depends on the diffusion parameters. The mode is related to diffusion time, which was chosen in order to obtain an optimal mode. On one hand the waveguide had to be studied with butt-coupling technique and have a good pigtailing coupling, but at the same time provide an optimal source for the microfluidic channel.

In order to quantify the properties of this output and its reproducibility a deeper analysis is required. The study of the reproducibility of the output mode shape was done by an analysis of 4 profiles: along y, along x and the two at $45°$ degree (figure 3.8). The only profile, that can be interpolated with a gaussian function, is the horizontal profile on the left figure 3.8, since both sides of that profile present the same index of refractive distribution.

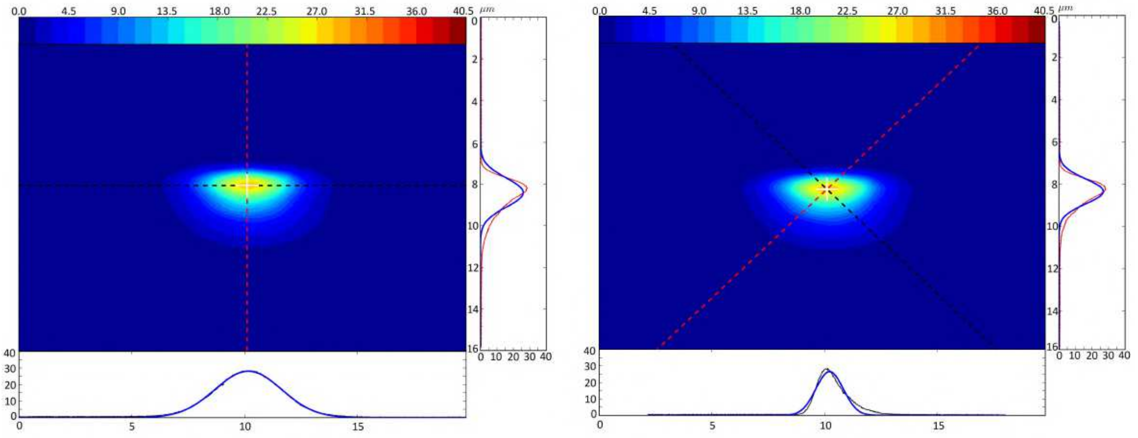

Figure 3.8. Analysis of the waveguide mode in figure 3.7: on the left x and y are reported in the side graphs, on the right same analysis for the two profiles at $45°$*. The blue lines in the side graphs represent the gaussian fits.*

The integrals I between the background value and the $16\,\%$ of the maximum intensity are calculated for each waveguide and for each side of the profiles, in order to measure quantitatively the reproducibility of such a shape. These integrals give a quantitatively description of the surrounding intensity distribution of the mode, which is the most sensitive part of the mode to the refractive index profile. In particular, two different parameters were obtained from these integrals:

$$S_{x,y} = \left(I^{left}_{x,y} - I^{right}_{x,y}\right)\left(I^{left}_{x,y} + I^{right}_{x,y}\right)^{-1} \tag{3.10}$$

$$D = \left[\frac{I^{left}_{+} - I^{right}_{+}}{I^{left}_{+} + I^{right}_{+}}\right]\left[\frac{I^{left}_{-} - I^{right}_{-}}{I^{left}_{-} + I^{right}_{-}}\right]^{-1} \tag{3.11}$$

where $I^{left,right}_{X,Y}$ represents the left or right integrals along direction x or y, $I_{+,-}$ refers the integrals along two directions +$45°$ or -$45°$ respectively. The idea behind these two parameters is: for the first one S (eq. 3.10) the estimation of the symmetry reproducibility of the mode shape along the two crystallographic directions, for the second D (eq. 3.11) is the measurement of the difference between two diagonal profiles. Both analyses were done for forty waveguides on eight samples for both polarization TE and TM, in table 3.1 all the averages are reported.

The variance on the mean obtained from analysis is always less than $15\,\%$, showing a remarkable reproducibility of the mode shape over different samples and

TE:		
S_x	S_y	D
0.23 ± 0.02	0.038 ± 0.006	1.00 ± 0.07
TM:		
S_x	S_y	D
0.26 ± 0.02	0.059 ± 0.006	0.96 ± 0.05

Table 3.1. Results of the analysis on the parameters S (eq. 3.10) and D (eq. 3.11) for both polarization over 4 waveguides. Means and relative errors are reported.

waveguides. Moreover, from the results of the analysis reported in the table 3.1 some information about the guide symmetry could be gained. S_y is close to zero suggesting that the diffusion of titanium parallel to the surface could be considered symmetric as expected. The same conclusion can be obtained from D compatible to one, thus meaning a high symmetry on the two diagonal profiles. Along x direction, on the other hand, the high difference between refraction indexes of air and $LiNbO_3$ led S_x to be significantly different from 0. Finally, no detectable differences were observed between the two polarizations. This analysis demonstrated the high reproducibility of the fabrication method and showed some features on the output mode shape, thus suggesting that the reproducibility of the process is sustainable and open the way to a future upgrade of the pigtailing coupling.

Another important study on the waveguides is the measurement of the propagation losses, in order to check the performance of the waveguides. The procedure consisted in the cut-back technique, which is the transmission intensity measurements of different guides varying their lengths. Usually it is performed for a fixed coupling input source in the waveguide, which in our case it was not available. However, the error due to the coupling efficiency can be estimated and considered during the analysis. The steps followed were: measurements of the transmitted intensities by four waveguides were measured at different lengths of the samples after well-known distance cuts (each cut is perpendicular to the propagation direction of waveguides). The intensities for the four guides were measured for seven different lengths[1]. As aforementioned, the dispersion on the transmission intensity was given mainly from the coupling instability, for this reason the errors were calculated from the standard deviation of 10 measurements with different coupling on the same waveguide. The data were fitted with $I = y_0 + I_0 \exp -\alpha(L - L_0)$, where I is the laser beam intensity, α is the attenuation coefficient, L is the length of the guide, y_0 and L_0 are fitting parameters and both resulted compatible with zero. Results of the analysis are reported in 3.2, where the attenuation coefficient α is reported in logarithmic scale $\alpha \to (logscale) log_{10}(\exp -\alpha)$.

# Waveguide	$\alpha[\mathrm{dB\,cm^{-1}}]$	σ_α $[\mathrm{dB\,cm^{-1}}]$
1	3	2
2	8	2
3	4	3

Table 3.2. Results of the attenuation coefficient α from the data fitting $I = y_0 + I_0 \exp -\alpha(L - L_0)$ for 6 different waveguides.

These values are comparable for the literature value for visible wavelength, for instance Irrera [144] obtained $2\,\mathrm{dB\,cm^{-1}}$. These value are higher than the one obtained for IR range: indeed, the coupling with visible range light is not common in LiNbO$_3$ due to its telecom successful exploitation. However, in many lab-on-a-chips the visible light is much more interesting, such as intracellular dyes [145], and as proven in the next chapter the intensity is not a limiting factor for these application. In fact, $1\,\mathrm{mW}$ laser beam is far enough for the transmission of the light across the channel, and it allows for probing application.

3.3 Microchannels and waveguides coupling

The light transmission at the output of the Ti-indiffused waveguide on LiNbO$_3$ can be analyzed only if the quality of the output surface roughness has an optical grade. The achievement of the light transmission between two waveguides on the two sides of microfluidic channel can be obtained only if the channel walls have such a quality. The engraving of microchannels described in section 2.1 provides

---

[1] Measurements were carried out by Dr. Anna Zaltron and Rita Scolaro in Department of Physics and Astronomy in Università degli Studi di Padova

a self-polishing behavior, thus channel walls show the required feature for the optical transmission [6]. Any roughness higher than the wavelength can scatter light in every direction, thus causing diffusion and avoiding a good transmission across te channel. Since the roughness from the engraving technique is less than 1/10th of th visible range, there are no needs of any other process for guaranteeing the transmission. Therefore, the coupling between Ti-indiffused waveguides and the microchannel on the same $LiNbO_3$ substrate is straightforward. Firstly, the waveguides were realized on the samples, then the channels were engraved directly onto the sample, in an orthogonal direction respect to the waveguides. During the cut, the waveguides were basically divided into two parts by the engraving process and the channel, and both outputs were directly on the channels walls. A schematic representation of such coupling between the waveguide and the channel is reported at the presentation of this chapter in figure 3.1. This process does not need any precaution on the coupling, neither in terms of design on both structures, microfluidics and waveguide, neither in terms of future fabrication steps.

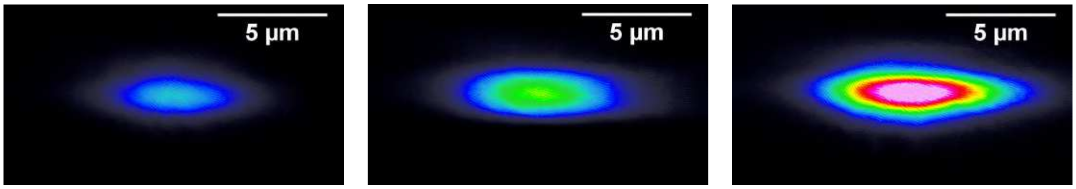

(a) Air $\frac{I}{I_0} = 38\,\%$ (b) Water $\frac{I}{I_0} = 46\,\%$ (c) Hexadecane $\frac{I}{I_0} = 76\,\%$

Figure 3.9. Example of a near field images of a z-propagating waveguide coupled to a $200\,\mu m$ *wide microfluidic channel: from the left channel is filled with air* ($n = 1$)*, water* ($n = 1.333$) *and hexadecane(*$n = 1.434$)*. The wavelength of light is* $632.8\,nm$ *and same attenuation were used for all images.*

The light cone is effectively influenced by the liquid inside the channel and also by the cover, from which part of light is refracted and reflected as depicted in figure 3.10. This light cone from the waveguide represents basically a local optical probe of the channel, depending on the position and the index of refraction the illumination part of the channel can be tuned. Indeed, if the channels geometry does not allow for a complete illumination of the matters inside it, the light interacts only with specific portion of it. This is a novel feature in the field of integrated optofluidics since the fibers devices usually probe all the channel feature. In this thesis the configuration used is always the first one reported in figure 3.10, which it is not the optimal in terms of transmission because of the cover presence. However, the configuration can be easily modified by means of either a chemical etch of the cover, exploiting the chemical resistance of the lithium niobate (center sketch of figure 3.10), either adding a extra layer before the engraving process (right sketch of figure 3.10). Therefore, the optical probe, i.e. the waveguide output can be positioned in any position, depending on the applications needs. The latter results demonstrates the possibility of the simplest configuration, this improvement could lead to other interesting perspectives and new applications.

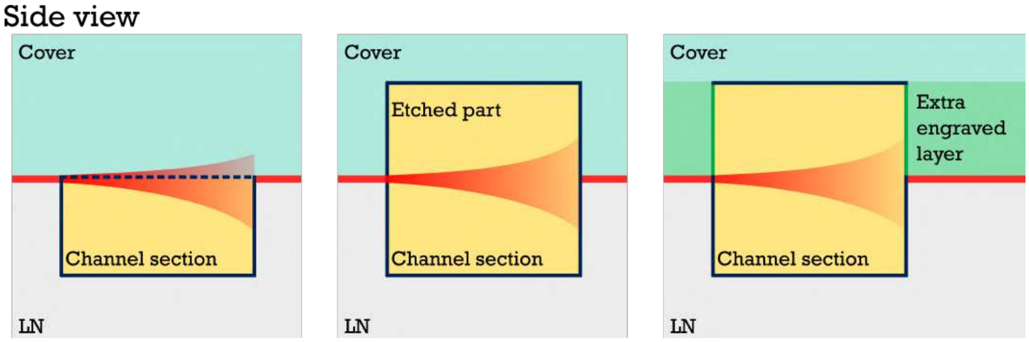

Figure 3.10. Side views of the possible configurations to adjust the position of the waveguides output respect to the height of the channel. On the left, there is the standard configuration used in this work, where the waveguide is on the upper edge of the channel and part of the light interact with the cover. In the center, the configuration of the channel can be changed by means of chemical etching inside the channel, since the substrate and the cover material can exhibit different chemical resistance, such as polymer or glass and lithium niobate. The final sketch represents a possible solution to tuned the position of the waveguide output respect to the channel height, just by tuning the height an extra deposited layer(either polymeric or crystal) before the engraving of the channel.

Furthermore, the alignment of the two sides of waveguide is naturally achieved in a perfect way, thus making the fabrication of the device straightfoward compare to the chips, where fibers are embedded and glued. Moreover, the direct facing of the waveguide inside the channel gives to the optical measurement a local behavior, since the source inside the channel has $5\,\mu\mathrm{m}$ width. This feature makes the system unique to the our knowledge, in particular the combination of such thin optical probe inside a microfluidic channel combined with high portable and integrated chip.

Since the waveguide output ends directly on the channel walls, the transmission of the light across the channel between the two aligned waveguide depends on the index of refraction n_{ch} inside the channel. Indeed, the numerical aperture $NA = n_{ch} \sin\theta$ of the waveguide inside the channel describes the cone of light θ. In particular, depending on n_{ch} the θ changes, since NA is constant given by the waveguide features, thus increasing amount of light recoupled light across the channel. This behavior was confirmed by the transmitted shape output in figure 3.9. Figure 3.9 proved the optofluidic coupling of the device, since the optical transmission is effectively influenced by the liquid inside the channel.

3.3.1 Two phase systems optical transmission signal

The optical transmission signal from the described coupling is even more sensitive to the flow inside the channel of an object. This effect is due not only for the eventual index of refraction contrast with the surrounding medium inside the channel, but also for the presence of interface which can scatter light and for the eventual absorbance of the object material. The generic description of the object is given to highlight the wide range of application of this system. In particular, water droplets in hexadecane were fluxed inside the channel to demonstrate the signal sensitivity of the coupling. In this case instead of the shape of the output the intensity was monitored during the time of the passage of each droplet.

As reported in figure 3.11, the droplet signal is characterized by two peaks corresponding to the meniscus and a plateuax during the droplet passage. As expected the droplet plateaux is significantly lower than the signal in the presence of oil in front of the waveguide, due to the scattering of the interface and the refractive index contrast of water with the hexadecane. Instead, the peaks can be explained mainly as a lens effect from the meniscus shape. This feature is really interesting because also the geometrical information can be obtained from such signal. In figure 3.12, the reproducibility of such feature can be appreciated, thus opening a future investigation on the morphology analysis. This characterization is feasible only thanks to the local probing nature of such fabrication technique.

In the next chapter several application based on the signal will be presented.

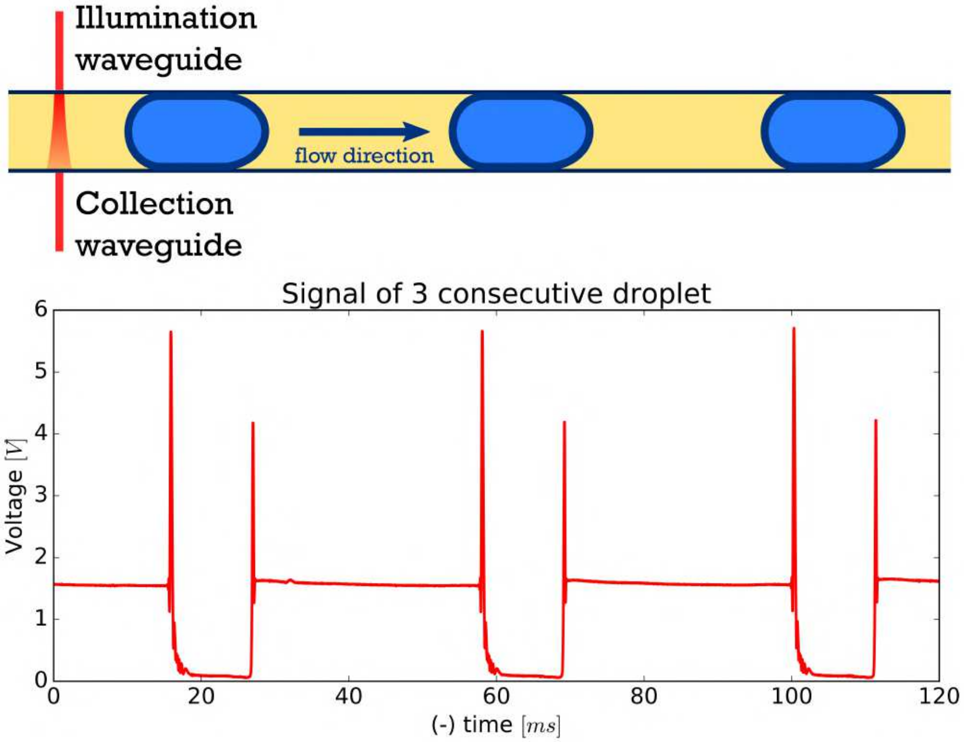

Figure 3.11. Sketch of the optofluidic coupling working principle for droplet passage. The droplet in front of the waveguide scatters light because of the interface and refractive index contrast, thus presenting a lower signal compare to the channel filled with heaxadecane. Such plateaux is characterized by two peaks during the meniscus passage, which probably act as lenses coupling more light inside the collection waveguide.

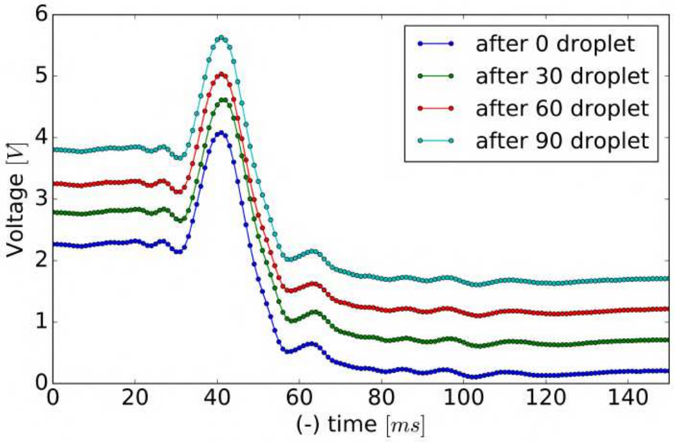

Figure 3.12. Highlight on the signal corresponding to a meniscus. Different signals are reported after several droplets, in order to demonstrate the reproducibility of the signal. Each signal is shifted in the y only for visibility reason, all the four are perfectly matching each others.

Chapter 4

Applications: new approaches of optical sensing in $LiNbO_3$

The $LiNbO_3$ chip with Ti-indiffusion waveguides and engraved microchannels can exploited for several applications, both in lab-on-a-chip field and optofluidics. Indeed, the waveguide optical transmission signal is demonstrated as a reliable probe for the liquid and object flowing in the microchannel. The optical probe in such an integrated way is an essential feature for every lab-on-a-chip application [14], and requires an optical study of objects inside a microfluidic channel. The interaction of the objects inside the channel and the light from the waveguides depends on the optical properties and interfaces of the objects and the medium. This interaction can be studied by the transmission optical signal and all this properties affect directly this signal. Therefore, the waveguide output represents a feasible tool for the measurement of those objects properties, in an integrated and portable $LiNbO_3$ chip. This novel stage represents an implementation of the toolkit provided in a monolithic substrate of $LiNbO_3$, thus getting closer to a multifunctional lab-on-a-chip in $LiNbO_3$.

Furthermore, the interaction between the microfluidic channel and the light from the waveguide allows for controlling the optical transmission by a microfluidic. The control on the liquids in microfluidic channel can be transduced in a control over the transmission signal.

In this chapter some applications of the coupling between Ti-indiffusion waveguides and engraving microchannels in $LiNbO_3$ are presented as follows:

4.1 This section describes an optical trigger for the flowing objects inside the channel. This platform based on the waveguide-channel measured the frequencies and the time passages of objects flowing inside a channel. The performances are compared with standard devices typically used for this application.

4.2 The previous section platform can also measure several shape properties of the objects. In this section this features is highlighted, in particular the coupling of a droplet generator demonstrated how the device can be sensitive to the droplets lengths, velocities and some shape changes during transitions between different droplets generation regimes.

4.3 In the section a slightly different chip is presented: the photonic configuration is a Mach Zenhder interferometer. This structure was exploited to achieve a velocimeter with two spatial trigger-point-references.

4.4 This section describes a novel integrated device for the pH titration, it exploits the optical transmission signal as a probe for the absorbance measurements of a solution with pH indicator. The optical absorbance of a pH indicator changes drastically with the pH of the medium, and thanks to this properties the device can be used for the determination of the pH of a solution.

4.5 Finally a section dedicated on an application where the microcahnnel tool is used to control the optical transmission signal. An optical stage controlled by the liquid inside the channel is presented. Essentially, the refraction of the light beam from the waveguide is driven by the liquid refractive index inside a channel, which is tilted and not perpendicular to the waveguide propagation direction.

4.1 Optical trigger

The first straightforward application of the waveguide-microchannel coupling described in the previous chapter is an optical trigger for detecting flowing objects inside a channel. As a matter of fact, the signal of a droplet in section 3.3 brings the information of the passage time of both meniscus in front of the waveguides. As a consequence, the alternation of the continuous phase and the droplet is described by an intensity peak and a subsequent drop of the signal (as far as the dispersed phase has a index of refraction lower than continuous one, the vice versa happens for a refractive index higher for the dispersed phase.) Similarly, the transition from a droplet to the continuous phase is identified by a rise of the signal and subsequent peak (see figure 4.1). These fingerprints play the roles of trigger signal and it can be used to identify frequencies as well as the intervals between two subsequent passage.

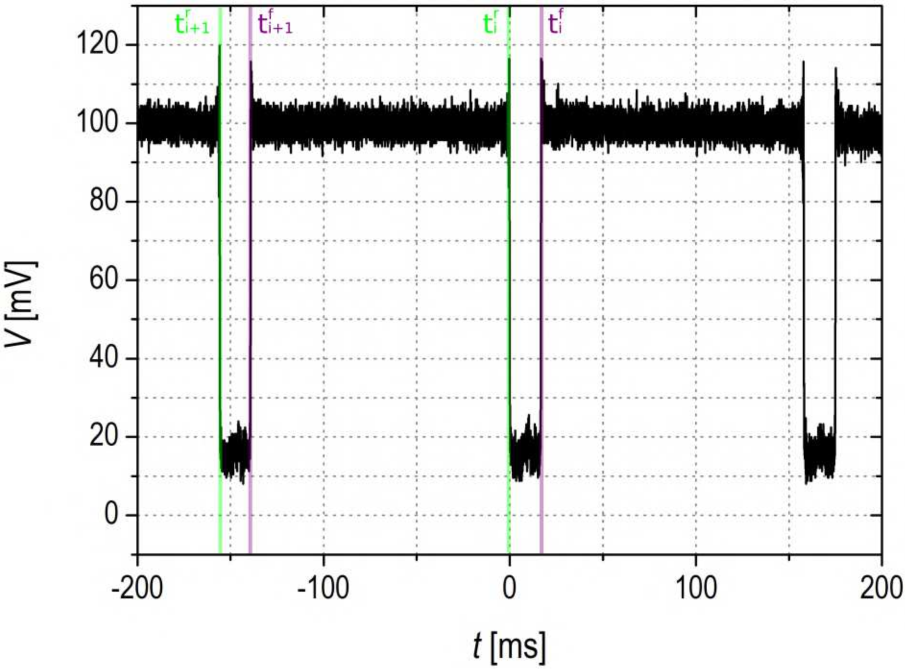

Figure 4.1. Example of three consecutive droplets signals, where in the bottom figure are highlighted the trigger times: in green the front meniscus signal, in violet the rear meniscus.

For instance, following the sketch in figure 4.1, the trigger time for the rear meniscus of i-droplet is the violet time t_i^r, whilst the front meniscus of the analogous droplet is in green t_i^f. The time interval between two menisci with the same curvature can be calculated as $\Delta t^r = t^r_{i+1} - t^r_i$ or $\Delta t^a = t^f_{i+1} - t^f_i$, as well as the time interval for the passage of the i-droplet $\Delta t = t_i^r - t_i^r$. Both time intervals have a crucial geometrical meaning, since Δt^r and Δt^a are the inverse of the frequency, and the Δt is proportional to the velocity and the length of the objects. Therefore, the determination of these trigger times is essential for the calculation of all the interesting physical properties of flowing objects. For this reason, the definition of a procedure for trigger times determination is mandatory, in order to define and measure a reliable time instant and its error. An highlight of the meniscus signal was given in 3.12, where that reproducible signal represents a fingerprint of the meniscus shape. Nevertheless, an univocal estimation was needed to define a time instant, which in this section was considered from the high slope part of each meniscus signal. From the statistical analysis of a large number of droplets trains, it emerged that the best physical quantity representing the beginning (and the end) of a meniscus is the instant t corresponding to the full width at half maximum (FWHM) of the recorded signal, taken with respect to two adjacent plateaus (continuous and dispersed phases respectively), as showed in figure 4.2.

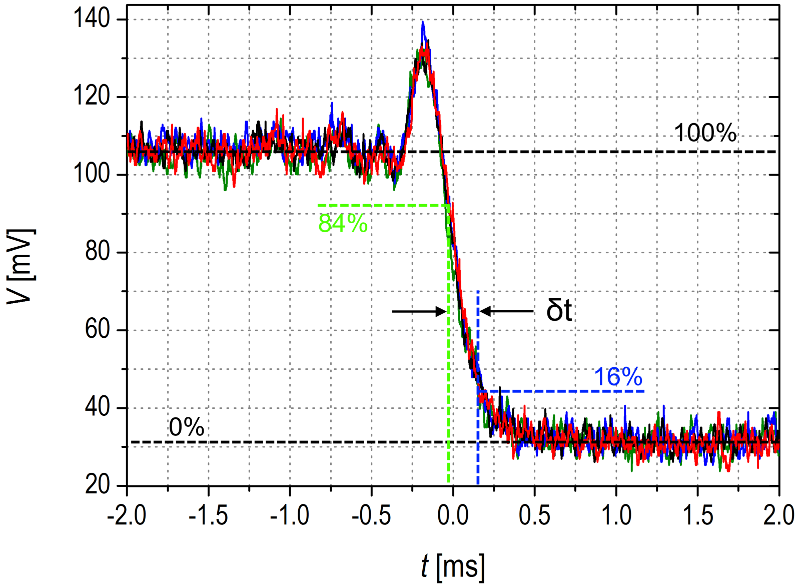

Figure 4.2. Example of the overlapping of the signal from four different on the front meniscus, where it is also depicted the estimation δt of the uncertainty related to a rise/drop of the signal. Blue lines refer to the $16\,\%$ of the average rise/drop of the signal, in the same way light green lines refer to the $84\,\%$.

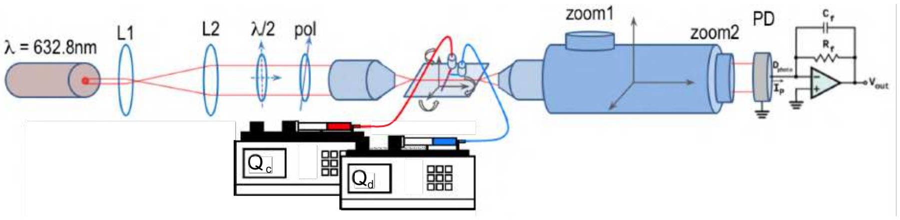

Figure 4.3. Sketch of the experimental setup. A $632.28\,\mathrm{nm}$ *He-Ne laser was enlarged by two lens (L1,L2) to properly fit the pupil of the objective, then a half wave plate and a polarizer allow the choice of the polarization. The light recollected by a near field system were analyzed by silicon photodiode. The current signal was then transduced and amplified into a Voltage value by mean of a transimpedance amplifier. Two syringe pumps control the flows of continuous and dispersed phase respectively.*

4.1.1 Optofluidic setup for droplet optical trigger

The demonstration of how this coupling can be used to trigger an object inside a microchannel was performed by the device with the glass cover described in section 2.1 in figure 2.6. The main substrate was made by $LiNbO_3$ with the integration between the Ti-indiffused waveguides and a T-junction droplets generator. The optofluidic setup (figure 4.3) for the measurements consisted in: a He–Ne laser (wavelength = $632.28\,\mathrm{nm}$, power = $1\,\mathrm{mW}$) was coupled into one waveguide of the device by means of the near field system described in section 3.2. The alignment between the beam and the waveguide was achieved by a six degrees of freedom micropositioner. The chip holder allowed the fluidic connection with two independent syringe pumps (PHD 2000, Harvard Apparatus), and the generation of droplets was achieved by a T-junctions, such as the one described in section 2.2. The two liquids were: MilliQ® water for the dispersed phase ($n = 1.332$ at $632.28\,\mathrm{nm}$), and hexadecane with a concentration $0.08\,\%$ (w/w) of SPAN®80 ($n = 1.434$ at $632.28\,\mathrm{nm}$). When passing in front of a waveguide, the droplets interact with the light from the input waveguide, and the output waveguide collects the transmitted light across the microfluidic channel. The output was read by a silicon photodiode and amplified by mean of a transimpedance amplifier. Finally, the analog signal was digitalized through an oscilloscope MSO-X 2012A (Agilent Technologies, Santa Clara, California, USA). The device was tested with this setup at different droplet lengths and frequencies. The continuous phase flow Q_c values tested were 10, 20, 30 and $40\,\mathrm{mL\,min^{-1}}$, for each of which the dispersed phase flow Q_d was modified accordingly to Q_c, in order to obtain the ratio $\phi = \frac{Q_d}{Q_c}$ equal to 0.1, 0.2, 0.4, 0.6, 1, 1.2 and 1.5 These flows correspond to a range of frequencies from $2.2\,\mathrm{Hz}$ to $121.9\,\mathrm{Hz}$ and a range of droplets volume from $4.69\,\mathrm{nL}$

to $15.7\,\mathrm{nL}$. The same experiment was compared to those acquired in real time imaging of the droplets flows using a standard setup (i.e. an inverted microscope coupled with a fast camera) described in [6], by way of comparison.

4.1.2 Optical trigger performances

The optical triggering achieved by the presented opto-microfluidic platform was finally compared with standard imaging technique. Firstly, one clear improvement respect to standard technique is the exploitation of a voltage signal, which requires a faster and more portable hardware for a real time analysis compare to the videos, obtain by the standard setup. Moreover, the platform is itself really compact compare to the bulky microscope and camera usually exploited for these kind of measurements. Even if the high recording speed cameras have nowadays compact sizes, the voltage signal given by the opto-microfluidic platform provides higher integration and several advantage from multiple point of views: the storage price is way lower than the video, and the real time analysis does not require as much computational power as the video analysis does, and also it can be performed by an electronical circuitry, thus guaranteeing more compactness.
The performances comparison was carried out by focusing on two droplets properties: the time passage Δt and their frequency $f = 1/\Delta t^d$. Δt for the optical trigger was measured as described in previous section in figure 4.1, while imaging approach used the whole video: and $\Delta t = Lv$ with L and v was calculated for each frame for each droplet, by standard tracking software [6]. Δt_d is measured as N/T from the video analysis, where N is the number of droplets flowed in the time interval T. Instead it could be measured in two ways from the optical trigger either by Δt^r or by Δt^a. The relative difference $(\Delta t^r_{av} - \Delta t^a_{av})\Delta t^a_{av}$ never exceeded $0.2\,\%$, and their dispersion was compatible within $10\,\%$. It is worth mentioning that no systematic trends between Δt^a_{av}, Δt^r_{av} across the tested rates was measured, as confirmed also by residuals and covariance tests of cross-linked quantities. The statistical analysis evidenced that there is no distinction in preferring one or the other parameter (Δt^a_{av}, Δt^r_{av}) as an estimator for the droplets frequency. The uncertainty estimation on each single trigger time, described in figure 4.2, depends on the speed and the shape of the droplets, and consequently on the flow rates employed. The δt ranged from $377 \pm 4\,\mathrm{\mu s}$ at a flow rates $Q_c, Q_d = 10, 1\,\mathrm{\mu L\,min^{-1}}$ to $50 \pm 1\,\mathrm{\mu s}$ at $Q_c, Q_d = 40, 60\,\mathrm{\mu L\,min^{-1}}$. These values are extremely low respect to the time intervals between two droplets. The ra-

tio between δt and Δt^a_{av} spreads from $0.4\,\%$ for first case ($\Delta t^a_{av} = 11.21 \pm 0.03\,\mu s$ $Q_c, Q_d = 40, 60\,\mu L\,min^{-1}$) to $0.1\,\%$ for the second one ($\Delta t^a_{av} = 369 \pm 6\,\mu s$ $Q_c, Q_d = 10, 1\,\mu L\,min^{-1}$). Moreover, δt results to be very small also compared to the time of passage Δt of a single droplet, less than $0.8\,\%$ for all tested rates. The δt is always related to a correspondent δV, which depends on the sensitivity of the instruments to distinguish the two plateuax. In general terms, δV is always related of the refractive index difference between the object and the medium, and also to the object shape. Therefore, δV can vary depending on the application, and the sensitivity of the system have to be tuned accordingly. As an order of magnitude, the minimum δV variation that can be detected is 2 time the value of the noise dispersion. Firstly the stability of the coupling should avoid any noise higher than δV, in the case of our setup is always less than $1\,\%$ of the transmission without objects. However, this can be easily reduced further with the pigtailing. Secondly, the acquisition system can influence the overall sensitivity, which mostly depends on the Analog to Digital converter. In particular, the measurements of the next section will show an upgrade in terms of sensitivity of the system in both of this two aspects.

Both measured parameters (Δt, Δt^d) were compared between the two systems (Video camera setup, optical trigger) as showed in figure 4.4.

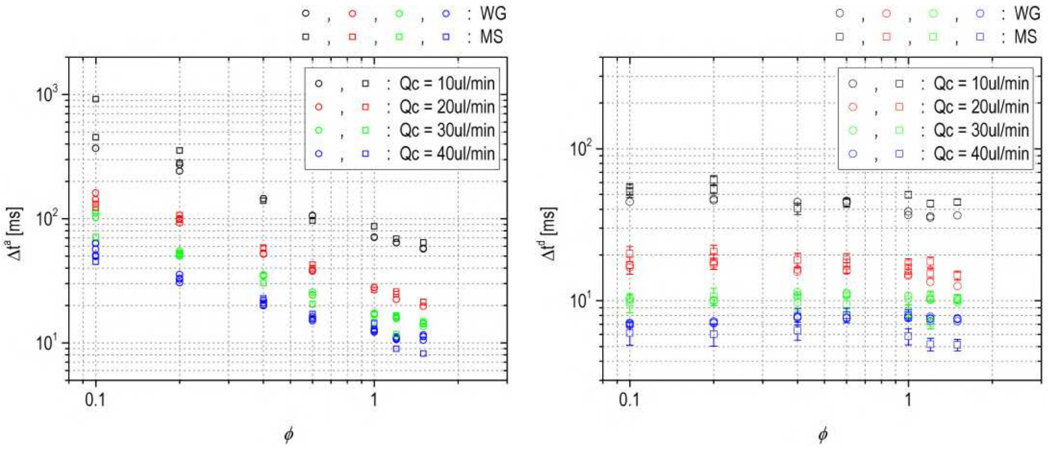

(a) (b)

Figure 4.4. Comparisons between the microscope setup system (MS) and the droplet measured with the optical trigger system (WG) here presented: on the left Δt^a , on the right Δt_d.The Logarithmic scales were set for a better visualization. Error bars were not drawn for the sake of clarity (markers size is bigger than errors). All repeated measurements were reported when available.

Both graphs showed an overlapping of the data from the two systems, proving that optical trigger measure both Δt, Δt_d in a reliable way, thus demonstrating the accuracy of the opto-microfluidic system. The precision of the latter was also significantly higher than the standard approaches, as reported in figure 4.5, where the dispersions are plotted for each values of Q_c at each dispersed flow rate Q_d. As it can be noted from figure 4.5, apart from few points at the lowest flow rates, the optical trigger is characterized by a significant lower dispersion in the determination of Δt, in average the optical trigger dispersion is more than $0.5\,\mathrm{t}$imes of microscope dispersion. In particular, the microscope setup dispersion is constant and does not show any evident trend depending on the microfluidics setup (as evident when looking at the σ dependence on ϕ). While, the optical trigger follows a decreasing trend (lower dispersion increasing ϕ), thus demonstrating that it is mainly affected by the natural droplet size dispersion due to the generation process. Indeed, the droplet generation fluctuations are expected to decrease with the increase of the flow thanks to the greater system stability.

Finally, another advantage of the opto-microfluidic tool compared to the standard systems is the sample rate acquisition. A standard system requires expensive cameras with high recording speeds for an high acquisition rate, and even if the technology of such cameras is always improving, the price and the sizes increase exponentially accordingly with the performance. While the optical trigger can easily reach several tens of kilohertz with a standard analog to digital converter, or even the signal can be read in an analogically way exploiting electronic circuitry.

In conclusion, the voltage signal output of the opto-microfluidic platform exhibited an high reproducible and stable behavior throughout a wide range of droplet volumes and velocities, and the data follows the same trends observed in microscope-based analysis, but showing less dispersion. The comparison with the microscope-fast camera method highlighted the good performances of the $\mathrm{LiNbO_3}$ device, which reduced the signal reading dispersion of more than $50\,\%$ respect to the standard setup. Moreover, the droplet signal profile showed how the shape of the voltage signal is directly determined by the droplet size and geometry. The beginning and the end of each droplet can be thereby clearly distinguished and associated with the rise and fall of its corresponding optical signals. These results confirm how a sensor stage for flowing object triggering can be integrated in every $\mathrm{LiNbO_3}$ optofluidic devices. This system can be useful for several practical applications, such as counting either biological analytes before a specific analysis, or either droplet of strong chemical reagent, exploiting also

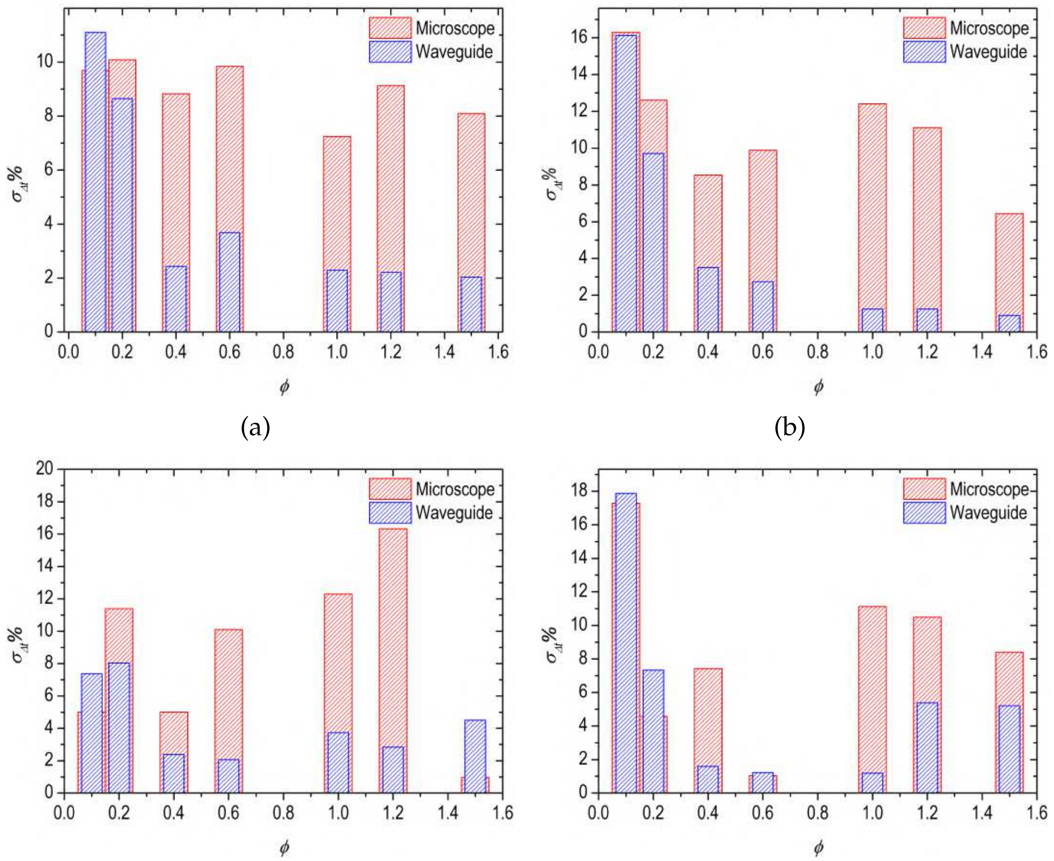

(a) (b)

(c) (d)

Figure 4.5. Comparison between the dispersion σ of Δt^a obtained with the microscope setup system (red bins) and with the optical trigger system (blue bins), for each tested ϕ and Q_c: $10\,\mu\mathrm{L\,min^{-1}}$ on the top left, $20\,\mu\mathrm{L\,min^{-1}}$ on the top right, $30\,\mu\mathrm{L\,min^{-1}}$ on the bottom left, $40\,\mu\mathrm{L\,min^{-1}}$ on the bottom right.

the biological compatibility and chemical resistance of this material. This trigger can be also used as a feedback system to select specific droplets with a desired length and velocity, in combination with the piezolectric sorting tage in $LiNbO_3$. In general, the presence of a fully integrated and self-aligned optical stage, i.e. the waveguides array, can also allow performing a wide range of optical investigations, such as absorption or fluorescence measurements, suitable for deriving physical and chemical properties of droplets.

4.2 Droplet shape optical analysis

The previous section showed an application on how the optical interactions can be used to measure some properties of flowing droplets inside the microchannels. Although the interesting results obtained, it is clear from the signal in figure 4.1 that the optical interaction with the droplet represents a finer probe of optical and geometrical properties of droplets, such as refractive index, menisci curvature and position inside the channel. This section is focused on the investigation of how droplets shape affects the optical signal of the optical trigger device and, consequently, how this optical probe can be exploited to analyze droplets shape features, such as meniscus curvature, droplet volume and length and the section of the droplet inside the channel (figure 4.6). The measurements of these properties are crucial not only for a better understand of the droplet fluidodynamics system behavior, but also for several application in microfluidic, such as measuring the volume of droplet for drug delivery applications [146]. The figure 4.6 shows a slightly different droplet signal, in fact a deeper analysis on the droplet shape requires an increased sensitivity and a better resolution of the signal respect to the previous one (figure 4.1). An upgrade was performed on the setup: the coupling and the waveguide quality were significantly improved by means of a standardization of the fabrication procedure and a better optical setup, an Analog to Digital converter with a better resolution was introduced, and pressure pumps with flowmeters to control better the flow rates. The new setup is depicted in figure 4.7, where an acquisition fast card Ni 6023 (200KHz maximum frequency and 0.0023mV sensibility, NIST) collects the signal from photodiode and a pressure pump OB1 MK3 pressure driver pump with 3 channels[1] with a range $0\text{-}8\,\mathrm{bar}$ (Elveflow, Paris, France). The flow control was obtained by a feedback system provided by the coupling of three flowmeters BFS Coriolis[2] (Bronkhorst, AK Ruurlo, Holland).

These expedients allow for the detection of new fingerprints of the signal, in particular a more extensive behavior due to the meniscus signal. An interesting new feature is the minimum before and after each meniscus peak, since it represents a clear fingerprint of the first interaction of the droplet with the waveguided beam. Although the previous determination of the triggering time guarantees a fine determination of the frequency, in the case of a deeper analysis on the droplet

---

[1] resolution: $0.006\,\%$, stability: $0.005\,\%$, response time: $9\,\mathrm{ms}$.

[2] accuracy: $0.2\,\%$, response time: $35\,\mathrm{ms}$

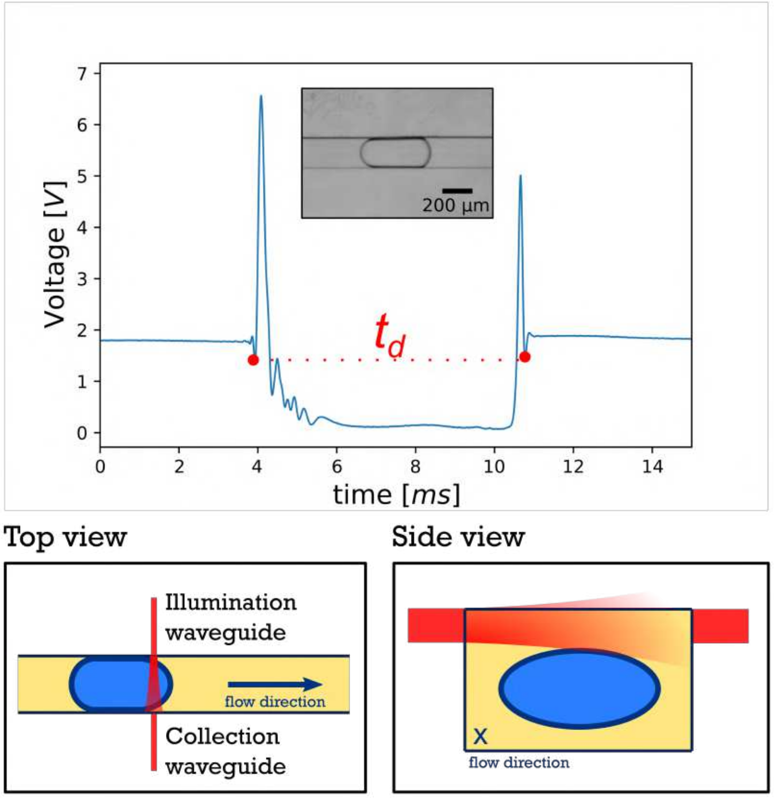

Figure 4.6. Sketch of the droplets trigger system: on the top droplet signal from the upgraded device of the droplet in the inset picture. The time passage is calculated in-between the two red points, which are the starting and ending interaction instants. On the bottom the two views of the channel during the interactions. In particular, the side view shows the starting (ending) time instant of the interaction.

shape a different indicator was needed. For this reason, the optimal indicator was the minimum, which gave a clear determination on the starts of the interaction between droplet and light. Moreover, the aim of this shape analysis was to give a preliminary insight on the study of the shape of multiple droplets, in order to gain more information of the droplet generators behavior. So, the statistical focus given to indicator to estimate the single object time passage was not needed as in the previous application, since the measurements were always considered a multitude of droplets. The distribution of the droplets shape are usually much higher than the error due to the estimation of the indicators. For this reason, in this section only the minima were considered as indicator, after a test on their reproducibility.

Thanks to the new capability of the improved setup, the measurements of volume can be easily achieved in a device that integrates on the same substrate both

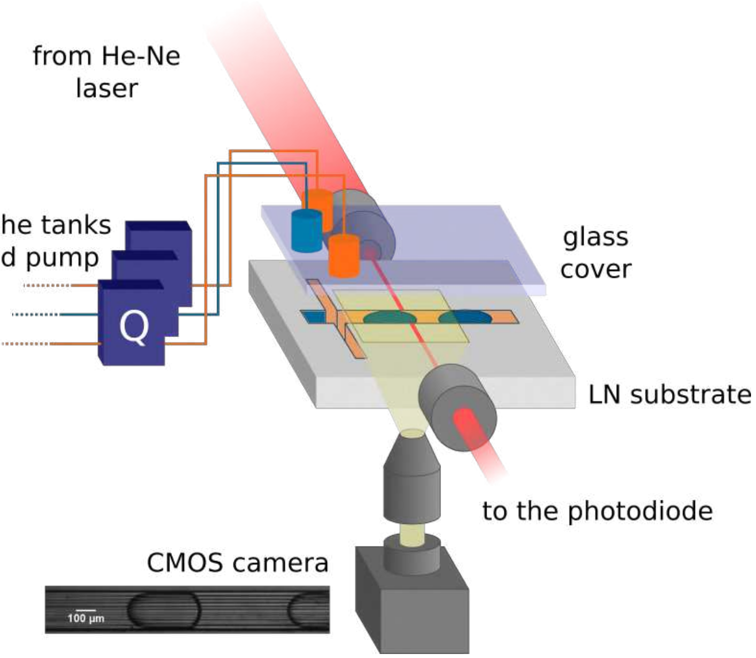

Figure 4.7. Setup for the droplet shape measurements: the optical transmission signal from the waveguide is studied by near field setup and simultaneously the video is recorded by an imaging system with a fast camera acA800-510um^3 *(Basler, Ahrensburg, Germany) on the bottom of the sample.*

a droplet generator (in particular in this case a Cross-junction) and a waveguide system described in this thesis. Indeed, the time interval between two consecutive droplets is the period of the production frequency and for the mass conservation:

$$V_{dr} = \frac{Q_d}{fq} = Q_d t^d \tag{4.1}$$

where V_{dr} is the volume of the droplet, Q_d is the flow rate of the dispersed phase, and fq is the generation frequency of the droplets. The t^d can be detected by the waveguides transmission signal and the Q_d can be measured by a flowmeter. The measurement of Q_d should consider the eventual difference in flow rates due to the system relaxing time, such as tubing expansion. In particular, the $LiNbO_3$ guarantees a high rigidity compared to the standard polymeric devices and, as explained in the section 2.2.2, the stability check before each measurement ensures that Q_d measured correspond to the actual one inside the dispersed microchannel. Therefore, the setup rigidity, the high sensitivity of the flowmeter and of the optical trigger allow for an indirect measurement of the volume as describe din equation 4.1. In figure 4.8 the volume analysis for the Cross-junction is showed: the data follows the expected trend for the volumes described in 2.2.

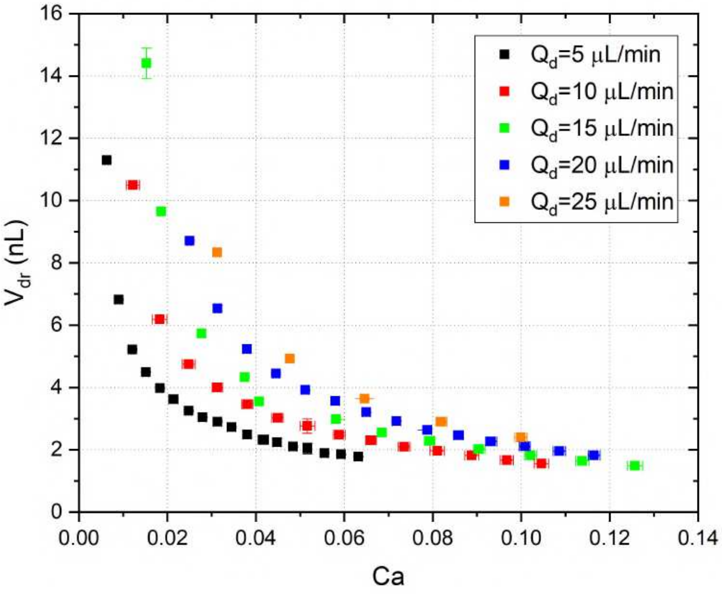

Figure 4.8. Cross-junction measurements of the volume, calculated as droplet production frequency multiplied for the dispersed phase flow. The error is always lower than $3\,\%$ *and distribution respect the behavior described in 2.2 for every value of* Q_d.

The data was obtained by means of the generation of more than $300\,\mathrm{droplets}$ for each flow rates combination. This number was chose as a good compromise to have high acquisition frequency to distinguish all the features of the signal, high statistical significance and at the same time reasonable file sizes. However, the device canperform single droplet measurements once characterized the behavior, as far as continuous measurements once realized an electronic to perform an in-line analysis.

For each point of the plot, the frequency was measured by means of the optical trigger, and in particular from the inverse of the average period between: the time periods between two consecutive front menisci signals, and the same for the rear meniscus. From this analysis, the volume averages and its error were obtained by the multiplication with the flow rate averages during the droplet generation measured by the flowmeter BFS Coriolis[4] (Bronkhorst, AK Ruurlo, Holland), which is also used as feedback for the pumps of the setup, described in figure 2.16. For

---

[4] accuracy: $0.2\,\%$, response time: $35\,\mathrm{ms}$

each droplets sequence, the volume error never exceeded $3\,\%$, thus confirming the outstanding performances of the devices, previously presented. Moreover, the volumes follow the standard power law scaling laws respect to Ca derived from the one for the frequency (scaling law for frequency in equation 2.10), confirming the feasibility of droplet generator in lithium niobate.

Another geometrical property that can be measured from the optical transmission signal is the droplets length, because t_d is proportional both the velocity and the length as follows:

$$t_d = \frac{L_{dr} - \Delta L}{v_{dr}} \tag{4.2}$$

where L_{dr} and v_{dr} are the length and the velocity of the droplet respectively, and ΔL is the difference due to a trigger mismatch. The waveguide position (see figure 4.6) is on the edge of the channels and the trigger time corresponds to the instant when droplet interacts with the light from the waveguide. This instant cannot correspond to the one given by the most advance part of the droplet is in front of the waveguide. In fact, the droplets menisci have a cup shape and their curvature shape must be taken into account. Basically, the time passages measured do not correspond of the ones of the droplet but the ones of the interacting spacial parts of the droplets, which is smaller than the droplets length. Nevertheless, the system can be calibrated by an analysis of ΔL, which is constant varying the flows if the droplets curvature remains constant. The analysis was performed by a simultaneous video recording and waveguide triggering of the flowing droplet, done by the setup schematized in figure 4.7.

The relationship between the actual L_{dr} and the one extracted from the time passage was studied for Cross-junction in figure 4.9 for a range of $\frac{L_{dr}}{w_c}$ between 0.78 and 4.4 In this range the droplet production regime changed from the squeezing and to the dripping. The plot in the figure 4.9 shows clearly two regimes in the relationship between the actual droplet lengths and the ones estimated from the time passage. The reason for this knee trend is clearly due to the change of curvature of the droplet during the squeezing dripping transition, which affects the trigger instant and consequently ΔL. In particular, in both regimes the curvature does not change with the variation of the flows, neither Q_d nor Q_c. Two linear interpolations were made (gray lines in figure 4.9, the logscale is the reason for an apparent non linear behavior of the lines): the first one (dashed line)for $L_{dr}/w_c = [1.5, 5]$ with slope 1.01 ± 0.01 and intercept

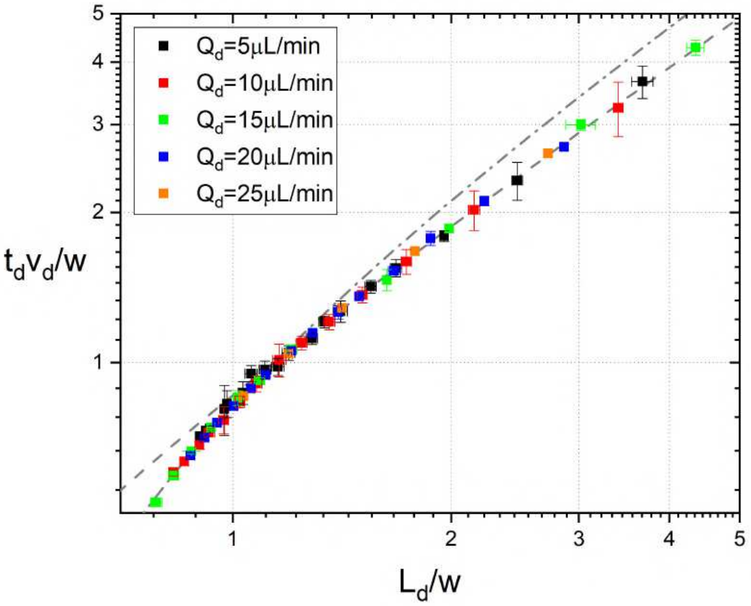

Figure 4.9. Plot of comparison between the two simultaneous measurements of the droplets lengths in the cross-junction configuration. The dashed lines represents the two linear regression of the data two regimes. As expected the relationship of the two lengths does not depends on Q_d. For a better visualization of the two trends both axes are in log-scale.

of $-0.15 \pm 0.02\,(R^2 = 0.999)$, the second one (dashed-dotted line) fits the data $L_{dr}/w_c = [0.1, 1]$ with slope 1.29 ± 0.02 and intercept of $-0.47 \pm 0.02\,(R^2 = 0.997)$. In the first regime, where the droplets are longer than the channel (i.e. squeezing regime), the slope is compatible with 1, as expected, and so the intercept can be considered as an estimator of $\frac{\Delta L}{w_c}$. This calibration is constant over all the squeezing regime range, and it allows the measure by this system of the lengths of droplets inside the microchannels with using only the waveguide signal.

In the second regime, the same considerations cannot be done. In this case, the slope is not compatible with 1, and so $\frac{\Delta L}{w_c}$ is not equivalent to the intercept. In the dripping regime the trigger instants change with the flow rates, due to the curvatures dependencies on the flows. The droplet in the dripping are not affected by the channel boundaries, as the squeezing regime, and so the droplets curvature depends strongly on the flow rates. This dependence did not allow for a description by same constant $\frac{\Delta L}{w_c}$ for droplets during both regimes. Nevertheless, the behavior of L is still linear, thus suggesting that $\frac{\Delta L}{w_c}$ is still in a linear dependency on the velocity, and consequently the time intervals has a linear trend compared to the velocity. This linear behavior allows the calibration of the device for the measurements of the lengths in this regime, thus expanding the length range of the device even to the dripping regime.

4.2.1 Transition from squeezing to dripping

The droplet curvature has a strong influence on the optical transmission signal, since the latter is the result of the interaction of the light from the input waveguide and the droplets surfaces. An analysis of this interaction was performed by the generation of several droplet shapes, with different curvatures exploiting different droplets generation regimes. As mentioned before, the droplet during the squeezing to dripping transition has drastic shape modification, due to the presence of the channel walls. In the following figure 4.10 this transition of the signal is showed.

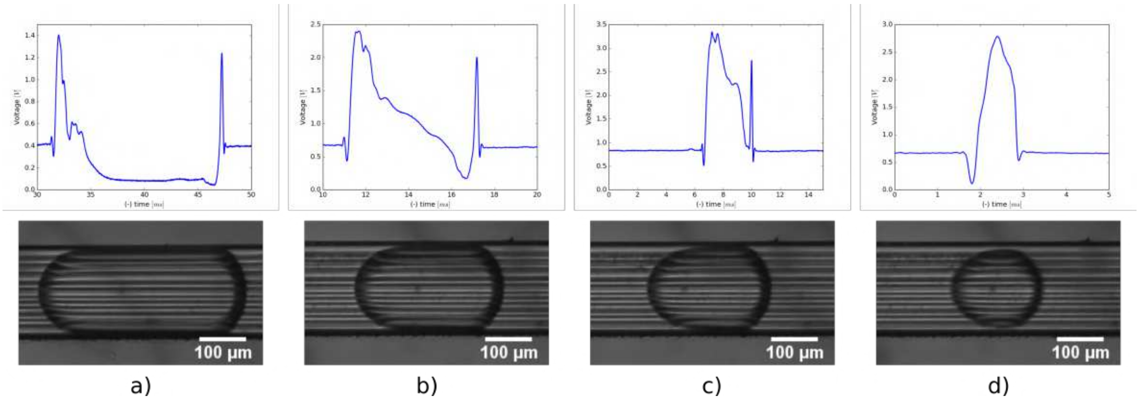

Figure 4.10. Different droplets signals and their corresponding images. In all droplets images, they are flowing from right side to left side. Figures a) and b) represent droplets in the squeezing regime, c) refers to a droplet in the transition regime, and finally the d) is a droplet in the dripping regime. The signals on the top have drastic changes during the transition: the plateau, first, modifies in the only one point then its value increase, and finally two peaks become only one. The flows in the figures change as follows: $Q_d = 10\,\mu\mathrm{L}\,\mathrm{min}^{-1}$ *for every one, a)* $Q_c = 20\,\mu\mathrm{L}\,\mathrm{min}^{-1}$*, b)* $Q_c = 40\,\mu\mathrm{L}\,\mathrm{min}^{-1}$*, c)* $Q_c = 60\,\mu\mathrm{L}\,\mathrm{min}^{-1}$*, d)* $Q_c = 120\,\mu\mathrm{L}\,\mathrm{min}^{-1}$.

During the droplet shape change on the bottom in figure 4.6, the time duration of the bottom plateau decreases until it becomes one minimum, then this minimum increase in intensity, and finally in the pure dripping regime the signal presents only one peaks. This transition of the signal is strongly and clearly related with the shape of the droplet, and theoretically the shape of the droplet can be deduced from the signal with the knowledge on the exact interaction between droplet and light inside the channel. However, the interaction can be calculated only knowing the shape of the droplet itself, and the shape is still under investigation. The only studies realized are based on time consuming simulation, as reported in section 2.2. Nevertheless, several results can be obtained on the droplet shape just by simple considerations on the interaction depicted in figure 4.10. The minimum of the droplet signal is the time instant corresponding to the minimum transmission of light across the channel. Since the eventual lens effect of the meniscus shape influences only the peaks, and in general the side part of the signal, the minimum should be affected only from the light that either does not interact at all with the droplet, or partially interacts with droplet interface. The first component is related to the distance between the droplet from the channel cover, indeed, the droplets are never in deep contact with channels surfaces, they are always surrounded by an oil layer. The thickness of this layer depends on Ca by the Bretherthon's law [147], and so during the transition squeezing to dripping. The second component should depend on the side section curvature only (see side view in figure 4.6), which does not change drastically during the transition. Consequently, since this distance variation describes the squeezing-dripping transition quantitatively, the same could be obtained by these minima. In particular, the minimum for i-droplet was calculated as follows:

$$Min(i) = \frac{\min_{t\in\Delta_{dr}(i)} V_i(t)}{\bar{V}_c(i-1)} \tag{4.3}$$

where $\bar{V}_c(i-1)$ is the average intensity signal of the previous plateau of the continuous phase, which allows for a normalization. The average and standard deviation of the distribution of this parameter over $300\,\mathrm{d}$roplets are plotted in figure 4.11 in function of Ca, in order to check the variation during the squeezing-dripping transition.

The transition is well described by this plot, where the minima shows a well-defined linear trends for Ca value higher than 0.03 ($R^2 > 0.99$ for each interpolations), which depends on Q_d. The slopes of the linear interpolations are plotted in the inset, where they show with Q_d with a linear behavior. These considerations can be related directly to the oil layer thickness h, since the minima should be proportional to this properties. In particular, the analysis on this layer can be performed. As expected, the distance between the droplet and channel surface starts to increase at the transition, from the figure 4.11 a quantitative value for the capillary number Ca^* can be extracted by the intersection of the minima average (for values $Ca < 0.025$) and the fits (for values $Ca > 0.03$). Ca^* results are com-

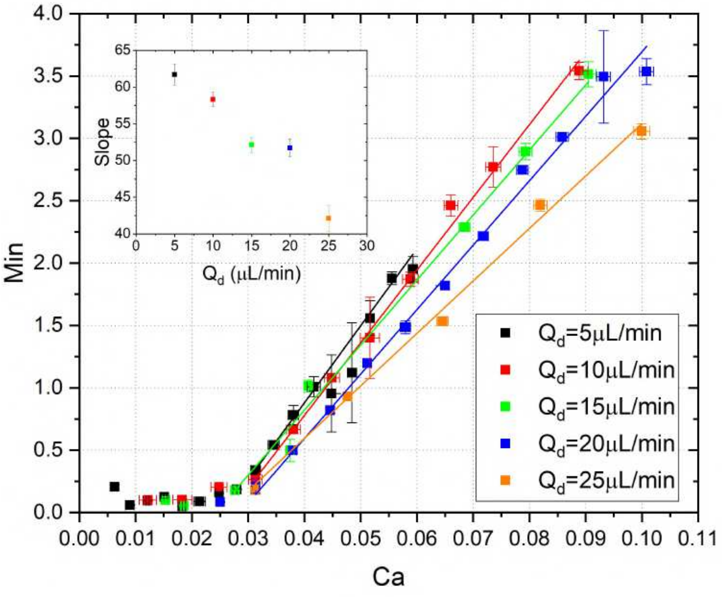

Figure 4.11. Plot of the minimum against the capillary number: a clear transition can be appreciated after almost Ca =0.03 Linear interpolations were realized for Ca higher than this value. The slope of this linear behavior decrease with the Q_d, in the inste this trend is showed.

patible between each Q_d set, and the average of all sets results is 0.026 ± 0.002.

The relationship between h and Min allows for the phenomenological analysis varying Ca. No conclusion can be achieved for values lower than Ca^*, but for higher Ca^* the linear trend of Min should be the same for h. A simple scaling law for h can be suggested based on this simple discussion, even if a quantitative analysis requires a well-defined formula to describe the relationship between h and Min. The simple phenomenological model from the data in figure 4.11 is:

$$h(Ca) = h(Ca^*) + \alpha(Q_d)Ca \quad \text{where} \quad \alpha(Q_d) = \beta + \gamma Q_d \tag{4.4}$$

where α, β, γ are fitting parameters, which can be quantitatively measured from the fits in figure 4.11, once studied the relationship between h and Min. This qualitative analysis represented still a novel method to study shape of the droplet and in particular the squeezing to dripping transition. Future investigations could be open for a quantitative studies.

In conclusion, this system allows for measuring the volume and lengths of Cross-junction generated droplets, and also gives an interesting insights on the transitions squeezing-dripping and droplets shape. Further studies will represent a key step for a deeper investigation on the microfluidic droplet behavior inside the channels.

4.3 Highly sensitive optical velocimeter

The time passage Δt measured by the previous device is an effective indirect measurements of droplets velocity v, indeed $v = \Delta t/L$ where L was their lengths. In that case the measurements of the velocity is always correlated to the length and it requires a calibration step, which can be done by imaging system or other integrated stages. Herein, a solution for a direct optical measurements is proposed. The key innovation behind this upgrade is to use two reference points at a known distance, in order to trigger the object at two different passage times. This improvement can be achieved by exploiting two waveguides as references, the distance between which is known, and measuring the time intervals between two consecutive triggers times. Although this approach is the simple improvements of the system described in section 4.1, it hides some complexities in the synchronization between two triggering times of the passage of the objects across the two waveguides, since the two measurements should be performed independently. In this work a novel solution is proposed to overcome these problems, instead of 2 independent waveguides, a Mach Zehnder configuration was exploited. The Mach Zehnder interferometer (MZI) waveguided structure in figure 4.12 is a well-known configuration for switching application in lithium niobate, exploiting the electro-optic effect [54]. This structure guarantees an independent reading setup for both probe points inside the channel and a integrated synchronization without the need of a post-processing of the signal. Up to author knowledge, there are no analogous integrated device which aims to similar measurements. The working principle of this approach is based on four-time-trigger signals given by: the start of the interaction of the object with the transmission of the arm 1 (referring to the figure 4.12), the same with the one of arm 2, and the two times at which the interaction stops for both arms. This system has the only requirements that the object should present a non negligible optical interaction with the optical transmitted signal across the channel. The MZI configuration guarantees that the optical coupling in each arm is the same of that mentioned in section 3.3. As a consequence, the 4 time triggers correspond to the two drops and two rises of the optical transmitted signal respectively.

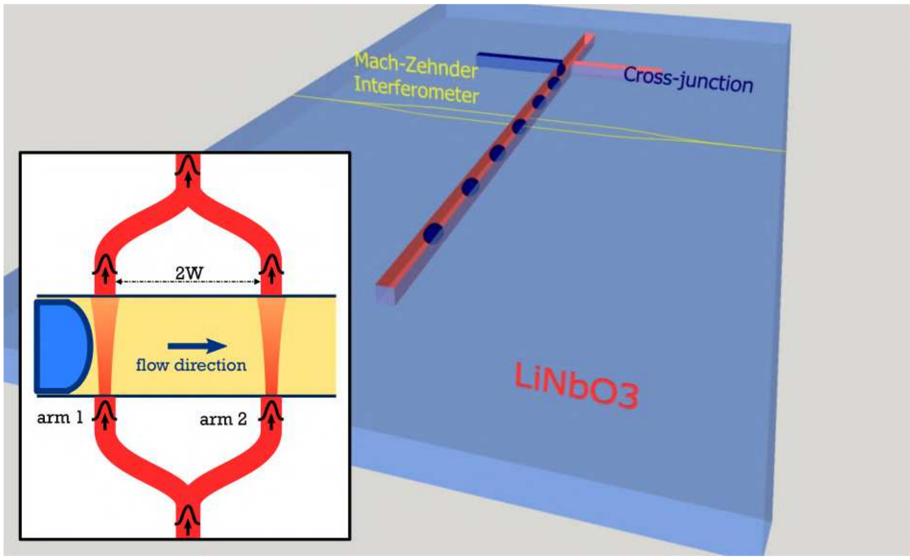

Figure 4.12. Sketch of the working principle of the optofluidic velocity sensor based on a Mach Zehnder interferometer structure. The device consists in the same substrate described in the previous section, but in this one the waveguided structure is a Mach Zehnder configuration, instead of a straight waveguide. In the inset, the working principle is reported, first the light is splitted into two arms divided by a distance $2W$*, then the light independently crossed the channel for two arms and it is recoupled, and finally the signal from both arm is collected in only one waveguide output.*

Although some attempts using such interferometer configuration was already reported in optofluidic applications, no results were published for such velocity sensing application up to our knowledge. Most of published reports exploited this configuration as interferometer for the measurements of liquids refractive index, either without waveguides [148, 149], or using only one arms coupled with a microfluidic channel and the other used as a reference [150–152]. For this reason, a novel design was studied to find the optimal configuration, since the geometric features have strong influences on the optical losses, such as bent part and Y-junction, and they affect drastically the trigger times analysis of the system, such as distance of between the two arms. From this point of view, the geometrical design was a crucial step for an effective realization of such a device, which has to guarantee the best performance as a velocimetry and at the same time a good optical transmission.

During last forty years, several studies were published on the dependencies of the optical losses on the geometrical features of the MZI configuration, since the MZI is one of the most exploited structure for optical modulators [54]. The main crucial parts of MZI from this point of view are the Y-junctions, which acts as a splitter (figure 4.13) [153, 154], the tapered regions [155] and the bending parts [156]. Despite these studies represent a comprehensive description on the optimal configuration, the optofluidic design is different from the one used for the optical modulator, since it has two main constraints on the distance between two arms $2W$. Firstly, the presence of the channel could lead to cross-coupling phenomena, due to the numerical aperture of waveguide illuminating the channels. Indeed, if the dispersion of the light inside the channel from both arm is comparable to $2W$, part of the dispersed light from the arm 1,2 can be couple into the arm 2,1, during the cross of the channel respectively. Secondly, the object interactions with the light for both arms could presented the same cross-coupling phenomena. Therefore, $2W$ should be high enough to avoid any coupling between the light from the arm 1 into arm 2 and vice versa. In particular, in this work the device was tested using water droplet for the validation of the proof of concept. Nevertheless, the application of the device can be extended for every other objects, as long as they have an optical interaction with the arm, and the $2W$ is large enough to avoid this cross-coupling problem. For instance, the extension to solid particles or biological samples is straightforward, once validated the proof of concept with water droplets.

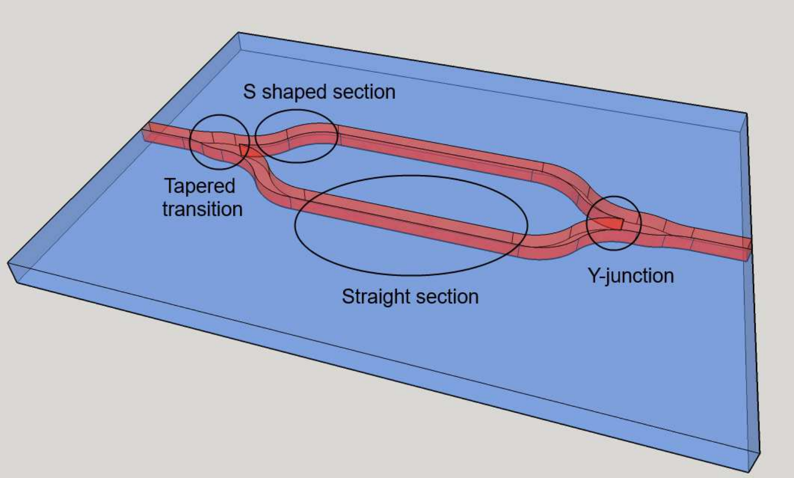

Figure 4.13. Sketch of a standard waveguided Mach Zehnder interferometer. The main parts are highlighted: the tapered region, which is the transition part between the straight waveguide and the Y-junction, the two Y-junctions, which are the correspondence for the beam splitters, the S shape bend and the two straight arms, which together represents the interferometer arms.

Therefore, a proper geometry had to be studied for this application fitting the previous requests, considering that $2W$ (i.e. the distance between two arms) should be higher than the illumination cone from the numerical aperture, in order to avoid the cross-coupling. Another restriction is the fact that the relative largeness of $2W$ and the droplets length could lead to different regimes signal, as showed in the figure 4.14. Firstly, the numerical aperture $NA = 0.13$ (section 3.1) of the waveguide leads to a waist of $13.2\,\mu\mathrm{m}$ at the end of a $100\,\mu\mathrm{m}$ wide channel, thus $2W > 2 \cdot 13.2\,\mu\mathrm{m}$. Secondly, there are four trigger times: t_{11} when the front droplet meniscus passes in front of the arm 1, t_{12} when the front droplet meniscus passes in front of the arm 2, t_{21} and t_{22} are the same for the rear meniscus respectively. In particular, t_{11} and t_{12} are both correlated to a drop of the transmitted optical signal, because the presence of droplet in front of the waveguide scatters the transmitted light. The opposite holds for t_{21} and t_{22}.

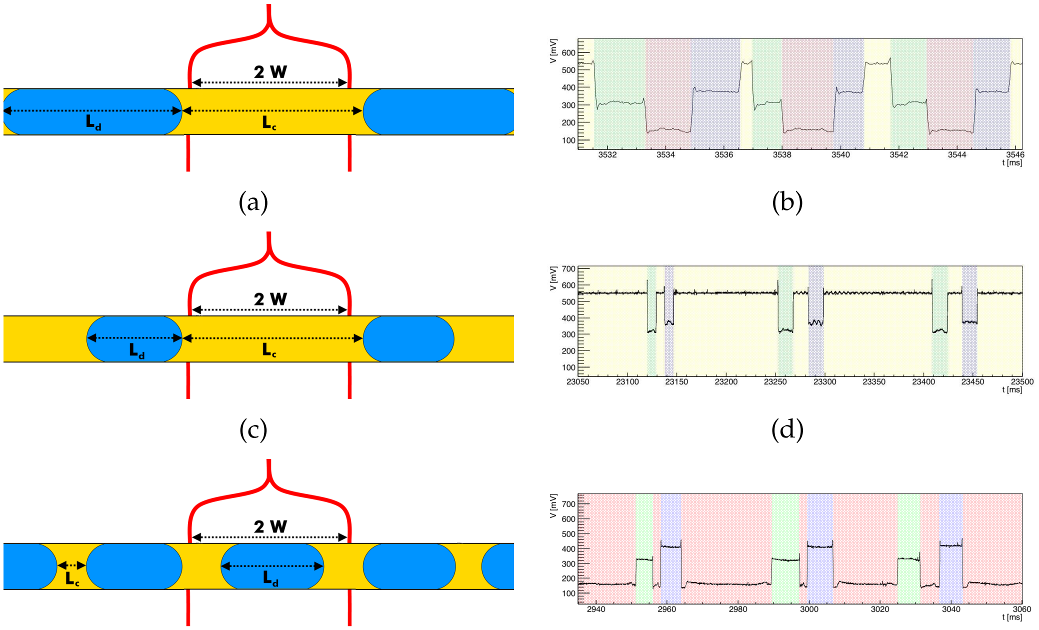

(a) (b)

(c) (d)

(e) (f)

Figure 4.14. On the left there are sketches of three different regimes in terms of signal behavior, depending of the relative droplet length compare to the arms distance. On the right the three graph reports the signals in each different regime respectively. The yellow highlighted plateaus represent the situation, where both arms have oil inside the channel, the red one when a droplet covers both arms, the green and blue when only one of the two is covered by a droplet. The signals are obtained by a test device with $2W = 260\,\mu\mathrm{m}$ *and exploiting air droplets in oil.*

The differences between the three regimes depend on the ratio $R = \frac{L_d}{2W}$ of the droplet length, $2W$ and the distance between two consecutive droplets. In fact, two consecutive droplets can exhibit different chronological sequence of the aforementioned triggering times, as shown in figure 4.14, and the regimes are characterized by different times and plateaus heights (depending on the the difference of index of refraction between two phases) sequences as follows:

(a) if $R > 1$ and continuous phase length L_c (i.e the distance between two consecutive droplets) are higher than the distance between two arms $2W$, the chronological sequence should be t_{11}, t_{12}, t_{21} and t_{22}, and this order is presented again for each droplet, see figure 4.14 (a,b). This chronological sequence implies also a specific sequence in terms of plateaus heights: both arms without droplets interaction correspond highest plateau (yellow region in figure 4.14), only one arm interacting with droplet corresponds to a half intensity plateau compared to the latter (blue or green region in in figure 4.14, depending on the arms transmission), and both arms interacting with droplet correspond to lowest plateau (red region in figure 4.14). The combination of this two sequences makes the signal a univocal fingerprints of the situation inside the channel.

(b) if $R < 1$ and continuous phase length L_c is higher than the distance between two arms $2W$, the chronological sequence should be t_{11}, t_{21}, t_{11} and t_{22}, and this order is presented again for each droplet, see figure 4.14 (c,d).This chronological sequence implies the following plateaus sequence: both arms without droplets interaction correspond highest plateau (yellow region in figure 4.14), only one arm interacting with droplet corresponds to a half intensity plateau compared to the latter (blue or green region in in figure 4.14, depending on the arms transmission). On the contrary, this regime needs an external information to correlate the actual droplets sequence to the signals, there is not a univocal droplets sequence that corresponds to the signal. However, the once matched the signal with a droplets sequence all the information about the droplets can still be obtained by the signal.

(c) if $R < 1$ and continuous phase length L_c is higher than the distance between two arms $2W$, the chronological sequence should be t_{11}, t_{21}, t_{11} and t_{22}, but t_{11} of one droplet is anticipated respect to t_{22} of the previous one, see figure 4.14 (e,f).This chronological sequence implies a similar plateaus sequence to the previous regime, expect for the situation where both arms interacting with droplet correspond lowest plateau (red region in figure 4.14). The consequence is the same of the latter regime.

As aforementioned, the only regime with a univocal matching between the droplets inside the channel and a signal is the with $R > 1$, which allows for the measurements of velocities and lengths of droplets, and to know exactly the droplets sequence inside the channel. On the contrary, two regime with $R < 1$ still guarantee the measurement procedure, but cannot provide aunivocal interpretation of the droplet sequence inside the channel. For this reason, $2W$ should be always lower than the droplets length, in order to implement this interesting feature, which make the MZI device unique and completely analogous to any imaging system.

4.3.1 Final geometrical design of the device

The distance between two arms of MZI design was chosen as $2W = 40\,\mu\mathrm{m}$, which allowed for avoiding any cross-talk, and for fulfilling the regime requirements for a unique correspondence, this means for droplets with a length $L > 40\,\mu\mathrm{m}(= 0.2w_c)$. The other parameters were chosen in order to reduce to the minimum the optical losses. The design of the tapered region, the Y-junction and the S-shaped arms were done fixing the value of $2W$ and tuning the other geometrical parameter in order to achieve maximum optical transmission, following the well-known optimization studies in literature [155–158].

In [157] the authors gave an analytical description of power and mode splitting Y divider. In particular, for small angles the Y-junction works as a power splitter, the best solution for this application. An angle of $0.5°$ guarantees a power splitting mode and at the same time it is also achievable by standard photolitographic techniques.

Secondly, the tapered region before the Y branch is designed following [155], where the authors made calculations based on the following superposition integral:

$$T_{00} = \left| \int_{-\infty}^{+\infty} \phi_{in}(x)\phi_{out}^{*}(x)dx \right|^{2} \tag{4.5}$$

where ϕ_{in} are the modes coming in the tapered region and $\phi_{out}(x)$ are the modes coming out from it. They obtained that the integral depends only on the index of refraction of waveguide core and the outer part, and the widths of the start and the end of the tapered region respectively. The designed angle was $2.8°$, it allows for achieving a loss lower than $-0.5\,\mathrm{dB}$ and at the same time for realizing a smooth transition, which is simple to reproduce with photolitography.

Finally, in [156] several low losses solutions were proposed for the four S-shaped sections, which divides the waveguides from the Y-branch to distance of parallel distance $2W$. The optimal solution for a $W < 0.1\,\mathrm{mm}$, found by the Baets [156] was a the connections between two arcs, which have losses lower than $-0.5\,\mathrm{dB}$. The two curvature radii for the arcs were given by Baets as:

$$R = \pm\frac{L^2}{4W}\left(1+\frac{W^2}{L^2}\right) \tag{4.6}$$

$2W$ was fixed by the application constraints, the values of L and R was chosen $1\,\mathrm{mm}$ and $12.5\,\mathrm{mm}$ respectively, in order to obtain a maxixum inclination angle for the waveguides $0.5°$. The final design had a length of $9.6\,\mathrm{mm}$: two tapered regions of $300\,\mu\mathrm{m}$, two S-shaped connections of $1\,\mathrm{mm}$ and the straight arms section is $8\,\mathrm{mm}$, to allow the alignment.

The fabrication of such waveguide geometry was realized with the same technique described in the previous chapter (i.e. photolitography, lift-off and Ti-indiffusion). The complexity of this geometry compared to the straight waveguide requires a deep verification of the final reproduction results, because the fine structures play an important role in terms of transmission and behavior. Among the others, the quality of Y-branches is a key factor, which was monitored during each steps, and characterized in figure 4.15, where pictures taken with optical

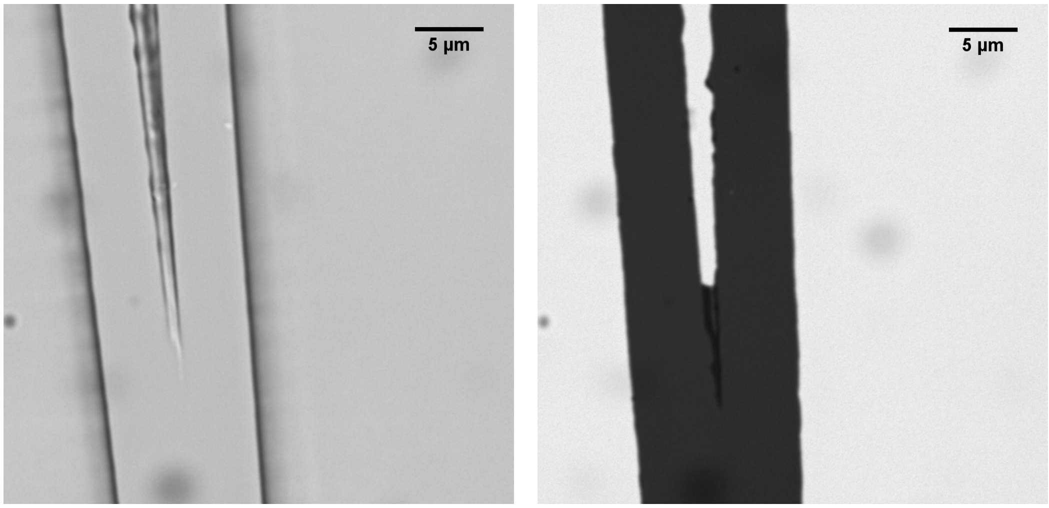

(a) After photolitography and before Ti deposition (b) after the Ti lift-of and before the diffusion

Figure 4.15. Pictures of the edge at the Y-junction of the MZI, before Ti-depostion on the left and after Ti indiffusion on the right. Both were taken by optical microscopy Eclipse Ti-E, Nikon with 40x apochromatic objective.

microscope are reported. From the picture on the left, the edges on the right and left are clearly defined and sharp, thus demonstrating high precision on the reproduction of the tapered region and the waveguide in general. Although the nominal resolution of the photoresist series is $0.48\,\mu\mathrm{m}$, the section in-between two waveguides the edge has a defined shape without the sharpness of the other edges. On the left, after the Ti sputtering the effect of this lack of sharpness is clear, during the lift off process the detachment of residual titanium layer was not so well defined. Such a behavior of the edge was well-known since 80's, and in particular Sasaki in [158] studied the losses due to lack of sharpness in the junction region.

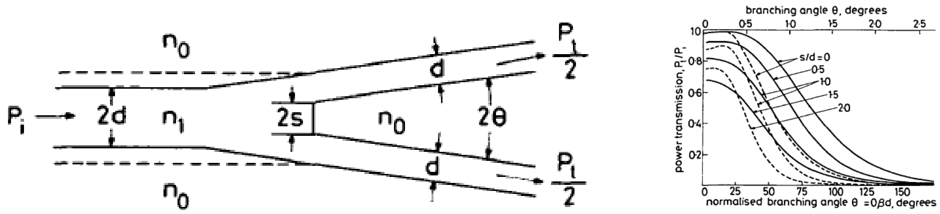

(a) (b)

Figure 4.16. On the left, there is the sketch of the junction considered by Sasaki, and on the right the power transmission calculated for different parameter. Both image were taken from orignal work of Sasaki [158].

The distance s (see figure 4.16), is measured by means of Atomic force microscope (Veeco CP-II, Camarillo, CA, USA) measurements. This morphology profile allows for the study of the thickness and sharpness of Ti stripes. s results to be close to $0.5\,\mu\mathrm{m}$ (figure 4.17). Such a value is compatible with the photoresist resolution, and the power losses, in this case, results to be less than $10\,\%$, since $\theta = 0.5°$, $d = 6\,\mu\mathrm{m}$.

4.3.2 Droplet velocity analysis results

Finally, the configuration of MZI described in the previous paragraph allowed for transmission measurements across the channels, and the same near field setup of the previous section can be used to couple light. A complete analysis of the transmission modes according to the polarization is reported in our previous work [159]. A crucial parameter is the actual $2W$ inside the microchannel between the two modes propagated in the two arms. The procedure used to measure $2W$ was the imaging the two modes inside the channel with the near field setup (section 3.2). The collection objective in the setup has a working distance of $0.8\,\mathrm{cm}$, which

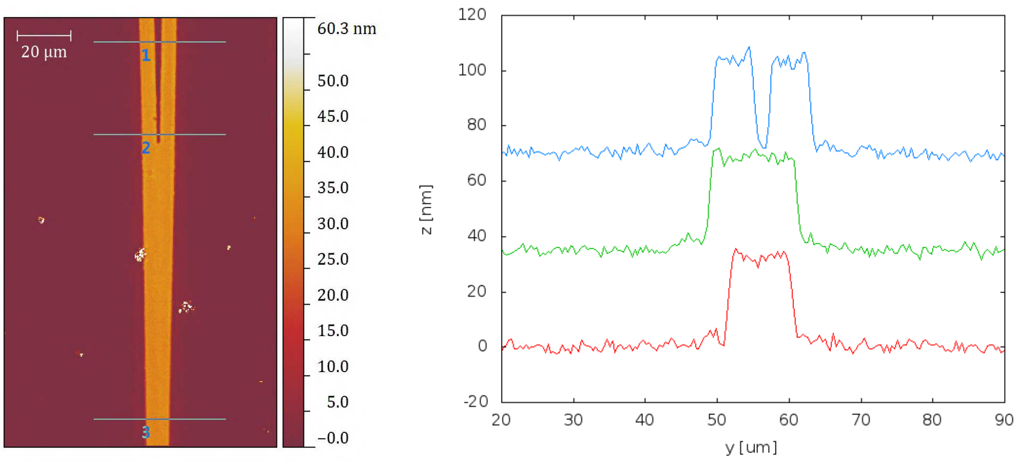

(a) (b)

Figure 4.17. Example of the AFM analysis result for MZI's Y-junction and Tapered section before diffusion of titanium. White semi spherical object in pictures are residual dust on surface of the sample. Profile on the right refers to corresponding profile studied in the figure on the left. For a better representation profile 2 and 3 have been shifted long ordinate by 35 and 70 nm, *respectively. Axis labels are referred to the crystal ones.*

is higher than the distance between the channel and the side of the sample, thus allowing the focus on the channel surface. In figure 4.18 a typical example of the CCD images of the channel side are reported.

(a) air

(b) water

(c) hexadecane

Figure 4.18. Three image of the channel view: on the top with air inside the channel, in the middle with water, on the bottom with hexadecane inside the channel. in terms of intensity there is basically no difference, since both three were taken with an OD of 3.3 *to avoid the saturation of the CCD.*

The three images in figure 4.18 differ in terms of liquid inside the channel the first had air, the second water, and the third hexadecane. No differences in terms of overall intensity can be appreciated, since all of them were taken with a optical density of 3.3. However, the mutual intensity between the two arms seems to changes accordingly to the liquids inside the channel, this effect can be explained either due to the liquid different refraction on the light collected by the objective (i.e the light have to cross the channel before meet the objective), either by a non orthogonality of the channel respect to the waveguides or simply by a coupling effects. Nevertheless, more investigation needs to be sure on this effect, studying only half on the device without the channel in order to characterize better the Y behavior. While, the similarity of overall intensity between the three confirms the fact that the images taken were really at the side of the channel and not afterwards. Indeed, the transmission intensity across the channel changes drastically by varying the refractive index inside the channel. From all the images $2W$ can be estimated from centroid of the beams profiles gaussian interpolation, on average $2W$ was $42\,\mu\mathrm{m}$ and the experimental error on this distance will be consider in terms of the distribution of the velocity measured. Indeed, the uncertainty on the measurement of the velocity is also related to the fact that the source and collector of light (i.e. the two waveguides across the channel) are not a point but an extended object.
The measurements of the droplet velocity were performed, generating droplets in a T-junction configuration using Hexadecane as continuous phase and MilliQ® as dispersed phase, in the exact way reported in section 2.2.1. The produced droplets were in a regime from squeezing to dripping, with a length from $L/w_c = 0.9 \rightarrow 202\,\mu\mathrm{m}$ to $L/w_c = 5.9 \rightarrow 1255\,\mu\mathrm{m}$. So, in every tested cases the device worked always in the first regimes of acquisition, an example of a standard signal is reported in figure 4.19.

The four trigger times t_{11}, t_{12}, t_{21}, t_{22} are considered in correspondence of the peaks before and after the rises and drops of the signal respectively. The indicator of the time is in this chase chose as the peak, because it guarantees the higher reproducibility. In fact, the MZI signal did not provide the same stability of the signal of previous section. However, this is still a preliminary study and a proof of concept of the system, the future perspective and effort could improve the system ì, thus reaching the same sensitivity of the previous section device. Moreover, the increased complexity of signal is compensed by the simpler and faster analysis of this indicator respect to the previous one. Moreover, the velocity estimation

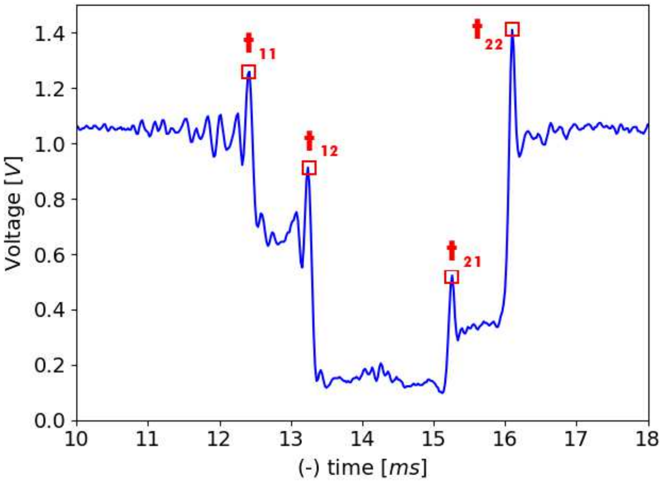

Figure 4.19. Example of the signal from a droplet generated with flow rates of $Q_c = 110\,\mu\mathrm{L\,min^{-1}}$ *and* $Q_d = 10\,\mu\mathrm{L\,min^{-1}}$*. As expected, there are two drops and then two rises, the regime is the first one and so* t_{11} *corresponds to the first drop of the signal,* t_{12} *to the second,* t_{21} *to the first rise and* t_{22} *to the second.*

need an indicator, which is always related to the same position on the droplets, in order to trigger the droplet in the same position. The only indicator that provide this feature is the peak, respect the previous ones, since it is reproducible over all four times. Indeed, these peaks are due to the lens effect of the droplet meniscus, so they are associated to the time when the waveguide light interacts with a specific point of the curved interface between continuous and dispersed phase. The choice is motivated by the fact that these peaks have high reproducibility over all droplets signal tested, and they are also really easy to be analyzed in a fast and reliable way.

In figure 4.20 the peaks related to t_{22} are reported for different droplet lengths and velocities. This graph shows the stability of the maximum compared to the oil plateau, and also that the width is proportional to the droplet length. The uncertainty on the determination of this points depends on the ratio between the width and the acquisition frequency. It could be maintained constant just by changing accordingly the acquisition frequency, but the higher is the acquisition frequency, the lower becomes the droplet analyzed, maintaining the same amount of total points in one signal. For this reason, the acquisition frequency was chosen at $50\,\mathrm{kHz}$, which allows for analyzing over 300 droplets with a reasonable amount of points ($< 10^7$) and also to describe such peaks with at least $10\,\mathrm{points}$. Then, the uncertainty was estimated as the error on the centroid from the gaussian fit. The estimated value varies from a maximum of $2 \times 10^{-6}\,\mathrm{ms}$ (for

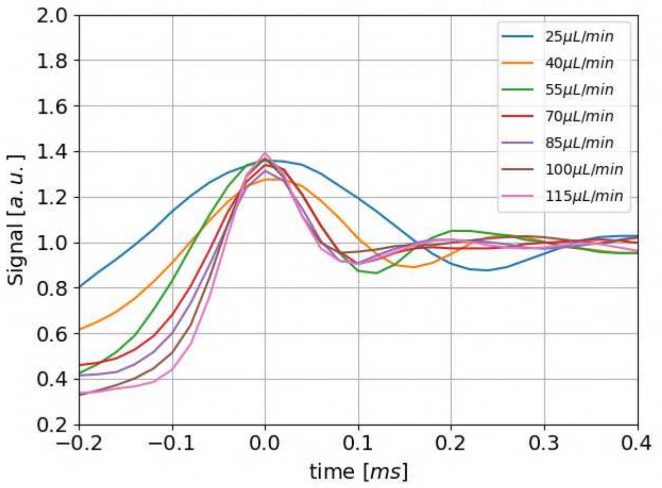

Figure 4.20. Examples of peaks related to t_{22} for different value of Q_c (in the legend) and fixed Q_d = $10\,\mu\mathrm{L\,min^{-1}}$. Higher is the Q_c, longer is the droplet, and wider is the peak.

the longest droplet) to a minimum of $9 \times 10^{-7}\,\mathrm{ms}$. Such uncertainties were considered as a systematic error, which was added to the error from the times data dispersion distribution of the times.

Once determined the four trigger times distributions, the velocity can be obtained. In particular, both velocities of first meniscus and the second can be measured with this device as follows:

$$\begin{aligned} v_{front} &= \frac{t_{12} - t_{11}}{2W} \\ v_{rear} &= \frac{t_{21} - t_{22}}{2W} \end{aligned} \tag{4.7}$$

This feature is interesting, since for some applications it could be useful to measure each one independently, especially because the two measurements are uncorrelated. The estimation of droplet velocities was made by the average of the two v. Similarly, two lengths estimation can be done through the value of the velocities, as follows:

$$\begin{aligned} L_1 &= \frac{t_{21} - t_{11}}{v} \\ L_2 &= \frac{t_{22} - t_{12}}{v} \end{aligned} \tag{4.8}$$

Indeed, the droplet length can be estimated as the time needed by the droplet to pass in front of one of the two arms divided by the velocity. Thanks to these four triggers times both velocities and lengths can be measured, an example for

300 droplets distribution generated at $Q_c = 20\,\mu\mathrm{L}\,\mathrm{min}^{-1}$ and $Q_d = 20\,\mu\mathrm{L}\,\mathrm{min}^{-1}$ is reported in figure 4.21.

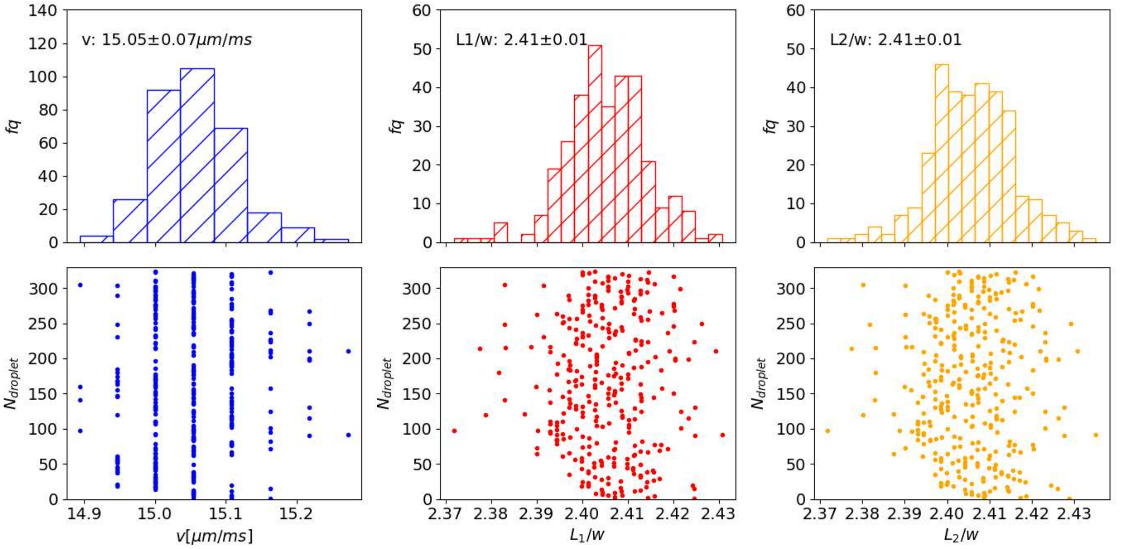

Figure 4.21. Output of the analysis made by the elaboration the voltage signal of 300 droplets. In blue on the left there is the histogram of the velocity, such 'digital' dispersion of points in graph below is due to the acquisition frequency (in this case $50\,\mathrm{kHz}$*) discretization from the DAC. Red and yellow histograms refers to the two lengths respectively. The values reported on the top of the graphs represent the averages and standard deviations.*

These analysis were done for several droplets generated at different velocity in order to demonstrate the sensibility and the working principle of the device. In particular, two different measurements were performed: in the first one Q_d was fixed at $10\,\mu\mathrm{L}\,\mathrm{min}^{-1}$ and Q_c was changed to achieve both dripping and squeezing generation of droplets (left figure 4.22), in the second $\phi = \frac{Q_d}{Q_c}$ was fixed at 1 and both flows were varied up to $55\,\mu\mathrm{L}\,\mathrm{min}^{-1}$ (right figure 4.22). The results are reported in figure 4.22, where the comparison between MZI configuration (v_{MZI}) and the standard camera setup (v_{Video}) is reported. In particular, the setup used as a comparison is the one described in 2.2.2.

Both graphs show a clear overlapping between the two systems, thus demonstrating the accuracy and the independence from the droplet properties of MZI measurements over a wide range of droplets, for both faster (ϕ=1 figure on the right 4.22) and longer droplets (Q_d =$10\,\mu\mathrm{L}\,\mathrm{min}^{-1}$ figure on the right 4.22). The significant results is remarkable, since the same measurements of a standard setup can be exploited with a portable and integrated device. This device represents a huge improvement respect to the one presented in section 4.2, since it requires

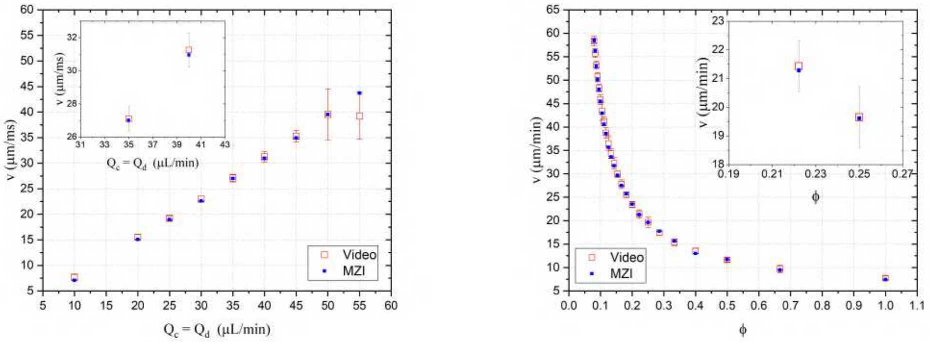

(a) Q_d =10 µL min^{-1}

(b) $\phi = 1$

Figure 4.22. The graphs represent the trend of velocities over ϕ, on the left, and over Q_c, on the right. The blue points are the results for the MZI device analysis while the red one for the video. The insets show better the difference in terms errors of the two systems.

only the measurements of the distance between arms as a calibrations step, which can be done only once for every device. Moreover, this data confirms that the MZI does not distrub in any way the droplet generation on the device, and there is no cross-talking between this two stages, thus evidencing a perfect integration on the same substrate. Consequently, the independence from the droplet generation and properties on the velocity measurements is the validation of the proof of concept, which can be extended to any other flowing objects, as long as their length is smaller than $2W$ and they interacts with the light from the two arms.
A deeper investigation on the comparison of the performance between MZI device and standard video setup is presented in the following figures 4.23. The accuracy of MZI measurements respect to the Video was estimated by compatibility of the slope with 0 and intercept with 0 of the linear interpolation between v_{MZI} and v_{Video} (see top graphs in figure 4.23). In both case slopes and intercepts were compatible with 1 and 0 respectively (slope 1.001 ± 0.005 and intercept 0.1 ± 0.1 for Q_d =10 µL min^{-1} and slope 0.993 ± 0.007 and intercept 0.5 ± 0.2 for $\phi = 1$), moreover in both cases R^2 was higher than 0.9998.

The precision comparison between the two systems is reported in figure 4.23 on the bottom, where the standard deviation is reported in terms of percentage of the distribution of more than 300 droplets for each combination of flows tested. The plots of both situations (Q_d =10 µL min^{-1} and $\phi = 1$) show a drastical increase in the precision by the MZI respect to the Video analysis. In particular, the values for the MZI are always less than $1\,\%$, which is less than the lowest value for the

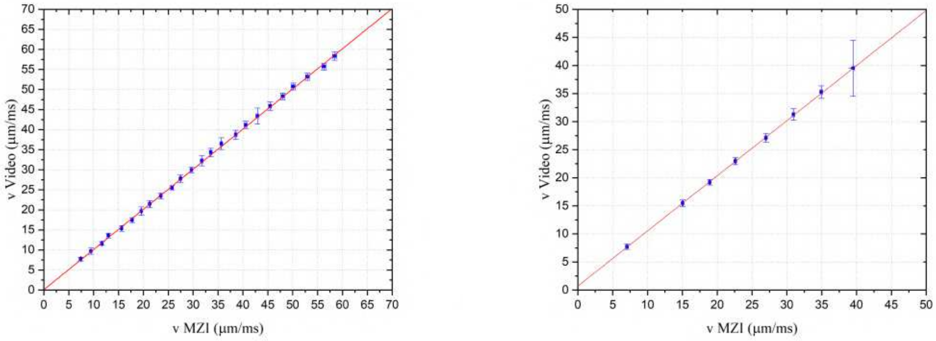

(a) $Q_d = 10\,\mu\mathrm{L\,min}^{-1}$ (b) $\phi = 1$

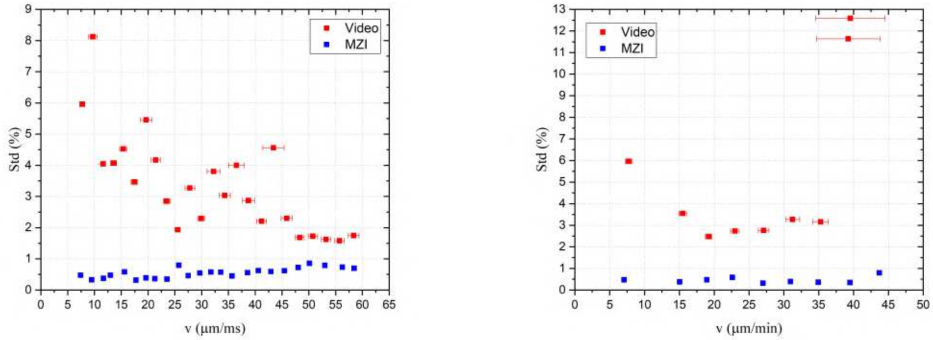

(c) $Q_d = 10\,\mu\mathrm{L\,min}^{-1}$ (d) $\phi = 1$

Figure 4.23. The graphs represent precision and accuracy analysis made for both data sets, on the left $Q_d = 10\,\mu\mathrm{L\,min}^{-1}$ *and* $\phi = 1$ *on the right. The graphs on the top are the linear behaviors of* v_{Video} *against* v_{MZI}*, in order to test the accuracy. The graphs on the bottom report the standard deviations in percentage of the* v_{Video}*, in red and of the* v_{MZI}*, in blue, for a distribution of* 300 *droplets.*

video analysis. Furthermore, the precision of video analysis strongly depends on the Q_c, while the one from the MZI is independent of it and with an average error of $0.5\,\%$.

In conclusion, the $LiNbO_3$ MZI velocimeter device was demonstated to be a reliable integrated tools for the velocities measurements of flowing object inside a microchannel. As matter of fact, its performances were proven to be three times higher than the one of a standard video camera microscope setup, in terms of precision. Beyond these remarkable results, the integrability and portability of the presented platform is not even comparable with a bulky instruments of standard system, such as a camera and a microscope. Despite the new technological improvements in terms of the sizes of video camera, the prices increase exponentially with the sizes and the acquisitions speed, while speed is not a limiting factor by MZI system. The optical signal, indeed, can be either read analogically without any speed limitation, or converted by an Analog to Digital converter, which can easily reach hundreds of kHz for cheap prices. Finally, the signal from the MZI can be simply analyzed during the measurement or efficiently store, while the video storage and analysis are typically slow, unefficient and require post processing.

4.4 Optofluidic device for pH titration

One interesting properties that can be analyzed by the optical transmission signal is the absorbance of the liquid inside the microchannel. The standard law used for the description of absorbance spectroscopic analysis is:

$$T = \frac{I_T}{I_S} = e^{-k_\lambda L} \tag{4.9}$$

where I_T is the transmitted intensity across a medium of length L and attenuation coefficient k_λ, I_S is the incident intensity on the medium and T is the transmittivity. From the equation 4.9, the exponential dependence of optical path L decreases drastically the contrast of transmission measurements between two different media, thus making such an analysis inconsistent for microfluidics, where most of the distances are in the order of hunderds of micrometers. However, in some specific applications the absorbance of liquid medium has sharp transition in correspondence with change of one property. This is the case of pH titration where the absorbance changes drastically respect to the pH of the solution, in particular at the so called titration point. Despite the small optical path guaranteed by microfluidic environment, in such a sharp transition this optofluidic device could be precise enough for pH precise determination by means of the optical transmission analysis.

The pH titration is a standard chemical quantitative analysis used for the determination of pH solutions. This measurements is based on the capability of pH indicator molecules to change their optical response (i.e. the transmission spectra) depending on the pH of the medium where these molecules are dissolved. There are several pH indicator available, and they are distinguished by their endpoint, which refers to the pH point at which the indicator changes color in a colorimetric titration. This technique is the most convenient for the determination of the equivalence point of the mixture of an acid-base systems, in order to neutralize the starting acidic or basic solution, depending on the needs. A standard neutralization is typically done adding to the starting acid or basic solution a small quantity of complementary one, and simultaneously checking the color (or equivalently the absorbance) of the analyte to identify the endpoints of pH indicator. In this case the endpoint of the pH indicator is equivalent to the equivalence points of the system. An example of standard pH neutralization is reported in the figure 4.24, where an aqueous solution of NaOH is neutralized by HCl one exploiting Blue Bromothymol pH indicator, which changes its color from blue (basic) to yellow (acid) passing through green during the interval pH 6-7.6 around the endpoint, thus when the solution has the green color the solution is neutralized.

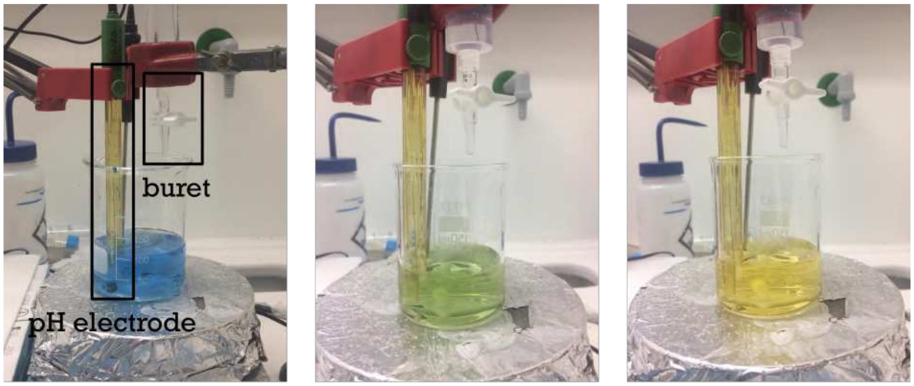

basic solution
color blue
ph> 7

neutral solution
color green
ph=[6.6,7]

acid solution
color yellow
ph<6.6

Figure 4.24. Setup for standard titration: the buret allows for the addition of small volumes into the liquid in the beaker, where the pH is also measured by the pH electrode as a reference. The starting liquid with the pH indicator is stirred by means of the magnetic bar.

It is clear how the pH of the solution is related to its optical absorbance thanks to pH indicator molecule. In particular, its absorbance spectrum drastically changes during the transition across the endpoint, thus allowing for also precise pH determinations near this pH point. This chemical analysis is perfectly suited for the device described in the previous chapter, where the waveguide is an optical transmission probe for the microchannel liquid. The $100\,\mu\mathrm{m}$ optical path of the channel is large enough, to perform such an analysis thank to the sharp transition of the pH indicator.

In this framework, the lithium niobate optofluidic device has all the properties and tools needed to perform such a chemical analysis in an integrated device: the chemical resistance that no other optofluidic material plaftorm can provides, and also the proper optical transmission probe. It can be exploited for effective neutralization operation in microfluidic channel, offering low reagents consumptions and high portability. Moreover, using different pH indicators with different endpoints the pH of a solution inside a microchannel can be measured effectively in a large range. These kind of lab-on-a-chip could be a breakthrough, since the standard pH performed slow measurements with the needs of large volumes of solutions (several mL), while such an optofluidic device has fast response in microfluidic environment of few nanoliters.

The physical principle was that to record the transmitted light across the microfluidic channel filled with the analyte. The light is illuminating the fluid by a suitable integrated optical waveguide as already described in the previous sections. The advantages of $LiNbO_3$ platform not only relies on its performance but also on the excellent chemical resistance to the chemical etching of $LiNbO_3$. This material is almost inert to strong acidic and basic solutions allowing the widest range of applications of pH values involved in titration.

4.4.1 Opto-microfludic pH titration

The device should integrated in the same substrate an equivalent system to the bulk one. Firstly the two liquids with opposite pH values should be added in a controllable way inside the microchannel. Each one is pumped by an OB1 MK3 pressure driver pump and the flow control is obtained by a feedback system provided by the coupling of three flowmeters BFS Coriolis[5] (Bronkhorst, AK Ruurlo, Holland), as showed in figure 4.25. The two flows ratio between the two is related to the concentration of the mixture, which is injected inside the optofluidic device. Depending on the pH of the solutions, the pH indicator will change the mixture transmission spectra. In this way the optical waveguide acts as a probe to the real pH of the solution, and so the flow ratio can be adjusted as a consequence, in a rapid optofluidic feedback system which avoid any extra consumption.

The system were tested using Blue Bromothymol[6] as pH indicator, which presents a nominal endpoint inbetween pH of 6 an 7.6, it have a color change from blue (basic) to yellow (acid), as showed in figure 4.24. The liquids injected were

---

[5] accuracy: $0.2\,\%$, response time: $35\,\mathrm{ms}$

[6] CAS Number: 34722-90-2 Empirical Formula (Hill Notation) $C_{27}H_{27}Br_2NaO_5S$

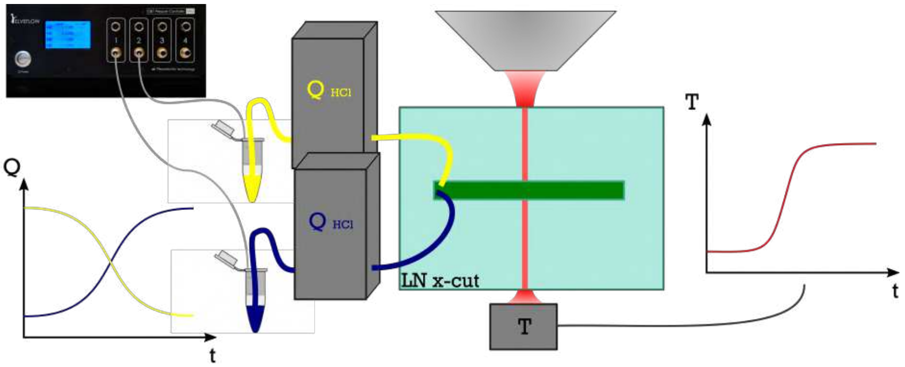

Figure 4.25. Opto-microfluidic setup for the titration: the injection of the two fluids is provided by the Elveflow pumps system with two flowmeters, whereas the the optical system is the standard near field previously described. The light intensity is measured with a silicon photodiode. The pH is controlled by a feedback system: the ratio between the flows changes the composition of the mixture inside the channel, and the waveguide is measuring constantly the transmission, therefore the pH of the solution.

aqueous solution of NaOH and HCl respectively, the same concentration of pH indicator was added to both solution. The concentration was optimally chosen in order to achieve the highest absorbance possible, avoiding saturation phenomena. Indeed, if the concentration of pH indicator exceeds the limit of solubility, it changes the pH of the solution introducing artifacts in the final measure. The optimal concentration was calibrated for our system by means of a spectral analysis using V-670 UV-VIS-NIR Spectrophotometer (Jasco Europe, Italy). Twelve solutions of aqueous solution of HCl and NaOH with different concentration of Blue Bromothymol were prepared and their visible spectra are reported in figure 4.26. Firstly, the spectra suggest that the highest transmission contrast between two solution can be achieved in the red range wavelength. For this reason, the wavelength used for this experiment was $632.8\,\mathrm{nm}$, but any wavelengths can be used in principle and even multiple waveguide at the same time. Secondly, the graph on the right is the transmission data at $632.8\,\mathrm{nm}$, which show an exponential behavior as evidenced by the interpolation. The tail of the exponential represents the saturation region in terms of absorbance, the addition of other pH indicator doesn't increase the absorbance. At the same time, the saturation in terms of pH artifact of each solution was tested with a pH meter, and each one does not show pH changes. The optimal value for the pH indicator concentration choose was the last one of the exponential, which was $0.12\,\mu\mathrm{M}$. Indeed, this value allows for achieving the maximum in terms of absorbance without affect the pH value of the solutions.

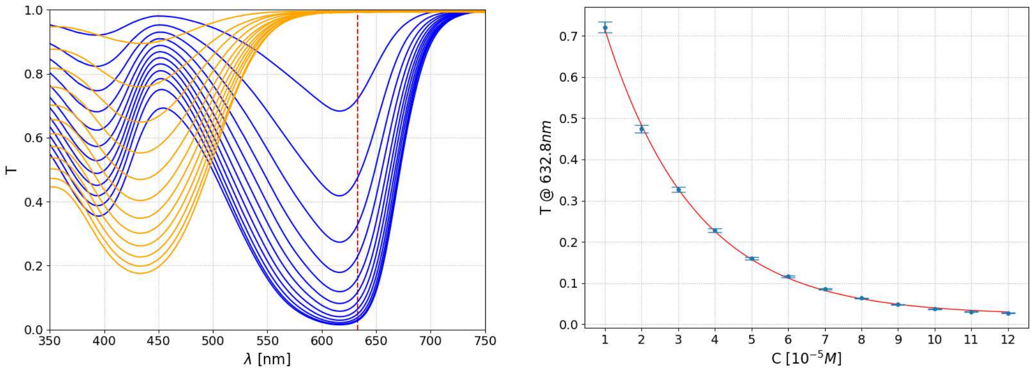

(a) Visible Spectra (b) T $632.8\,\mathrm{nm}$

Figure 4.26. Concentration analysis of the Blue Bromothymol: on the left there are the transmission spectra in the visible, the blue spectra are the one for the NaOH aqueous basic solution, whereas the orange one are the acid HCl aqueous. On the right, the transmission at $632.8\,\mathrm{nm}$ *(the red line in the visible spectra) are plotted in function of pH indicator concentration.*

Before the actual measurements in the device, a calibration of the pH indicator was performed in order to study what to expect by the device results. In particular, the standard bulky titration was performed and at several fixed pH value of the solution a spectral analysis was done. In the figure 4.27 an example of these spectra is reported on the left, whereas on the right the transmission at wavelength of $632.8\,\mathrm{nm}$ during the transition.

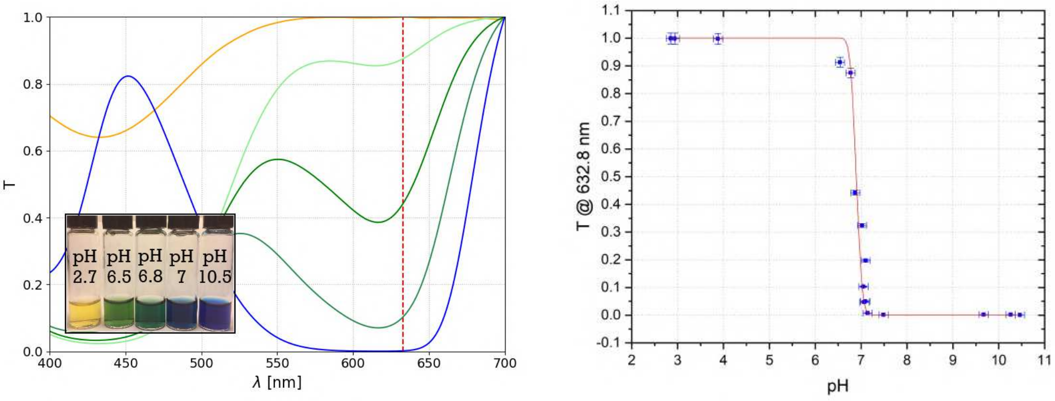

(a) (b)

Figure 4.27. Titration analysis for Blue Bromothymol: on the left 5 different pH solution spectra are reported across the endpoint, (a solutions picture is in the inset). On the right the data of the transmissions at $632.8\,\mathrm{nm}$ *are plotted in function of pH.*

The transition shows an abrupt change of transmitted intensity in a really limited interval of the pH. The characterization of this transition was realized by the fit with an error function of the data in figure 4.27. The steep transition from $T = 1$ to $T = 0$ occurred in a pH interval of 0.6 and centered in 6.89 ± 0.05. The calculations for such a transition for an optical path of $100\,\mu\mathrm{m}$ shows a transition of Δ_{sp} $=0.12 \pm 0.01$ in transmission in the interval 6.5-7.1, and thus making feasible a detection with the optofluidic platform.

This value is matching with the measurements performed with the device, as showed in figure 4.28 where our latest main results are reported. In these measurements the flows were changed 11 times every $3\,\mathrm{min}$ as following:

time	$Q_{(Startingsol.)}$ $\mu\mathrm{L\,min^{-1}}$	$Q_{(Neutralizingsol.)}$ $\mu\mathrm{L\,min^{-1}}$
0-3 min	100	0
3-6 min	70	30
6-9 min	65	35
9-12 min	60	40
12-15 min	55	45
15-18 min	50	50
18-21 min	45	55
21-24 min	40	60
24-27 min	35	65
27-30 min	30	70
30-33 min	0	100

Table 4.1. Combination of flow tested every 3 minutes the starting solution flow was decreased, while the neutralizing one was increased accordingly. The precision of the experimental is the one provided by the sensibility of the flowmeters.

The pump system allowed for a dynamic changed of the flow rates, but as a first tests the use of fixed and stable flows was better to understand the behavior of the systems. The transition between each flow rate combination was still recorded and tested as a first step to check the dynamic behavior. Moreover, the two solutions were mixed before the injection onto microfluidic channel, in order to check the right mixing of two solutions, and to prevent slow diffusion and mixing in microfluidic dimension.

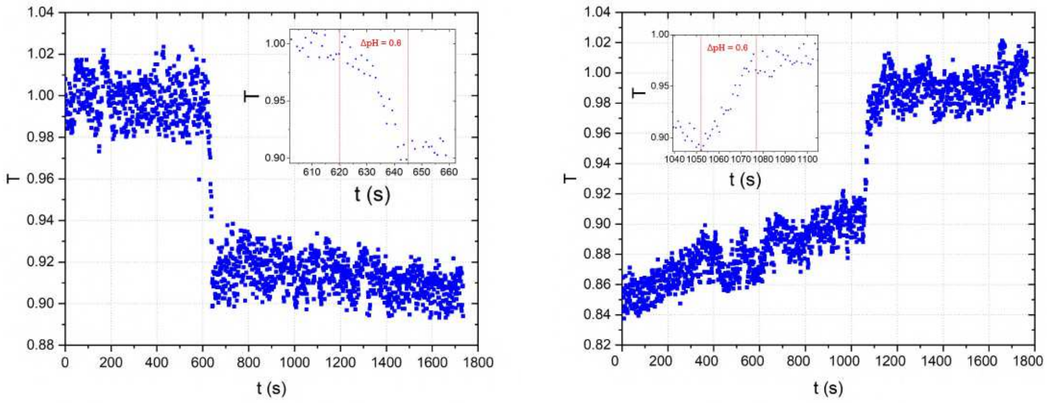

(a) (b)

Figure 4.28. The optical transmission response from the waveguide on the chip is plotted in function of time in which every $3\,\mathrm{min}$ *the ratio between the flow of two solutions was changed. The two measurements have the opposite order of flow ratios. In both insets there is an enlargement of the abrupt transition.*

The measurements show well distinguishable steep transitions between two plateaus, which correspond to the pH transition, since both measurements are completely reversible (see figure 4.28), neglecting any random noise as the source of such a transition. Both transitions were characterized by the difference between the average of 60 point after and before the transition interval respectively, and they results Δ_{HCl} $=0.09 \pm 0.01$ (basic solution as the starting solution, left figure 4.28) and Δ_{NaOH} $=0.08 \pm 0.01$ (acid solution as the starting solution, right figure 4.28). Both values are compatible with the predicted one.

These latest results clearly show how the neutralization point can be easily found with this opto-microfluidic device: the flow rates can be tuned accordingly in a feedback system with the transmission optical signal from the waveguide. Moreover, the detection precision on the intensity during the transition could be a reliable measurements of the pH. It indeed shows a precision For instance, in the case of figure 4.28 the device could measure the pH in the interval 6.5,7.1 from the optical transmission response. The pH indicators and the wavelengths can be tuned opportunely in order to measure also in higher pH ranges, even high or low pH taking advantage of the chemical resistance of $LiNbO_3$. This proof of concept opens the way to many applications in the chemical analyses and work is in progress to study further potentialities and opportunities provided by our platform. A further improvement will be performed by optimizing the measures protocol: the possibility of using an alternate sequence of droplet A-B-A-B-... (A=analyte solution, B=solution without the pH indicator) will allow to update the transmission measures with the background subtraction.

4.5 Optofluidic multiplexer

The potentiality of combining of $LiNbO_3$ and microfluidic tools on the same platform opens to the exploitation of these devices for optical applications. An example is presented herein, whit the aim to realize an optical *multiplexer* actuated by a microfluidic system. The microfluidic channel can be used to tune the light refraction inside the channel in order to couple light in different waveguides. The sketch in figure 4.29 represents the working principle of this device. The light from a waveguide can be directed inside one desired waveguide from a pattern by means the refraction dependent on the value of tilt angle respect to channel direction. Like an optical multiplexer, the output pattern can be controlled by the tilt angle, the channels widths and the refractive index of the medium inside the channel respectively. In particular, one or multiple output waveguides of a pattern can be excited by choosing the liquid with the needed dispersion relationship inside a tilted channel with a specific width. Moreover, the waveguides pattern can be designed depending on the application, either multiplexing, switching, or filter. In general, the liquid optical properties can be tuned opportunely to modified the light propagation depending on the needs. For instance, multiple channels with different tilting angles and widths can be realized on the same sample, where the liquids with specific optical properties can be injected, in order to achieved a multiplexer. In this way, the liquid add a novel degree of freedom in the tunability of optical devices.

Herein, the first demonstration of this possibility is demonstrated by proving the feasibility on controlling the waveguide output by means of the refraction controlled by the liquid inside a tilted channel.

The device designed for this aim is based on a pattern of straight waveguides, interrupted by a microchannel in a diagonal direction respect to these latter. A channel induces a refraction of the light from the waveguide (i.e. the input waveguide), which can recoupled in other waveguide (i.e. the output waveguide) from the pattern depending on the aforementioned parameters. Therefore, the distance between the input waveguide and the output waveguide is related by refractive index of the liquid inside the channel. In particular, the distance d is related as follows to the parameter of the device referring to the figure 4.29:

$$d(L, n_L, n_{LN}, \theta) = \frac{\sin(\alpha(n_L, n_{LN}, \theta) - \theta)L}{cos(\alpha(n_L, n_{LN}, \theta))} \tag{4.10}$$

where n_L is the refractive index of the medium inside the channel, n_{LN} is the refractive index of lithium niobate seen by the light inside the waveguide (i.e. ordinary, since the waveguide are z-propagating) θ and $\alpha(n_L, n_{LN}, \theta) = \sin^{-1}(\frac{n_{LN}}{n_L}\sin\theta)$ are the angles in figure 4.29 and L is the width of the channel. Depending on the distance d, the device controlled by the liquid inside the microfluidic channel.

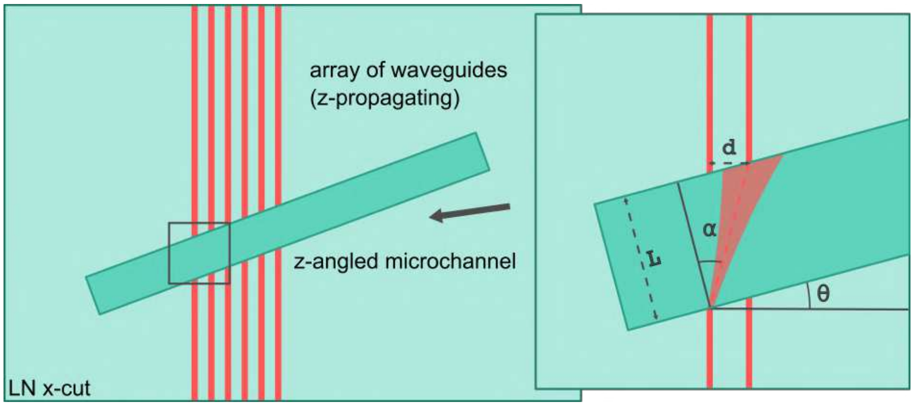

Figure 4.29. Sketch of the final design for the optofluidic device: a pattern of waveguides is coupled with a L wide microfluidic channel, which crossed them at an angle $\frac{\pi}{2} - \theta$. Such a channel induces a refraction of the light from the input waveguide at an angle α, resulting in a deviation d on the other side of the channel.

If d matches the distance between the input waveguide and a waveguide from the pattern, the light can recouple in the latter. The device can also avoid any recoupling if the n_L is small enough to have θ higher than the critical angle, thus achieving a total reflection condition. In particular, this condition is reached when $n_L > n_{LN}\sin\theta$. So, the device can be tuned the output waveguide over a pattern by tuning opportunely the waveguide pattern by means of photolitographic process, and the n_L, for instance just by adding salts in water.

4.5.1 Fabrication and coupling procedure

Although the device geometry is slightly different from the previous presented ones in this chapter, the fabrication steps were the same: firstly the Ti indiffusion waveguide patterns were realized (section 3.1), secondly tilted channels were engraved by means of self-polishing saw (section 2.1). The main issue for this application is the control of the distances between the waveguides during all the fabrications steps, since the performances of the device are strictly related to the waveguides pattern. In particular, the higher is the distance between two consecutive waveguides the greatest is the refractive index change needed to couple light from one to the other. Several patterns of waveguides were tested: the waveguides width was maintained always $5\,\mu\mathrm{m}$, while the pitch (i.e. the distance between the centers of two consecutive waveguides) was varied as follows: 10, 11, 12, 13, 14, 15, 20 and $25\,\mu\mathrm{m}$. Since its importance in term of performances, the pattern geometries were measured at each step during the fabrication process: the nominal one on the Chromium mask, after the lift off and after diffusion. Ti stripes after the lift-off were characterized by Microscope pictures (figure 4.30), in particular for each pattern the unit width was measured. The unit is considered as the minimum part, which is repeated in the pattern (see red dashed lines in figure 4.30). The widths of 1 up to 5 units were measured then the average is considered with the semidispersion as the error, the results are reported in table 4.3. Each pattern was realized twice on each sample, 24 samples were realized from 2 different wafer, in order to take into account every fluctuation possible during each fabrication step.

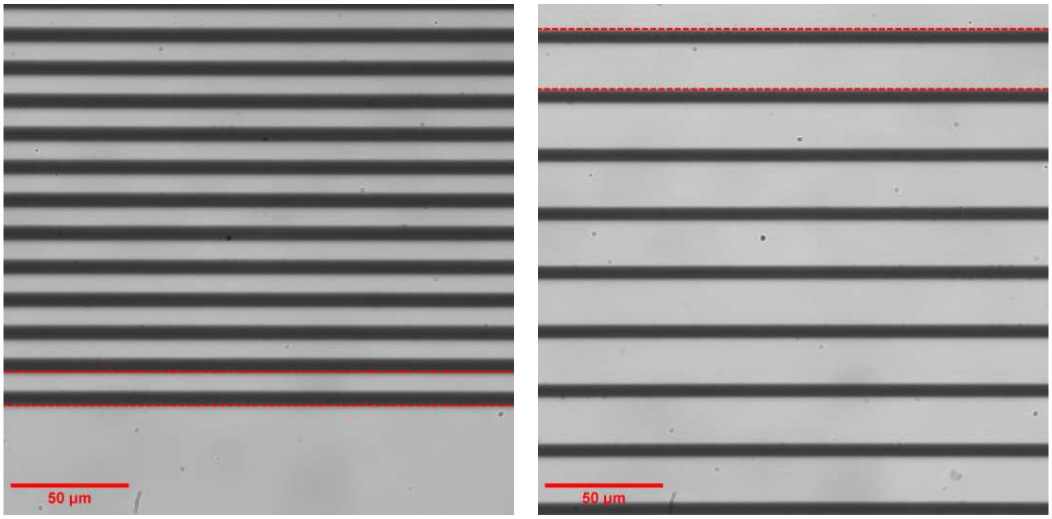

(a) (b)

Figure 4.30. Microscope picture of the Ti stripes after the lift-off process. The microscope was an inverted Nikon Ti-E equipped with 60x Objective. The red dashed lines represents the unit for the patterns, on the left the picture of a pattern with a unit of $14\,\mu\mathrm{m}$ *(nominal value) is reported, and on the right the unit has a nominal width of* $25\,\mu\mathrm{m}$.

The results are in agreement with the nominal values. The unit distance can be compared between different patterns, but the waveguides width could be change between different patterns due to the photlitography process. The widths of Ti stripes and the empty spaces between stripes were also analyzed independently from the unit of the pattern, in particular considering the position on the wafer. In fact, the Ti deposition procedure could affect the distribution especially on the high surface like on a full wafer, for instance during the spin coating and the UV exposure the developed photoresist layer can present some lack of uniformities, or during the Ti sputtering the deposition rate can change for such surface. In particular, the samples were squared shape with side of $1.7\,\mathrm{cm}$, and 12 samples can obtain from one $3\,\mathrm{inch}$ wafer distributed on a cross shape, thus 8 distributed on the side and 4 in the center of the wafer. Such a distribution requires an analysis to confirm the uniformity for all the samples. The results of the analysis for the pattern with $10\,\mu\mathrm{m}$ unit is reported in the following table: The samples on different positions presented some slight differences in both Ti stripes and empty spaces, but values are still in agreement each others considering errors from statistical analysis. The results show how the photolitographic technique tends to have larger waveguides against the space in-between them. This effect could be due to the diffraction of the UV during exposure, because this mismatching is more evident in the central sample where the diffraction of the light is higher. However, such differences are always lower than $2\,\mu\mathrm{m}$ and have a systematic and reproducible aspect, that can be predicted and corrected during the mask designing.

position and wafer	**Ti stripes** [$\mu\mathrm{m}$]	$5\,\mu\mathrm{m}$ **empty space in between** [$\mu\mathrm{m}$]
central on wafer 1	6.2 ± 0.3	4.1 ± 0.2
side on wafer 1	5.8 ± 0.3	4.4 ± 0.1
central on wafer 2	6.1 ± 0.3	4.4 ± 0.2
side on wafer 2	5.7 ± 0.3	4.6 ± 0.1

Table 4.2. Ti stripes analysis depending on the position on the wafer.

After the characterization of the Ti stripes, the diffusion was performed and the final patterns were obtained. Since the Ti stripes patterns could be modified during the diffusion process, a second analysis of the final configuration was required. For instance, some anisotropies during the thermal treatments or crystal defects could induce some differences between the Ti pattern and the actual distances between modes propagated inside the waveguides. Moreover, an optical control of the diffused waveguides represents a test for the quality of the sample. Therefore, before the engraving of the channel, the samples were analyzed by a near field setup depicted in figure 4.31.

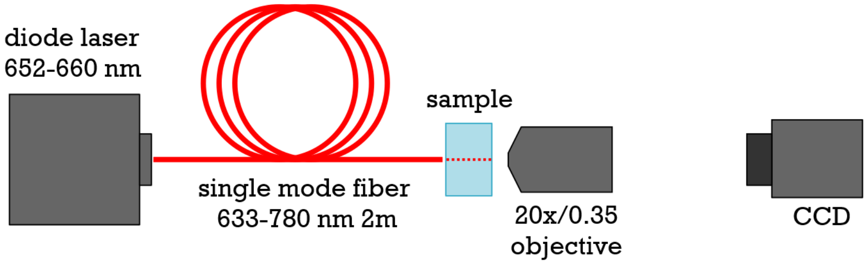

Figure 4.31. Experimental near field setup for coupling a laser diode into a waveguide. the fiber is posited onto a nanopositioner, in order to get close as much as possible to the surface of the sample. The near field output is characterized by an objective coupled to a CCD camera.

In particular, a red diode laser was coupled into several consecutive waveguides for each pattern by a mono mode fiber and the mode outputs were analyzed by a CCD (figure 4.31). Each picture was taken without moving both sample and camera, but only the fiber in order to allow for an overlapping of the images taken and so an analysis of the distances. The intensity profile of the overlapped pictures were interpolated with one gaussian functions for each waveguide, as showed in figure 4.32.

From these interpolations, the distances between the centroids were obtained, as well as the σ, which represent the waist of each input source. The average of this later over all the waveguides analyzed was $1.80 \pm 0.02\,\mu\mathrm{m}$, which confirms that a pattern with distance larger than 2σ cannot be achieved for this wavelength. The average differences between two consecutive centroids are reported in table 4.3 for each pattern. The table is an overall views for all tested pattern: from the values the diffusion seems to be the critical process, since the average distances after diffusion are smaller than before. However, this mismatch is due to the fact that the propagation mode is slightly different from the Ti concentration profile, and due to the diffusion of Ti in the direction parallel to the surface. So, this difference can be properly predicted and corrected during fabrication process. It is worth mentioning that these problems only at a laboratory level, because Ti-diffused technology in the telecom has reached an excellent compatibil-

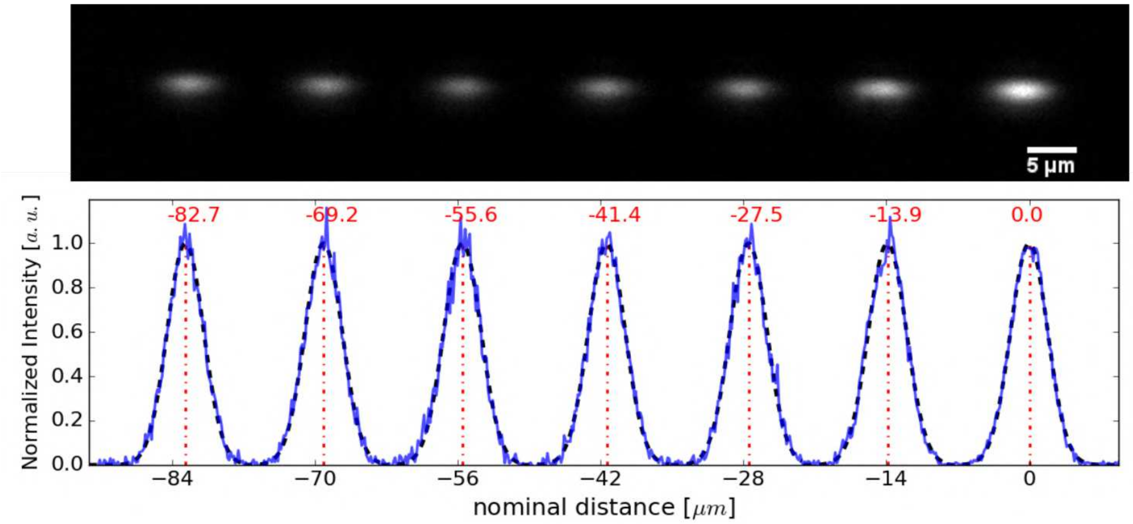

Figure 4.32. Analysis of the $15\,\mu\mathrm{m}$ *unit pattern: on the top near field pictures overlapping is reported, where each waveguide is coupled singularly and then the overlapping final image is the result of all outputs. On the bottom, the blue line is the intensity profile referring to the outputs image, where each profile is normalized in order to have an integral equal to 1 and the x-axis is shifted by the first Gaussian centroid. The red lines report the value of the Gaussian centroid, resulting from the gaussian interpolations drawn in and the black dashed line.*

ity between the nominal the design and the final diffused one. The last fabrication

Nominal unit width [µm] (on Chromium Mask)	**Ti stripes and empty space** [µm] (after Lift-off)	**distances between waveguides** [µm] (after diffusion)
10	10.0 ± 0.1	8.7 ± 0.2
11	11.0 ± 0.1	9.6 ± 0.3
12	12.0 ± 0.1	10.4 ± 0.2
13	13.0 ± 0.1	11.3 ± 0.1
14	14.0 ± 0.1	12.2 ± 0.1
15	15.0 ± 0.1	13.1 ± 0.2
20	20.0 ± 0.1	17.5 ± 0.3
25	25.0 ± 0.1	21.8 ± 0.3

Table 4.3. Overall results of the pattern geometry characterization: from the nominal value, then Ti stripes after the lift off, to final waveguides.

step required for the realization of this device was the engraving of the channel, in section 2.1 the realization of such angled channels is already discussed. Several value for θ angle were tested: $12.5°$, $13.3°$, $14.1°$, $15.5°$, $21.5°$. All the channel were engraved with the $50\,\mu\mathrm{m}$ thick blade, and in principle the L should be the same. Nevertheless, for a precise calculation of d a measurements of the channels width L are needed. For this reason, 10 profiles of the channel were obtained by a profilometer P-10 (KLA Tencor, California, USA), and for each one the widths were calculated, final geometry features of each samples are reported in the following overview table: The actual channel are $10\,\mu\mathrm{m}$ thicker than the nominal blade width, this mismatch could be either due to the vibration during the cut or to the actual thickness of the blade. Nevertheless, there are no specific needs of channel widths for this application, $50\,\mu\mathrm{m}$ was chosen in order to prevent high consumption of liquids and low dispersion. The injection of this latter were provided by pressure pumps, which flowed the desired liquid from a tank into a tube connected to the a inlet in the PDMS cover, which was previously connected to the LiNbO$_3$ substrate, as described in section 2.1. The chip showed in figure 2.5 was indeed one used for this application.

θ ($degree$)	L [µm]
12.5	61 ± 1
12.5	62 ± 2
13.3	62 ± 1
13.3	61 ± 1
14.1	62 ± 2
14.1	62 ± 2
21.5	61 ± 1

Table 4.4. Results of the analysis on the channel geometry features.

The devices were tested with water ($n_L = 1.331$ at $655\,\mathrm{nm}$) and air ($n_L = 1.0003$ at $655\,\mathrm{nm}$) as the liquid inside the channel. The setup used for the measurements was the one depicted in figure 4.31. A mono mode fiber for a wavelength of $655\,\mathrm{nm}$ was used instead of the objective as a coupler, since it guarantees a single coupling with the input waveguide of the pattern. In fact, for a spot higher than the pitch of the waveguides pattern, more than one waveguide can be excited.

The diameter mode output of such fiber was measured to be lower than $5\,\mu\mathrm{m}$, which is lower than the minimum distance between two consecutive waveguide, thus avoiding for the simultaneous coupling of the waveguides.

4.5.2 Results and comparison with the theoretical formula

The first test made on the device was the control over the effective optical transmission across the channel on the diagonal surface outputs. The proof was given by the microscope images taken from the top of the samples, thanks to the scattering light from the waveguides. These pictures, as the one reported in figure 4.33, demonstrated that the light can be recoupled on a different waveguide of the pattern from the input one across the channel. On the picture 4.33, indeed, the light from the left waveguide (i.e the input one) when it meets the channel is a refracted pattern respect to the input one.

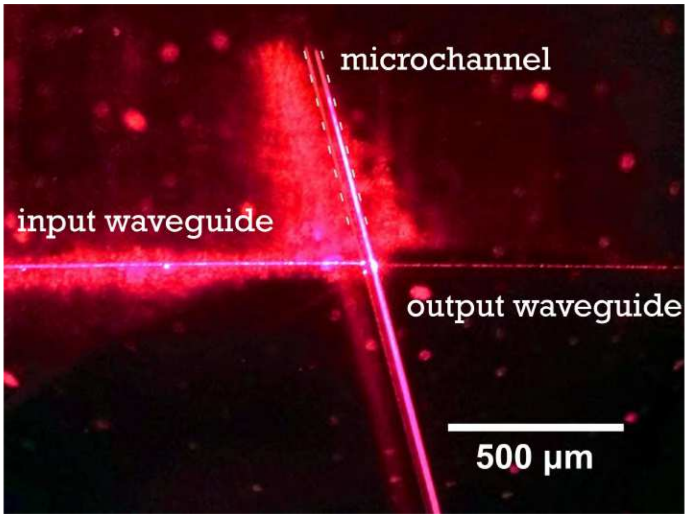

Figure 4.33. Picture from the top of a multiplexing device. The input waveguide on the left is illuminating the microchannel, which refracts the beam across the channel and it couples in the output waveguide. The output waveguide is clearly not align with the input one, thus demonstrating the working principle of the device. In particular, the three bright spots on the channel represents respectively: the point where input waveguide illuminates the channel, the spot of illumination on the other side of the channel, and the point of reflected illumination.

Before the measurements, the formula 4.10 allows the calculation of d for each sample (θ, L) and for each liquid (air, water, n_L), and so the best pattern for each application was used. For instance, the calculation for a wavelength of $655\,\mathrm{nm}$ gave $d_{air} = 22.6\,\mu\mathrm{m}$ and $d_{water} = 11.4\,\mu\mathrm{m}$ for the sample with $\theta = 13.3°$ and $L = 61 \pm 1\,\mu\mathrm{m}$. So, the best pattern for this sample and this liquid was the one with a nominal unit width of $13\,\mu m$, which has a distances between consecutive waveguides of $11.3 \pm 0.1\,\mu m$. Once the pattern is chosen, similar measurements to the one done for the characterization of the waveguide pattern were performed. However, in this case the overlapping of the images cannot be performed, since the injection of the liquids can move slightly the sample. This problems is solved automatically once the device is equipped with pigtailing connections. A different solution was exploited to overcome this problem, for each sample several waveguides were kept without the channel, as a reference, in order to maintain the flexibility of the near field setup and still perform a quantitative analysis by the overlapping of the figure. The distance of the center of each output waveguides was normalized by the distances from the references waveguides. An example of such analysis is reported in figure 4.34, where the two images of the output waveguide on the top were shifted according to the reference waveguide position, in this way the two can be overlapped and compared in terms of distances. The two images represent the outputs with air and water inside the channel respectively (water on the bottom and air on the top). The difference of position is clear and well defined, thus demonstrating how the system can properly multiplexed the waveguide output by means of the microfluidic channel. By the overlapping of the profile in the plot in figure 4.34, the distance between the two outputs was measured by means of the gaussian interpolation of the profile. the example in the figure reports a value of $10.9\,\mu m$, which differs of less than $0.5\,\mu m$ from the expected value.

The difference in terms of intensities in figure 4.34 is due to the different dispersion depending on the liquid inside the channel, since Rayleigh's length depends on the refractive index. However, the output is clearly distinguishable and the air case is the worst possible intensity that can be achieved. In the case of higher refractive index liquid, the intensity increases.

The multiplexing is effectively demonstrated for all samples and all pattern from same measurements, the maximum difference from the expected value and the experimental one was $1\,\mu m$. This value is 1/10th of the maximum distance of the pattern, thus preventing any possibilities of mismatching of the waveguide outputs. Moreover, this error was the results of the systematic error from the procedure of positional normalization using the reference, since between the measurements of the output and the reference there was always a non negligible time interval, in which the sample can move due to small mechanical vibrations. Nevertheless, a future pigtailing connections will improve even more the system.

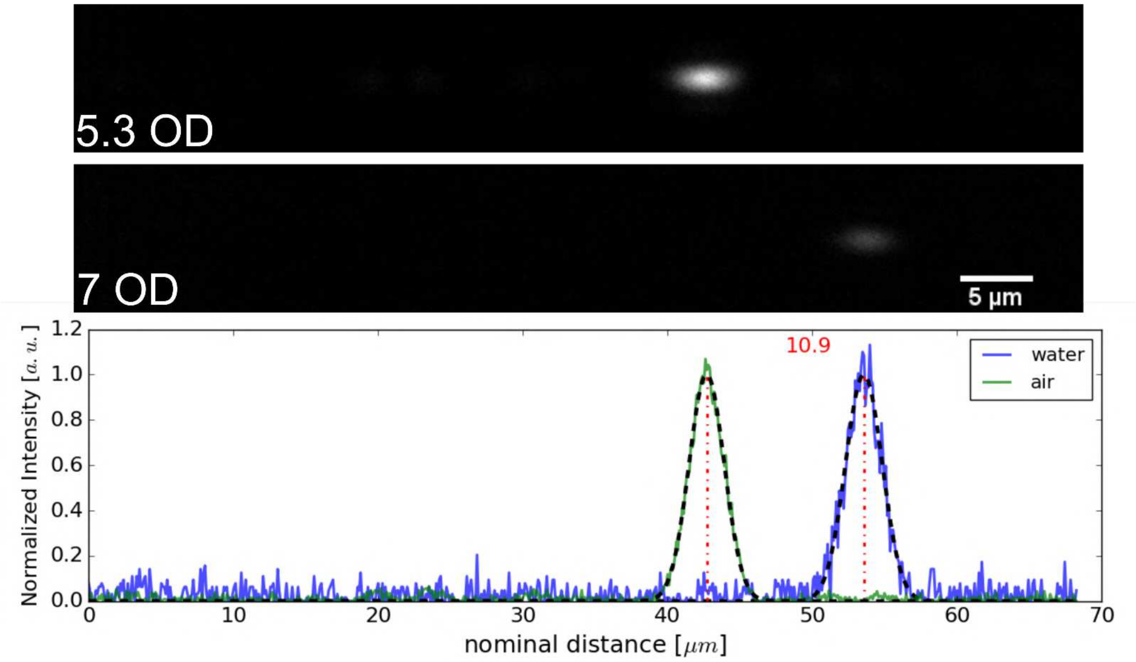

Figure 4.34. Example of analysis of a multiplexing actuated by the microfluidic channel: on the top there are two CCD near field Images of the output modes, where the OD on the left represents the optical used for avoiding the saturation of the camera. As expected, the top figure refers to the air, while bottom one to water, since higher refractive index corresponds to smaller dispersion. On the bottom, the plot reports the intensity profiles with gaussian fits (black lines) and relative centroids (red dashed lines), the red number represents the distance in microns between the two centroids.

Finally, a comparison between the calculated and the measured d is crucial for the prototyping stage of the device, and also to validate the working principle of the system. The analysis was performed fro both results for water in blue in figure 4.35 and in red for air. The plot shows the values of d normalized by the length of the channel varying the θ:

$$\frac{d(n_L, n_{LN}, \theta)}{L} = \frac{\sin(\alpha(n_L, n_{LN}, \theta) - \theta)}{cos(\alpha(n_L, n_{LN}, \theta))} \tag{4.11}$$

The quantity d presents also the dispersion boundaries due the beam waist during the crossing of the channel.

The water results are in agreements for all the θ range tested, validating the system. Instead the results for air are slightly lower for the highest angle, but these results could be explain by the approximation of gaussian beam, which does not describe the light behavior inside the channel for long light paths, such as the one for high angle and air. In particular air is not the best solution as a tester, since every time the channel should be dried in a perfect way and any

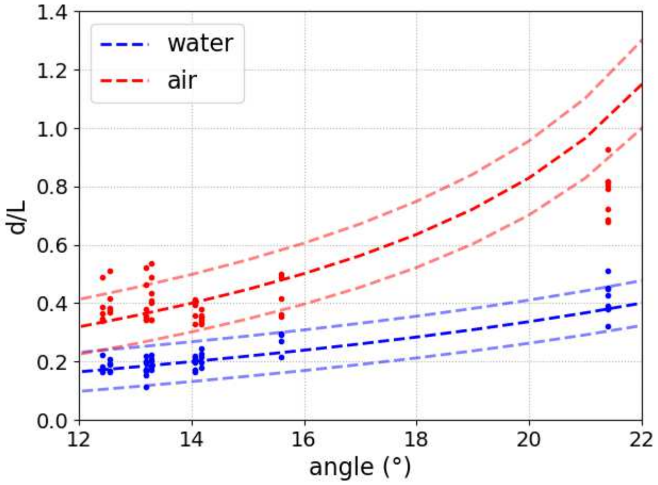

Figure 4.35. Comparison between the distance d *calculated and measured for water(blue) and air(red). The points represents the experimental points for different samples and patterns, and bright dashed lines represents the respective calculation, and the other transparent line represent the* $d - 0.5waist$ *and* $d + 0.5waist$*.*

residual droplet can be source of error.

In conclusion, this configuration proves how a microfluidic actuated optical device can be realized especially with the water, describing all the parameters that influences the performances. In particular, the width of the channel L, the angle of the channel θ, the pattern of the waveguides and the range of liquid index of refraction (n_L) can be tuned accordingly to the needs of the applications. This large amount of parameters that can be controlled opens the application range of this platform. Among the others, the multiplexing applications is clearly the most interesting one, but several future investigation have to be done, also combining more outputs and exploring others liquid and angles. Moreover, the microfluidic actuation opens the possibility of several optical application, such as spectral filter. For example, this latter can be achieved coupling a broad band source into the input waveguide, and tuning properly the dispersion relationship, in order to ob-

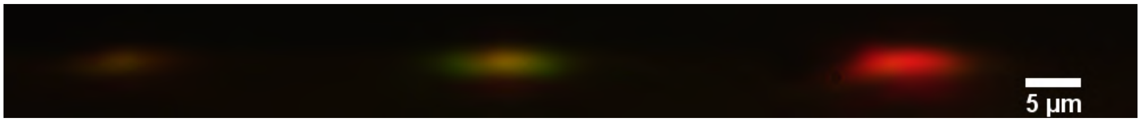

Figure 4.36. Example of the waveguides outputs, where a broadband in the visible range was coupled into the input waveguide, and due to the relation dispersion of the liquid inside the channel, each spectral component has different d*, and so it is coupled in different output waveguide of the pattern.*

tain different wavelength output in each of the waveguide outputs, as showed in figure 4.36. Another interesting application for such platform is the combination with the photovoltaic tweezers and liquid crystals, described in the next chapter. The integration of both stages could lead to the light actuated multiplexer, which can control also the polarization of the output, thanks to the exploitation of liquid crystals.

Chapter 5

Integration of a photovoltaic tweezer

The previous chapters demonstrated the feasibility of the realization of an optofluidic device in $LiNbO_3$ exploiting new studied microfluidic capabilities of this material, and its well-known optical potentialities. Despite this achievement, most of the starting interest gained by $LiNbO_3$ in lab-on-a-chip field was related to properties of manipulation stages, such as pyroelectricity [22], piezoelectricity [160] and photovoltaic effect [23]. A remarkable result in terms of lab-on-a-chip application could be the combination of both these tools on the same $LiNbO_3$ platform. In this chapter an example of such integration is presented. In particular, a sample of $LiNbO_3$ with the microchannel coupled with the waveguide is properly sealed with an iron doped lithium niobate cover, for photovoltaic tweezers (PT) application. The PT is one of the most promising application of the material in this field, and an integration with the optofluidic device previously described in this work could pave the way for a lab-on-a-chip realized in lithium niobate.
The iron doped $LiNbO_3$ can generate an electric field if illuminated by suitable wavelength light and geometry. The effect relies on the photogeneration of electrical carriers from the Fe^{2+} ions along *c*-axis, which can be trapped inside acceptors, such as those given by Fe^{3+}. In case of a non uniform illumination a space charge accumulation creates an effective potential difference and so an electric field. In the geometry hereby presented, the evanescent queue of this electric field penetrates into the microfluidic channel from the cover, thus interacting with the matter inside the channel. In such way, the optofluidic $LiNbO_3$ device is integrated with a PT, thus implementing on it a new tool for micromanipulation of ″objects″ by means of photoinduced electric field. This final configuration could be applied for plenty of lab-on-a-chip applications and also represents the first core building block for further integration exploiting others properties of the

material. For instance, the manipulation of liquid crystal (LC) director was controlled by the PT inside the microchannel and simultaneously was successfully monitored by the waveguide signal.
This chapter describes step by step the integration of this stage into the optofluidic chip and it is divided as follows:

5.1 The first section is dedicated to an analysis of the physics behind the PT in iron doped material, from the charge transport to one center model by Kukhtarev [161], which describes the photoinduced field generation in iron doped lithium niobate.

5.2 In the second the sample fabrication steps are reported with a complete discussion on the structural parameters of the Fe:LiNbO$_3$, and their influence on the PT properties. Then, the setup needed for the characterization of this new chip is presented.

5.3 Finally, in the last section the LCs actuation application is showed. During the LCs actuation, the simultaneous optical properties change is monitored by the transmission signal from the optofluidic system. These interesting results demonstrated the feasibility of such device for LCs actuation, and also proved the effectiveness of such integration and the coupling of the PT and the optofluidic substrate.

5.1 Iron doping of Lithium niobate

The photorefractive properties of $LiNbO_3$ is already described in the first chapter 1.2. In the following, the focus is on the effect provided by extrinsic centers in the material. Among the others, the transition metals attracted particular interest as dopant in $LiNbO_3$, since they present at least two valence states, which play the roles of donor and acceptor, respectively. Both states influence the charge transport process of the photorefractive effect.

5.1.1 Charge transport phenomena

There are three main contributions to the current of the photoinduced carriers: the drift, the bulk photovoltaic and the diffusion. Therefore the total current inside the material can be expressed:

$$\vec{j} = \vec{j}_{drift} + \vec{j}_{phv} + \vec{j}_{diff} \tag{5.1}$$

which has to satisfy the Poisson continuity equations:

$$\begin{aligned} \nabla(\hat{\epsilon}\vec{E}) &= \frac{\rho}{\epsilon_0} \\ \nabla \cdot \vec{j} + \frac{\partial \rho}{\partial t} &= 0 \end{aligned} \tag{5.2}$$

The drift current is due to the carriers interacting with an electric field $\vec{E}$, which correspond to the sum of an eventual external one, a space charge field generated by the separation of trapped carriers, and a pyroelectric field eventually promoted by the heating due to high intensity illumination. The latter can be neglected for an intensity less than $10^5 \mathrm{W/m^2}$ [162]. This current follows the Ohm's law:

$$\begin{aligned} \vec{j}_{drift} &= \hat{\sigma}\vec{E} \\ \hat{\sigma} &= q\hat{\mu}N \end{aligned} \tag{5.3}$$

where $\hat{\sigma}$ is the conductivity tensor, $\hat{\mu}$ is the mobility tensor of either holes or electron, depending on the carrier type considered, and N is the density of the carriers.

The bulk photovoltaic current is the contribution from the movement of the photoinduced carrier from the absorbing center to the nearest neighboring ions. This transfer is due to the non-centrosymmetric structure of the material, and the consequent preferred momentum of the carriers. The photoinduced charges can contribute to drift and diffusion as far as the thermalization was occurred. In fact, the photoinduced carriers contribute only to the photovoltaic current before thermalization, which is a current already described in 1.2 and characterized by the photovoltaic tensor β. The largest effect in $LiNbO_3$ can be obtained along the *c*-axis, which is often expressed in a scalar form as:

$$\frac{j_{phv,c}}{I} = \alpha k_G = \mu \tau_{phv} E_{phv,c} \alpha / h\nu \tag{5.4}$$

where k_G is the Glass constant, that takes into account the anisotropy of the crystals ($2.8 \cdot 10^{-11}\mathrm{m/V}$ for Fe:$LiNbO_3$), and α is the absorbing coefficient which depend on the wavelength and the compositional properties of the material. The Glass constant can be expressed as the mobility of the carriers μ divided by the energy of the photon $h\nu$, multiplied by the time constant τ_{phv} in which carriers contribute to the photovoltaic current, and by the phenomenological field E_{phv}, which moves the carriers.

The diffusion current is due to the spatially fluctuation of the carriers density, and it is proportional to the diffusion tensor of the carrier $\hat{D} = \mu \frac{k_B T}{q}$:

$$\vec{j}_{diff} = -q\hat{D}\nabla N = -\mu k_B T \nabla N \tag{5.5}$$

where N and μ are respectively the density and the mobility of the carriers considered.

5.1.2 One center model

The first model developed of the photorefractivity is the one center model by Vinetskii and Kukhtarev [161]. It describes many experimental results, such as photorefractivity of iron doped lithium niobate for low intensity illumination, i.e. $I < 10^4 - 10^5 \mathrm{W/m^2}$. In this model only one photorefractive center is considered, as the name suggests, and in the case of Fe:$LiNbO_3$ the center is the iron. It shows two possible valence states in $LiNbO_3$ Fe^{2+} or Fe^{3+}, which is carrier acceptor or donor, respectively. Kukhtarev described the carriers density evolution and their current by the following equations:

$$\begin{aligned}
\frac{\partial N_i}{\partial t} &= (sI + \beta_T) N_{Fe^{2+}} - \gamma_i N_i N_{Fe^{3+}} - \frac{\nabla \cdot \vec{j}}{q} \\
\frac{\partial N_{Fe^{2+}}}{\partial t} = -\frac{\partial N_{Fe^{3+}}}{\partial t} &= -(sI + \beta_T) N_{Fe^{2+}} + \gamma_i N_i N_{Fe^{3+}} \\
\vec{j} &= q\mu_i N_i \vec{E} - qD_i \nabla N_i + s N_{Fe^{2+}} k_G I \hat{j}
\end{aligned} \tag{5.6}$$

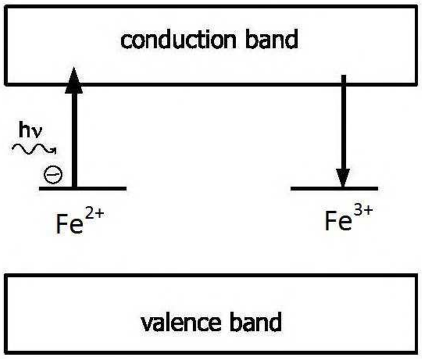

Figure 5.1. Sketch of the working principle of one center model for iron doped lithium niobate. One photon excites one electron from the donor state Fe^{2+} *to the valence band. The photoinduced electron can be trapped by an acceptor state Fe*$^{3+}$*. The electron moves in the conduction band by diffusion, drift and photovoltaic phenomenon between the excitation and the trapping moment.*

where I is the illumination intensity, N_i,γ_i, μ_i and D_i are respectively the density, recombination, mobility and diffusion constant of the carriers (either electrons or holes $i = e, h$), β_t is the thermal generation rate, $N_{Fe^{2,3+}}$ is the density of the acceptor or donor, s is the photoionization cross section and $\vec{E}$ is the total applied field (that is the sum of both external and space charge field). The current $\vec{j}$ is taking into account all three contributes from the charge transport: drift, photovoltaic and diffusion. The space charge field of this model should obey the Poisson continuity equation:

$$\nabla \cdot (\hat{\epsilon}\epsilon_0 \vec{E}_{sc}) = \rho = q(N_i + \Delta N_{Fe^{2+}}) \tag{5.7}$$

where $\Delta N_{Fe^{2+}}$ refers to the difference of donors density from the case without illumination. This latter equation can be simplified, since N_i (standard value $10^{14}\mathrm{m}^{-1}$) can usually be neglected compare to $\Delta N_{Fe^{2+}}$ (standard value $10^{24}\mathrm{m}^{-1}$). Moreover, the previous set of equations can be approximated by the adiabatic approximation, which states that the carriers are in a quasi equilibrium state with the traps distributions, $\frac{\partial N_i}{\partial t} = 0$. In lithium niobate this can be considered a good approximation for long illumination times, since the carriers density reaches a constant saturation value in few picoseconds. This approximation allows for stating that also $\frac{\partial N_{Fe^{2+}}}{\partial t} = 0$, which it does not mean that $N_{Fe^{2+}}$ is in a steady state, since the charge transports slowly gives a contribution. Thanks to this approximation, the model estimates the carriers density at any time and any place as:

$$N_i = \frac{(sI + \beta_T)}{\gamma_i} \frac{N_{Fe^{2+}}}{N_{Fe^{3+}}} \tag{5.8}$$

From this latter equation combined with the definition of the conductivity by the Ohm's law (equation 5.3), the following definition can be derived:

$$\sigma_i = q\mu_i \frac{sI}{\gamma_i} \frac{N_{Fe^{2+}}}{N_{Fe^{3+}}} + q\mu_i \frac{\beta_T}{\gamma_i} \frac{N_{Fe^{2+}}}{N_{Fe^{3+}}} = \sigma_{phv,i} + \sigma_{dark,i} \tag{5.9}$$

The conductivity σ_i shows clearly two contributes: one the so called *photoconductivity* $\sigma_{phv,i}$, which is non zero only if the material is illuminated, and $\sigma_{dark,i}$ so called *dark-conductivity*, which does not depend on the illumination, but only on the thermal excitation of carrier. It is worth mentioning that both conductivities depend on the reduction degree $\frac{N_{Fe^{2+}}}{N_{Fe^{3+}}}$ of the material, since it can be experimentally controlled by thermal treatments.

5.1.3 Non homogeneous illumination solution

A non homogeneous illumination increases the grade of complexity of the previous equations (eq. 5.6). The simplest case to approach the non homogeneous illumination solution is the interference of two beam along *z*-axis:

$$I(z) = I_0(1 + m\sin(\vec{k} \cdot \hat{z})) \tag{5.10}$$

where $I_0 = \frac{I_1+I_2}{2}$ is the average of the two beams intensities, $m = \frac{I_{max}-I_{min}}{I_{max}+I_{min}}$ is the visibility of the pattern, $\vec{k} = \vec{k}_1 - \vec{k}_2$ is the difference of the beam wavevectors. The solution to describe the carriers density into the material [161] was first obtained developing all the three main equations of the one center model (eq. 5.6) in Fourier series, since they depend only on the spatial coordinate $\hat{z}$. In the case of a small modulation $m \ll 1$ only zero and first terms can be taken into account, in fact each term of the Fourier expansion decreases as m^f, where *f* is the counter of Fourier terms. Each variable of the three main equations ($F = \vec{E}$, $N_{Fe^{2+}}$, $N_{Fe^{2+}}$, N) can be expanded as $F = F_0 + F_1 e^{i\vec{k}\cdot\hat{z}}$. Thus, the three main equations (eq. 5.6) simplify as follows:

$$\begin{aligned} E_{sc} \approx E_1 &= -\frac{E_0 + E_{phv} + iE_D}{1 + E_D/E_q - iE_0/E_q - iE_{phv}/E_q^{'}} \\ E_{phv} &= \frac{j_{phv}}{\sigma_{phv}} = \frac{k_G \gamma_i}{q\mu_i} N_{Fe^{3+}} \\ E_D &= \frac{k_B T}{q} K \\ E_q &= \frac{q}{\epsilon\epsilon_0 K}\left(\frac{1}{N_{Fe^{2+}}} + \frac{1}{N_{Fe^{3+}}}\right)^{-1} \\ E_{q'} &= \frac{q}{\epsilon\epsilon_0 K} N_{Fe^{2+}} \end{aligned} \tag{5.11}$$

where E_D is the diffusion field, E_{sc} is the space charge generated electric field, E_q and $E_q^{'}$ are the space charge limiting fields respectively, and $K = \vec{k} \cdot \hat{z}$. When both the spatial frequency and the light pattern are fixed, E_q represents the maximum field that can be generated by the movement of the electrons inside the material. In Fe:LiNbO$_3$ the diffusion field E_D is negligible compared to the photovoltaic one E_{phv} for light modulation larger than $1\,\mu\mathrm{m}$, thus E_{sc} has the same phase of the light pattern. The one center model gives also information in time evolution of the space charge field, which is described by an exponential behavior in the case of a sinusoidal illumination. The time constant of this phenomenon can be calculated as:

$$\begin{aligned} \tau_{sc} &= \frac{1 + (E_D - iE_0)/E_M}{1 + E_D/E_q - iE_0/E_q - iE_{phv}/E_q^{'}} \tau_M \\ E_M &= \frac{\gamma_i N_{Fe^{3+}}}{\mu_i} \frac{1}{K} \\ \tau_M &= \frac{\epsilon\epsilon_0}{\sigma_{ph,i} + \sigma_{dark,i}} \end{aligned} \tag{5.12}$$

5.1.4 Comparison with experimental data: simplified version

In this work, the one center model results can be further simplified by taking into account several assumptions:

$i = e$, the previous equations are the same for both holes and electrons and in general, both of them can be involved in the charge transport. However, the electrons dominate over holes in transports processes for visible light and iron doped lithium niobate [162, 163], as a consequence in the case here under study it holds $i = e$.

$E_0 = 0$, in our experimental setup no external field were applied to the material.

$E_q \gg E_D$, $E_q^{'} \gg E_{phv}$, there are not limiting effect, which means that the material have enough donor and acceptor to support the space charge field. This is the case studied herein, since the material was always strongly doped.

$E_{phv} \gg E_D$, the modulation was larger than $1\,\mu\mathrm{m}$.

The first conclusion that can be made from these considerations is that $E_M \gg E_D$, and consequently $\tau_{sc} \approx \tau_M$. The substitution of equations 5.10 and 5.11 in One center model time evolution equation 5.6 combined with the aforementioned assumptions, gives rise to the following simple result for the space charge field time behavior:

$$E_{sc} = -E_{phv}(1 - e^{-\frac{t}{\tau_{sc}}}) \tag{5.13}$$

where E_{phv} is the photovoltaic field and it represents also the saturation value for E_{sc}. Such description can be directly compared to the fitted data and provides a feedback to tune the Fe concentration and the reduction degree. Indeed, several useful dependencies can be obtained:

$$j_{phv} \propto I N_{Fe^{2+}} \tag{5.14}$$

$$\tau^{-1} \propto \sigma_{phv} \propto I \frac{N_{Fe^{2+}}}{N_{Fe^{3+}}} \tag{5.15}$$

$$E_{phv} \propto N_{Fe^{3+}} \tag{5.16}$$

5.2 Fe:LiNbO$_3$-optofluidic device characterization

In this work the Fe:LiNbO$_3$ substrate covers the opto-microfluidic platforms instead of the glass of the previous chapter. In this way, a new manipulation tool can be integrated without any new fabrication steps and without loosing any capabilities provided by the optofluidic substrate. Indeed, the integration of a Fe:LiNbO$_3$ onto the optomicrofluidic device is straightforward, just by following the same procedure described in section 2.1 for the glass. In figure 5.2 a sketch of the final device is reported, where the photovoltaic eletric field is induced from the upper part of the device. In this way, there is no restriction to the illumination pattern by the device configuration, since the monolithic Fe:LiNbO$_3$ cover the whole microfluidic circuit. Therefore, the electric field can be induced in every desired position on the cover, and the consequent evanescent field can be generated in every section of the microfluidic circuit, either in front of waveguide either in the junction. This feature opens the field of applications drastically: on one hand any light pattern can be realized as well as every electric field modulation, on the other this pattern can be freely positioned respect to the microfluidic circuit. This configuration allows, indeed, an independent control of each device features: the microfluidic channel by fluids injections from the tubes on the top, the waveguide by the injection of the light on two sides, and the photoinduced electric field by the illumination from the top in-between the tubes.

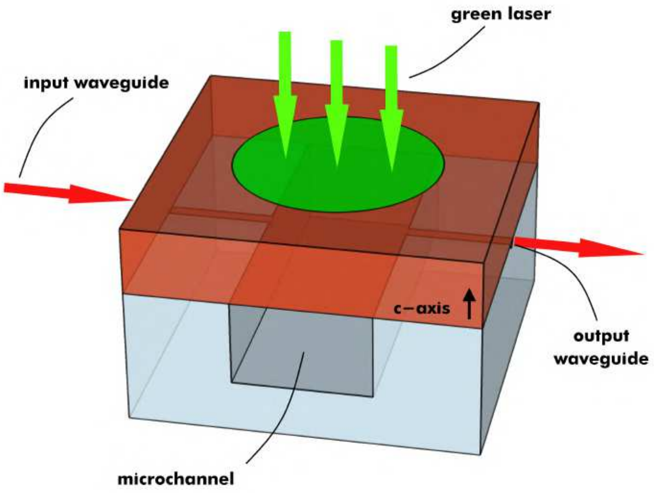

Figure 5.2. The sketch represents the final lab-on-a-chip realized in lithium niobate. The cover in brown is the iron doped material, which acts as a PT illuminated by the green laser. The substrate on the bottom is the optofluidic device described in previous chapters. The matter inside microfluidic channel is at the same time monitored by the waveguides, thanks to the effective coupling, and it can be manipulated by the PT.

The only new developments needed for this upgraded device are related to the green illumination and the fabrication of Fe:LiNbO$_3$ covers. Indeed, the physical properties of the sample have strong influence on its photovoltaic response, thus making the control on these properties crucial for the performances of the device.

5.2.1 The integration of Fe:LiNbO$_3$

The Fe:LiNbO$_3$ samples used to close the opto-microfluidic circuit were grown by Czochralski technique, which allows to control the concentration of dopants inside the material. The samples grown, reduction degree thermal modification and samples cuts were carried out by the group of matter physics of Department of

Physics and Astronomy of University of Padova. In particular, boules of congruent lithium niobate with different iron concentrations were grown with a diameter of $1.7\,\mathrm{cm}$ oriented along z-axis. Then, the flat z-cut flat samples were obtained by the boule slicing with a thickness of 1 and $1.3\,\mathrm{mm}$ by means of a South Bay 540 machine equipped with diamond coated blade. The cut was performed after a precise crystalline alignment, exploiting X-ray diffraction measurements. The cleaning procedure after the cut was made of baths in acetone and isopropanol in ultrasonic cleaner for ten minute each. The reduction degree was tuned by thermal treatments in different atmosphere, done in a tubular furnace Hochtemperatureofen Gmbh (model F-VS 100-500/13) by Gero: an oxidizing atmosphere induces a decrease in the reduction degree, while the reducing atmosphere promotes the reduction of iron its Fe^{3+} to Fe^{2+} states. Several parameters have to be controlled in order to obtain the desired concentrations, such as time, temperature, the inert gas composition with O_2 or H_2 and temperature ramps. Once performed the thermal treatment, the samples concentrations can be measured by absorbance measurements, thanks to the fact that the two iron valence states modify the absorbance band of the material. A complete description of from the growths to the thermal treatment is reported in [164].

The $Fe:LiNbO_3$ bilk doped crystals were then polished on both on z-faces. This technique was realized by means of lapping and polishing machine PM5(Logitech Limited, Glasgow, UK), and the roughness were reduced after two steps, exploiting two different size aluminium oxide powder, the first one with $9\,\mu\mathrm{m}$ and the finest with $3\,\mu\mathrm{m}$ size. On average $300\,\mu\mathrm{m}$ were lapped form both sides of the sample. This lapping step guaranteed a roughness of $9\,\mu\mathrm{m}$ (root mean square). The final step to achieve an optical quality ($R_a < \frac{\lambda(nm)}{10}$), was a polishing process by means of SF1 Polishing Fluid (Logitech Limited, Glasgow, UK).

Finally the both side polished z-cut samples with desidered reduction degree and Iron concentration were integrated in the optofluidic device in the way described in section 2.1: the microfluidic connections were realized drilling the holes into the sample and connection tubes, and the sealing were achieved by means of the NOA68 (Nordland optics UV curable glue).

5.2.2 Characterization setup

The setup for characterizing the integration of the $Fe:LiNbO_3$ cover is the same described in section 3.2 regarding the red beam, but in addition it has a green laser line for the excitation of the photoinduced field. The green beam has to illuminate the cover directly, without passing through the LiNbO$_3$ substrate in order to optimize the photovoltaic effect. Indeed, both the bottom of the microfluidic channel and the lithium niobate device itself can modify the beam profile of the spot on the iron doped cover, thus preventing a full control of the photovoltaic effect and the illumination area. For this reason, the laser beam illuminates the cover from the top. The final setup is sketched in figure 5.3. The green laser used

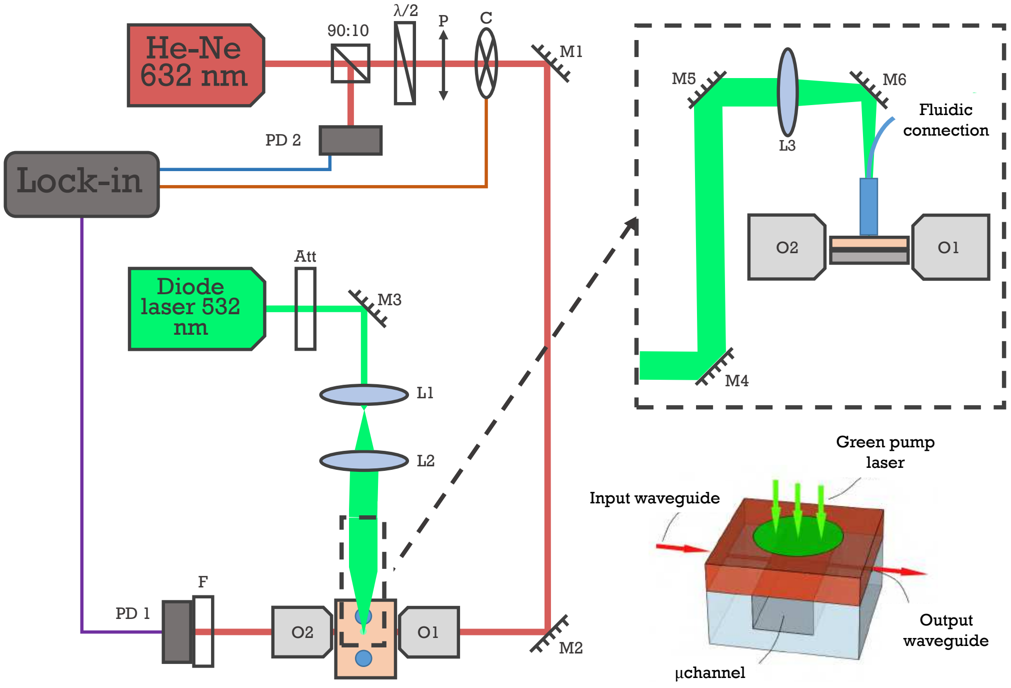

Figure 5.3. Sketch of the setup used with the devices covered by an iron doped lithium niobate cover. On the left, there is an overall view of the setup: the He-Ne laser is coupled into the waveguide with the objective (O1) as the setup describe in section 3.2, then the signal is recollected by O2 and read by a photodiode PD2 coupled with a green-line filter. The polarization of He-Ne laser is controlled by a half-wave plate and a polarizer, and 10% of its intensity is used as normalization signal and recorded by PD2. The intensity signal is amplified by a Lock-in, and normalized by the signal from PD2. The continuous diode laser at $532\,\mathrm{nm}$ *is first expanded with two lenses (L1, L2) in order to tune the waist of the beam, then another lens (L3) focus it on the spot, which is determined by the cross between the channel and the waveguide.*

for the generation of the photoinduced field is a diode laser with a effective power of $66.3\,\mathrm{mW}$. The power of the beam can be controlled using an variable attenuator (Att. in fig. 5.3). At the end of the configuration showed in fig. 5.3, the spot of the beam on the top of the cover is an ellipsoid with axis $955 \pm 1\,\mu\mathrm{m}$ and $817 \pm 1\,\mu\mathrm{m}$

(measured the FWHM of the two profiles), and an area of $2.45 \pm 0.01\,\mathrm{mm}^2$. The size of this spot allows to have an homogeneous intensity over the channel width (i.e. $200\,\mu\mathrm{m}$), thus an homogeneous evanescent photoinduced field is created inside the channel. The visible waveguide presents in the underneath optofluidic device in principle can guide also green light, however in this setup most of the light is absorbed by the iron doped cover and due to the device configuration a random coupling of green light laser is rare. Nevertheless, a spectral notch filter (F in fig. 5.3) around $532\,\mathrm{nm}$ is used to avoid that any undesidered green light scattering by the channel walls enters in the final detector which is positioned after the output waveguide.
The coupling beam configuration is almost the same of section 3.2. The main difference is in the acquisition system, since the requirement for the liquid crystal application is the measurements of the optical transmission signal from the waveguides. The near field setup is coupled with a photodiode, which gives a current signal proportional to the light intensity. This signal is amplified by a phase sensitive amplificator, in order to cut signal noise. The only frequency amplified by this lock-in is the one applied by the chopper wheel (C in fig. 5.3). Moreover, this setup allows for collecting $10\,\%$ of the original beam by a beam splitter, in order to normalize the signal over the laser intensity variations (PD 2 in fig. 5.3).

5.3 An Application: integrated light-controlled Liquid crystals cell

Among the possible applications of this device, surely one of the most promising is represented by its combination with liquid crystals (LCs), thanks to the photovoltaic effect of $LiNbO_3$ and the sensitivity to the external electric fields of LC. As a matter of fact, a LCs cell using $LiNbO_3$ as active substrate has been already presented in [165–169], and in particular the light-induced photovoltaic control of the LCs orientation was demonstrated. Another recent publication [170] shows how such LCs cells can be efficiently implemented in a microfluidic configuration: in [170] the authors report a device where LCs can injected in a microfluidic channel and external light beams are used to monitor the orientation of LCs molecules. Although these interesting results, such cells still lack of a full integration between the microfluidic and the light-driven components. In this thesis a reliable overcome of this lack is proposed by the exploitation of this optofluidic device. The LCs inside a micro-optofluidic circuit are controlled by the photoinduced field generated by the cover, and at the same time their orientation are monitored by the waveguide transmission signal. This orientation can be varied upon demand by the photovoltaic actuation of the iron doped lithium niobate cover in order chose the desired signal transmission from the waveguide. The LCs used for this purpose are 5CB.

5.3.1 5CB Liquid crystal

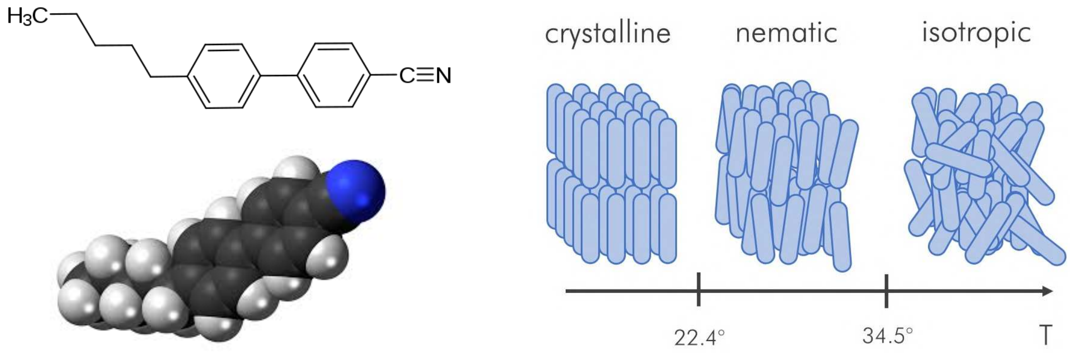

Figure 5.4. On the left molecular structure of 5CB liquid crystals. In partcular the bottom figure is taken from On the right three structure phases of thermotropic 5CB with the transitions temperatures.

4-Cyano-4-pentylbiphenyl $C_{18}H_{19}N$ (figure 5.4) or commonly called 5CB are thermotropic uniaxial nematic liquid crystal first synthesized by Gray, Harrison and Nash in 1973 [171]. They presented the three standard thermotropic phases depending on the temperature: crystalline below temperature of $22.4\,°C$, nematic between $22.4\,°C$ and $34.5\,°C$ and isotropic above $34.5\,°C$ [172].

Nematic phase and director

The nematic[1] phase is characterized by no specific positional order (i.e. no-long range order with respect to gravity centers of the molecules, like a liquid), and by a long order in term of average the direction of molecules [174], this preferential orientation is described by the *director* $\hat{n}$ (i.e. the direction average of molecules alignment). The difference with isotropic phase (i.e. no order both positional

---

[1] *nematic* $\nu\eta\mu\alpha$ from greek = thread, first cited by Friedel [173] (1992), due to the thread-like defects in this phase.

and directional) and crystalline phase (i.e. high positional and directional orders) are described by an *order parameter*. The description of this parameter can be made adopting several approaches [174], the most intuitive and simple one for the uniaxial nematic LC, such as 5CB, is the microscopic approach. In this frame, the LC molecules can be represented in good approximation as rigid rods, which cannot interpenetrate each other. Like LC molecules, the rods have cylindrical symmetry about its main axis, which is described by a versor $\hat{a}$. In agreement with the figure 5.5 the components a can be defined as:

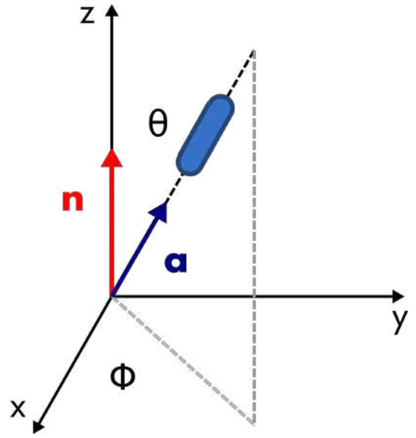

Figure 5.5. Reference frame for the liquid crystal, â in blue is versor representing the rod direction, $\vec{n}$ is the director of the system.

$$\hat{a} = \begin{pmatrix} \sin\theta\cos\phi \\ \sin\theta\sin\phi \\ \sin\theta \end{pmatrix} \tag{5.17}$$

where the reference frame (figure 5.5) is taken as the one where z-axis is aligned with $\hat{n}$, and each component is expressed in terms of polar angles θ and ω. The distribution of the angle position of the axis $\hat{a}$, and so the rods alignment, can be described by a distribution function $f(\theta, \phi)d\Omega$, where $d\Omega = \sin\theta d\theta d\phi$ is the small solid angle. The nematic phase has rotational symmetry about $\hat{n}$ and it is symmetric in the change $\hat{n} \to -\hat{n}$, therefore $f(\theta, \phi) = f(\theta) = f(\pi - \theta)$. The alignment distribution can be described with the average:

$$\langle \hat{a} \cdot \hat{n} \rangle = \langle \cos\theta \rangle = \int f(\theta)\cos\theta d\Omega = 0 \tag{5.18}$$

which it gives a trivial solution, since$f(\theta)$ has maximum for $\theta = 0$ and $\theta = \pi$, minimum for $\theta = \frac{\pi}{2}$ and it is symmetric about this latter. However, this integral can be considered as the dipole from a multipole expansion. The next multipole non trivial is the quadripole:

$$S = \left\langle \frac{3cos^2\theta - 1}{2} \right\rangle = \int f(\theta) \frac{3cos^2\theta - 1}{2} d\Omega \tag{5.19}$$

It is clear how S is a measurement of the alignment and thus an order parameter: when $\theta = 0$ or $\theta = \pi$ the versors $\hat{a}$ are all aligned in the same direction of $\hat{n}$ and $S = 1$, on the other hand if $\hat{a}$ has a perpendicular alignment respect to $\hat{n}$ (i.e. $\theta = \frac{\pi}{2}$) $S = -\frac{1}{2}$, and with a random distribution (i.e. $\langle \cos^2\theta \rangle = \frac{1}{3}$) $S = 0$. The three phases can be described quantitatively in terms of orientational order of the molecules by using the parameter S.

The order parameter S describes in this way the anisotropic behavior of the system, which makes the LCs highly susceptible to external fields. For instance, the magnetic anisotropy favors an alignment of $\hat{n}$ to an external magnetic field always positive. The same alignment happens for an external electric field because of the anisotropy of dielectric constant $\Delta\epsilon = \epsilon_{\parallel} - \epsilon_{\perp}$, which in the case of the 5CB is always positive, so $\hat{n}$ aligns with the electric field. Therefore, in the case of optical frequencies, the LCs show a birefringent behavior with $\hat{n}$ corresponding to the optical axis, where the two refractive indices are $\sqrt{\epsilon_{\parallel}} = n_e$ and $\sqrt{\epsilon_{\perp}} = n_o$ [175]. For 5CB, the two values are n_o =1.518 and n_e =1.682 at room temperature and at 632.8 nm.

A more accurated description [176] of the LC can be given combining the order parameter S and the director $\hat{n}$ in the order parameter tensor $Q_{ij} = S\left[\hat{n}_i\hat{n}_j - \frac{1}{3}\delta_{ij}\right]$ by the so called Frank-Oseen free energy:

$$\begin{aligned} g =& \frac{1}{2}K_{11}(\nabla \cdot \hat{n} + \frac{K_1}{K_{11}})^2 + \frac{1}{2}K_{22}(\hat{n} \cdot (\nabla \times \hat{n}) - \frac{K_2}{K_{22}})^2 && (5.20) \\ &+ \frac{1}{2}K_{33}(\hat{n} \times (\nabla \times \hat{n}))^2 - \frac{1}{2}K_{12}(\nabla \cdot \hat{n})(\hat{n} \cdot (\nabla \times \hat{n})) && (5.21) \end{aligned}$$

where the K_i and K_{ij} are the curvature elastic constants relative to each possible deformation, as depicted in figure 5.6. The presence of an external magnetic or electric field has strong influence on the deformation of the director direction, due to the high anisotropy of the system. In particular, the additional energetic

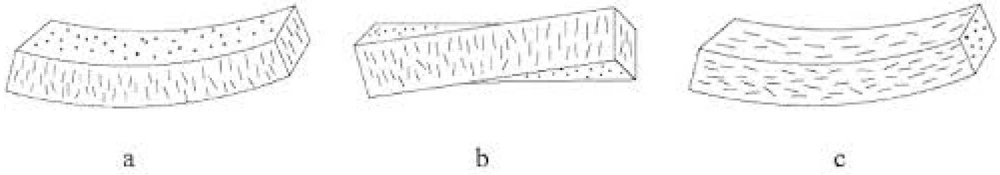

Figure 5.6. The three deformation of uniaxial LCs: splay, twist and bend from left to right respectively. Image taken from [176]

term for an electric field $\vec{E}$ acting on LCs molecules is:

$$g_e = -\frac{1}{8\pi}\epsilon_\perp E^2 - \frac{1}{8\pi}\epsilon_a(\hat{n}\cdot\vec{E})^2 \tag{5.22}$$

The deformation that the device aims to control is the one relative to the above energetic term, where $\vec{E}$ is the evanescent part of the photoinduced field created inside the channel.

Optical properties

As aforementioned, 5CBs present a strong anisotropic dielectric constant $\Delta\epsilon = \epsilon_\parallel - \epsilon_\perp$, which describes the dielectric susceptibility difference respect to the direction parallel and perpendicular to the director, respectively. This difference leads to the birefringency of the material and the difference in terms of refractive indices. In general, a light beam that enters in a birefringent material, is splitted into the two polarization components, which travel with different velocities inside the material. At the end of the sample, the beam has a polarization state depending on the recombination of these two components. In a quantitatively way, the description can be given by a simple 2D formalism [177]. If the entering light has a linear polarization with an angle θ with the director $\hat{n}$, the components are described as:

$$\vec{E}_{in} = \begin{bmatrix} E_0\cos\theta \\ E_0\sin\theta \end{bmatrix} \tag{5.23}$$

the two components are perpendicular to the propagation direction. After passing through the LCs, it becomes elliptically polarized due to the birefringency previously described:

$$\vec{E}_{LC} = \begin{bmatrix} E_0\cos\theta\exp(ik_eL) \\ E_0\sin\theta\exp(ik_oL) \end{bmatrix} \tag{5.24}$$

where L is the length of the LCs sample, $k_e = \frac{2\pi}{\lambda} n_e$ and $k_o = \frac{2\pi}{\lambda} n_o$ are the propagation vectors along same direction of L (the reference frame is chosen to consider only one component of these vectors). These two components can be analyzed with a polarizer at the same angle of the initial polarization. In [177] the matrix describing the polarizer is:

$$\bar{\bar{P}} = \begin{bmatrix} \cos^2\theta & -\cos\theta\sin\theta \\ -\cos\theta\sin\theta & \sin^2\theta \end{bmatrix} \tag{5.25}$$

Therefore, the intensity can be calculated as:

$$|\bar{\bar{P}}\vec{E}_{LC}|^2 = E_0^2 \cos^2(2\theta) \sin^2 \frac{\pi \Delta n L}{\lambda} \tag{5.26}$$

With a monochromatic light the intensity depends only on the L and $\Delta n = n_e - n_o$. For $\theta = \frac{\pi}{2}$ the transmission is zero. Without the polarizer, the transmission on the signal is minimum when the polarization of the initial beam is aligned with the smallest value of the index of refraction, and vice versa is maximum when the polarization of the initial beam is aligned with the highest value of the index of refraction. This is a free space propagation description, which can not be applied to the optofluidic system. However, it gives an explanation on how the intensity of a beam can be modified by LCs. In fact the liquid crystal inside the channel acts in a similar way with the beam from the waveguide output.

Anchoring

The orientation of LCs respect to an interface, i.e. *anchoring*, is crucial for the realization of any kind of devices involving LCs actuation. Their behavior strongly depends on the properties of the material, the morphology and the physical interaction between the LCs molecule and the surface. Three main cases observed are:

hometropic anchoring, when $\hat{n}$ is perpendicular to the interface,

uniform planar anchoring, when $\hat{n}$ is aligned to a well defined direction parallel to the interface,

random planar anchoring, when $\hat{n}$ is parallel to the interface, but with an arbitrary alignment in this plane.

The alignment is defined by the interplay between steric interaction and elastic behaviors of the molecule. The most common technique for achieving a uniform planar anchoring is a mechanical rubbing, which consists in a friction procedure after a polymer coatings on the substrate, in order to produce a grooves pattern. However, this technique cannot be applied for microfluidic devices, in fact closed microfluidic channels inhibits any kind of intrusive methods. Several alternative techniques were studied depending on the material and the final desired anchoring, such as patterned surfaces [178] or non intrusive surfaces [179].
The anchoring of a photoactuated LCs cell in $LiNbO_3$ should be orthogonal to the alignment of the photoinduced electric field in order to allow for a reorientation by this latter. In particular, in this work the anchoring have to be uniform planar, since the photoinduced field by $Fe:LiNbO_3$ is orthogonal to the surface. 5CBs exhibit such an alignment on substrate of untreated $LiNbO_3$, as demonstrated in several papers on photoactuated LCs cells [167, 168, 170]. Moreover, two other effects favor this anchoring: the morphology in the bottom of the engraved channel, which presents scratches in the bottom in the direction of the channel as showed in figure 2.2, and the capillary flow of LC inside the channel [180].

5.3.2 Photoinduced actuation and waveguided signal

The simultaneous readout of the alignment of the LCs throughout the waveguide transmission signal is presented in this section. The LCs director alignment inside the microchannel affects directly the two polarization components of the red beam across the channel, since the index of refraction seen by the two components is different $\Delta n = n_e - n_o = 1.682 - 1.518 = 0.164$. So, the actuation of 5CBs inside the channel by means of the photoinduced field allows for changing their orientation from the starting anchoring orientation (i.e. parallel to the flow direction and channel main direction) to the final alignment with the evanescent electric field. If the red light from the waveguide in the channel is polarized, the transmission signal is simultaneously sensitive to the described rotation (figure 5.7).

The red beam polarization was aligned with the direction of photoinduced field, which is the direction of the orientation direction of the LCs after the actuation. The choice of this polarization should imply an increase of the signal when the green light is on. First test was made using a $Fe:LiNbO_3$ cover with an

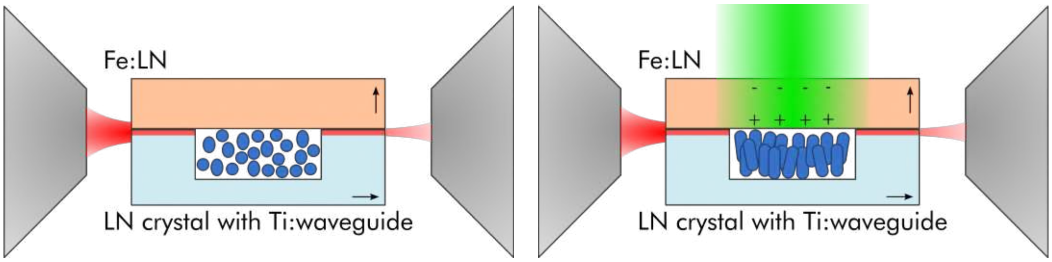

Figure 5.7. These two sketches on the left represent the two states of the device: on the left when the green light is off and the orientation of LC follows the flow direction, on the right instead the green laser is on and the dipole interaction of LC with photoinduced field forces LC to align in the field direction. Two little black arrows represents the z-axis of the two LN samples.

$0.1\,\mathrm{mol}\,\%$ and with a reduction degree of 0.033. This value of reduction degree guaranteed an high concentration of Fe^{3+}, which is proportional to the saturation photoinduced field E_{phv}, in equation eq:Edep. Since the reduction degree can be controlled by thermal treatments, every desired reduction degree can be chosen depending on the application. As first test, the maximum value of electric field should be highest as possible in order to be sure to observe the effect. As showed in graph 5.8, the transmission signal rises at the turning on of the laser.

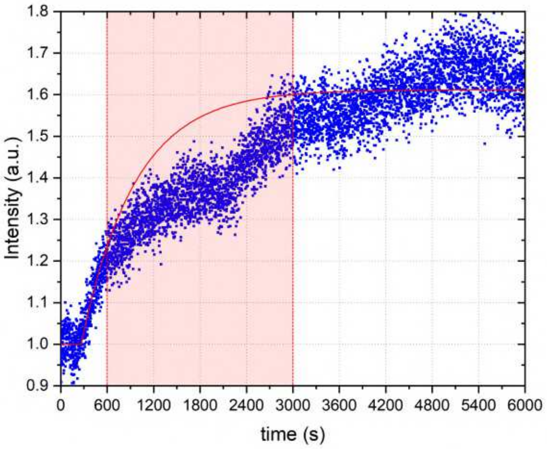

Figure 5.8. The graph represents the transmitted signal (i.e. Intensity in y-axis) throughout the waveguide, during a photoactuation by means of a green laser at $66\,\mathrm{mW}$*. The lighting time of the latter was at* $200\,\mathrm{s}$*. The iron doped cover features for this measurements were* $0.1\,\mathrm{mol}\,\%$ *of iron concentration and a reduction degree of* 0.033*. The red line represent the fitted curve of 5.27, where points from* $1200\,\mathrm{s}$ *and* $3000\,\mathrm{s}$ *were not considered.*

Several considerations have to be made from this graph. Firstly, the transmitted intensity signal is constant for the first $200\,\mathrm{s}$ and suddenly it increases. The switching on instant of the green laser t_{on} corresponds exactly to $200\,\mathrm{s}$. The absence of any delay between t_{on} and the start of signal rise confirms the effectiveness of the LCs photo-actuation. In particular, it suggests that the LCs rotation time is negligible compared to the time needed for the generation of the photoinduced field, which is equal to the carrier generation time and their transport in Fe:LiNbO$_3$. Indeed, there is no delay between the raising time of the transmitted signal and the lighting time of the photo-actuation. This result is also confirmed theoretically, considering the time scale involved in the system:

- the time scale of the LC rotation $\tau_{on} = \frac{\gamma_1}{\epsilon_0 |\Delta\epsilon| E^2}$ and for typical photoinduced field $10^5 - 10^6 \mathrm{V\,m^{-1}}$, ranges from $1\,\mathrm{ms}$ to $1\,\mathrm{s}$ (5CBs: $\gamma_1 = 66\,\mathrm{mPa\,s}$, $\Delta\epsilon = 0.5248$);

- For the intensity used in this work the time scale of the photoinduced τ (eq. 5.15) ranges from tens to hundred of seconds, much higher than the time scale of the LC rotation.

Secondly, the variation of the signal recorded by the waveguide is only influenced by the presence of the LCs inside the channel, because the same experimental conditions measurements were performed with with water and the signal does not present any similar increasing behavior, as shown in figure 5.9. Therefore, any change of the transmission signal due to the effect of the photoinduced field or to the green light on the waveguide properties should be neglected. As a consequence of these two considerations, the transmission signal should follow exactly the exponential behavior described in equation 5.13. Indeed, as far as the evanescent photoinduced field increasing, it should interact with LCs deeper in the channel, because the electric field threshold for the interaction is reached in deeper distance from the Fe:LiNbO$_3$ surface. In this way, the electric field aligns consequently LCs deeper in the channel, and the amount of aligned LCs increases, thus inducing an increase of the red light beam transmitted signal proportional to the amount of LCs oriented. Finally the transmission signal is expected to have the same time behavior of the field:

$$I = I_{sat}(1 - e^{-\frac{t}{\tau_{sc}}}) \tag{5.27}$$

where τ_{sc} is the same of equation 5.13, and I_{sat} is the maximum intensity when the field is equal to the saturation field E_{phv}.However, the red fit in figure 5.8

shows clearly a bad interpolation of experimental especially in the range between $1200\,\mathrm{s}$ and $3000\,\mathrm{s}$. This behavior of the data is due to the fact that equation 5.13 was obtained in approximation of light modulation $m << 1$. This approximation does not fit well with the gaussian illumination of this device, so that other fourier terms should be considered in the expansion. Nevertheless, it is always a good approximation for $t < \tau$ due to the fact that higher harmonics of the space-charge field grow slower than fundamental one. This behavior is evident in figure 5.8, where the data with $t < 600\,\mathrm{s}$ is well described by the red curve, and the $\tau = 692 \pm 14\,\mathrm{s}$. This value confirms that the correspondence between the photoinduced electric behavior and the transmission signal one is really mediated by the actuation of the LCs inside the channel.

In addition to the proof of the working principle provided by the previous measurements, the next step was the demonstration of how this actuation can be tuned by varying the compositional parameters of the Fe:LiNbO3. As explained before, the reduction degree of the material can be modified by thermal treatments to obtain the desired value. Since τ_{sc} depends on the reduction degree (equation 5.15), same samples can show faster or slower behavior, after a thermal treatment. In order to test such tunability of the device, the same sample used for the previous measurements underwent a reduction treatment to increase the

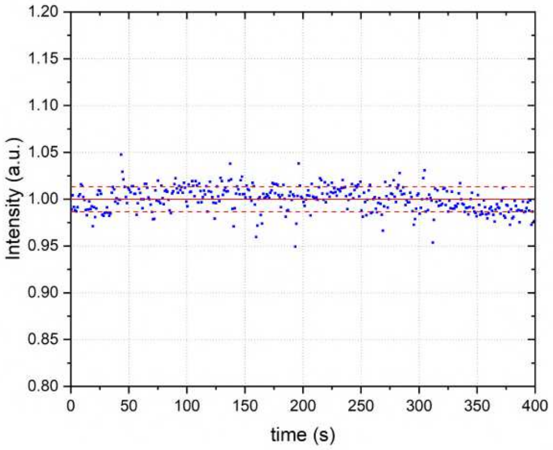

Figure 5.9. The graph represents the transmitted signal (i.e. Intensity in y-axis) throughout the waveguide, during a photoactuation by means of a green laser at $66\,\mathrm{mW}$ *with water inside the channel. The switching on time of the latter was at* $200\,\mathrm{s}$*. The iron doped cover features for this measurements were* $0.1\,\mathrm{mol}\,\%$ *of iron concentration and a reduction degree of* 0.033*. The red line represents the mean value, while the dashed ones have one standard deviation of distance.*

reduction degree (i.e decrease the concentration of antisite Fe^{3+} and at the same time increase the concentration of the site concentration Fe^{2+}). The reduction obtained at the end of the process was 0.2 and consequently the τ should decrease of about 6 times, since the τ is inversely proportional to reduction degree (equation 5.15). After the treatment on the sample, the same measurement was performed and the results is reported in figure 5.10.

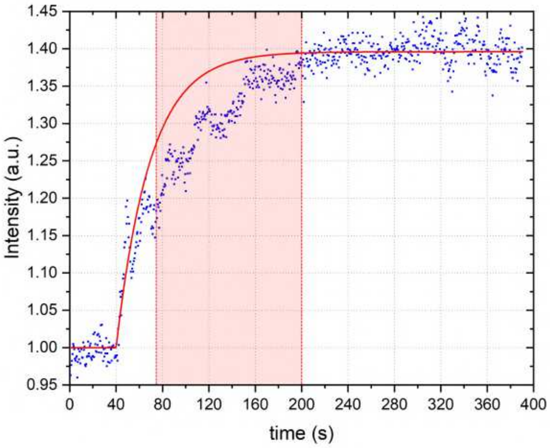

Figure 5.10. The graph represents the transmitted signal (i.e. Intensity in y-axis) throughout the waveguide, during a photoactuation by means of a green laser at $66\,\mathrm{mW}$. *The switching on time of the latter was at* $40\,\mathrm{s}$. *The iron doped cover features for this measurements were* $0.1\,\mathrm{mol}\,\%$ *of iron concentration and a reduction degree of* 0.2. *The red line represent the fitted curve of equation 5.27, where points from* $75\,\mathrm{s}$ *and* $200\,\mathrm{s}$ *were not considered.*

As showed by the data, the τ is decreased significantly from the previous case, in particular the time constant derived by the fit from all the data is $29.51 \pm 0.09\,\mathrm{s}$. The saturation transmitted intensity is decreased from $60\,\%$ to $40\,\%$, since the saturation value of the field is proportional only to the antisites concentration Fe^{3+}. However, this value is still enough for some optical applications, such as optical spectral filters [181], which require high contrast. The data still presents a low compatibility with the exponential behavior (i.e. the red function in figure 5.10) for $t > \tau$, especially for interval between $75\,\mathrm{s}$ and $200\,\mathrm{s}$. Nevertheless, the exponential description has still good agreement for $t << \tau$, but still the fit with small amounts of points does not give a precise estimation for τ. A precise estimation can still be obtains by means of a Taylor expansion of equation 5.27, taking the linear term for $t \to 0$:

$$\frac{\partial I}{\partial t}\Big|_{t\to 0} = \frac{I_{sat}}{\tau} \tag{5.28}$$

In particular, the analysis of τ is interesting since it is related to the intensity of the green light (equation 5.15). So, the photoactuation should be tuned by the change of I. The prove of this tunability is showed in figure 5.11, where several transmission signal from the waveguides are reported during a photoactuation with different green laser powers.

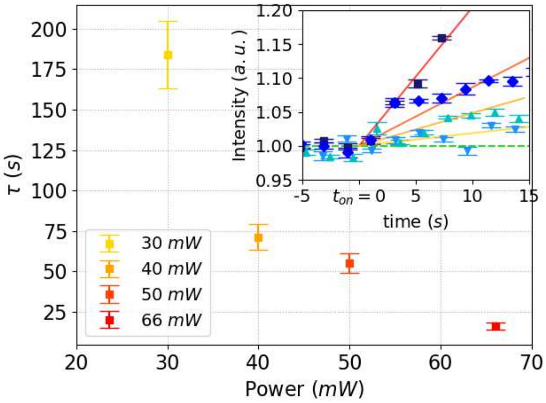

Figure 5.11. The red points represents τ values for the transmitted signal (i.e. Intensity in y-axis) at different power illuminations of green laser. The iron doped cover features for this measurements were $0.1\,\mathrm{mol}\,\%$ of iron concentration and a reduction degree of 0.2. The inset shows how these values are obtained from the linear interpolation of the transmitted signal, which are the points with different blue brightness.

The graph highlights the linearity of τ for a power range from 30 and $66\,\mathrm{mW}$, where τ is estimated, as showed in the inset, from the linear interpolation of time close to the switching on time. These results demonstrated how large is the range of time constants tunability, indeed, the device can increase its response time more than 7 times just using an attenuator of optical density 0.3 This improvement is due to the combination of two factors: the faster electric field growth, which has inversely proportionality with the green beam intensity (equation 5.15), and the simultaneous faster reaching of the threshold electric field for deeper layer of LCs in the field of view of the waveguided red beam. Therefore the temporal evolution of the waveguide signal is totally dominated by the intensity photoinduced field and its time dependence: this allows for a complete performances control of the optofluidic device (in terms of transmitted light intensity and polarization) solely by the tuning the compositional properties of Fe:LiNbO$_3$ cover.

These promising results show that deeper investigations on the tunability promoted by the material are necessary, in order to exploit all the potentialities offered by the device. In particular, the LCs orientations turning off and the general

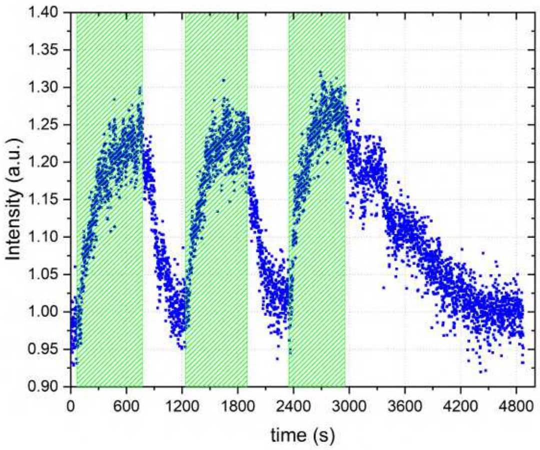

Figure 5.12. Transmitted signal of three consecutive photoactuations. The sample used was the same of figure 5.10. The lighting times are evidenced by the green regions, which are limited by the turning on times 70 s, 1240 s *and* 2350 s *and the turning off ones* 770 s, 1900 s *and* 2950 s.

reproducibility of the phenomenon are the future steps to be studied in details for a complete analysis of the system. In figure 5.12 an example of this feature is given. The same reduced sample of previous measurements was used and three consecutive photoactuations of the LCs were realized. As it is possible to notice, the same transmitted signal as well as the time constant of the LCs reorientation are highly reproducible, thus paving the way for the realization of an highly reusable optofluidic controller.

Conclusions and perspectives

Lab-on-a-chips are promising devices for a multitude applications, aimed to substitute operation typically done in laboratories in small platforms. The multidisciplinary research efforts are focused on the realization of few centimeters size devices, which can provide a wide and flexible toolkit. This work aimed to develop and prove the potentiality of lithium niobate as a substrate for such platforms.

The first part of this work was dedicated to the realization of microfluidic channels on lithium niobate: fabrication methods were investigated. Different techniques were explored in order to realize a microfluidic circuits on lithium niobate studying the drawbacks and advantages of each one, both the channels engraving and the sealing procedures. The optimal fabrication technique for microchannel was found to be the engraving by an self-polishing saw, which allows for an optical grade quality of channels walls in term of roughness, and thus, for optofluidic coupling. This quality was tested with both atomic force microscope and optical microscope. Regarding the sealing, three procedures show high compatibility with such a microfluidc structure, each one with advantages and drawbacks depending on the applications and the reconfigurability. The optimized microfabrication procedure can be exploited for the realization of several microfluidic circuits, in particular this work focused on two droplets generators configurations, a T-junction and a cross-junction. Both these microfluidic stages were characterized in details: the wettability, the capabilities in terms of droplet stability, the reproducibility and its performance. The water-in-oil droplets generation showed a frequency and volumes compatible with the well-known scaling laws, and a polydispersion better than $3\,\%$, which in agreement with the other standard material. This study demonstrated the feasibility of the realization of a microfluidic closed stage in lithium niobate.

In the second part, the optofluidic integration was presented between the microfluidic channel and waveguide on the same substrate of lithium niobate. Several techniques can be used for the waveguides realization in this material, since its famous exploitation in photonics. For optofluidic coupling with microchannel, the best technique is the Ti diffusion. The waveguides realized for this purpose were $5\,\mu\mathrm{m}$ wide Ti-indiffused, and they are designed to be monomode in the visible range propagation, since in several lab-on-a-chip application such a wavelength range is required. Each fabrication steps were deeply described: the photolitography, the sputtering of Ti, the lift off and the thermal diffusion. In particular the Ti diffusion inside $LiNbO_3$ was characterized by SIMS and RBS in order to study the optimal diffusion time to achieve a single mode waveguide. The waveguides were characterized by a near field analysis, which allowed for a transmission study of the losses and the output modes. The transmission losses achieved were on average $3\,\mathrm{dB\,cm^{-1}}$ for $632.8\,\mathrm{nm}$, which is compatible with standard of literature. The shape mode was studied in details for demonstrating the reproducibility of such a fabrication technique and for a future pigtailing coupling with optical fibers. An analysis of the mode symmetry was performed on more than 40 waveguides. Finally, the coupling with these waveguides and the microchannel were presented: the channels were engraved in a substrate with the waveguide, and the saw crossed the waveguides, in fact they were divided into parts.

The light from the first part crosses and illuminates the channel. The waveguide that acts a source therefore is called input waveguide. After being transmitted by the medium filling the channel, the light can couple into other part of the waveguide (output waveguide) on the other side of the channel, thus allowing for optical transmission analysis across the microchannel. Such a coupling is provided by the optical quality of the channel surface, and due to this feature it represents an unexplored way of coupling waveguides to microfluidic channel. It guarantees an self-alignment of the two waveguides, low transmission losses and a optical probing direct on the channel and with a local intrinsic nature. This local probe can be used for the measurements of flowing object in the channel or as simply transmission probe on the liquid inside the channel.

In the third part of this thesis several applications of this coupling were proposed. Firstly a novel optofluidic device was described, which aims to substitute the standard microscope and camera system for imaging. This device can, indeed, measure the frequency and the time interval of flowing objects in the channel by their optical transmission response, analyzed by the waveguides system. In particular, the system was tested with water-in-oil droplets, generated by an integrated T-junction, and the device showed a precision higher than standard setup, and a never reached level of integration. The droplets optical transmission signal gave also several geometrical information on the droplets shape, such as the volume and lengths. Moreover, a phenomelogical analysis of droplets generation led to a phenomenological scaling law on the lubrication film during the squeezing to dripping transition.

Another significant application proposed is the velocity measurements of objects flowing inside a microchannel, by changing slightly the structure of the waveguide with a Mach-Zehnder interferometer configuration. In particular, the coupling between this photonic structure and the channel allowed for a never achieved before precision on the direct measurements of velocity inside microchannel in a such integrated device. The system was based on a two reference points acting as optical triggers, but both can be analyzed by the same waveguided output, due to the peculiar photonic configuration.

Secondly, the waveguide transmission signal was exploited for a pH titration microfluidic operation, in order to neutralize an acidic or basic solution. The optofluidic substrate guarantees a continuous monitoring of the pH of a solution with a pH indicator inside the channel, which can be use as a feedback to control two flows of two opposite pH solutions for the chemical neutralization. The lithium niobate high chemical resistance allowed for its use of either high or low pH solutions, and thus this device achieved unique results, such as the neutralization of either HCl and NaOH solution in microfluidic channel and the simultaneous control. This simultaneous control can be further used for also pH measurements, exploiting different wavelength and pH indicators.

Thirdly, the flexibility in term of channel configuration was exploited for the realization of tilted channels respect to the waveguide, in order to control the refraction of the light inside the channel by the liquid optical properties. This microfluidic actuation on the light transmission was exploited for the realization of a stage, which can be considered as the first step for achieving a microfluidically actuated optical "multiplexer". Among an waveguides array, the output waveguide could be tuned by the optical properties of the liquid inside the microchannel, because of the refraction control inside the channel. The working principle was confirmed by air and water at a wavelength of $632.8\,\mathrm{nm}$, thus opening several future investigations on possible spectral filter application and other more sophisticated multiplexing operations tuning the uncertainty relation of the medium inside the channel.

All this promising applications showed the feasibility of a lab-on-a-chip based on a optofluidic driven $LiNbO_3$ substrate. These results represent only the first investigation on the potentialities of $LiNbO_3$ for optofluidic device, indeed the capabilities offered by this material properties can represent a breakthrough in the lab-on-a-chip technology. Among the others, the photovoltaic effect was already demonstrated to be optimal properties to generate electric field to manipulate microobjects. The last part of this work focused on the demonstration on the combination of a photovoltaic tweezers on the optofluidic device previously presented. A cover of lithium niobate doped with iron was implemented to the substrate with the microchannels and the waveguides, such a doping was realized to increase the capability of photoinduction of electric field on its substrate. In order to demonstrate the interaction of such a photoinduced electric field, this device was tested with liquid crystals, which can be oriented in the direction of the electric field. Their orientations were controlled by the electric field and it influenced the polarization optical transmission of the waveguide. In particular, this thesis showed how the electric field interaction power can be tuned by the compositional properties of the cover and the photoinducing laser intensity, depending on the needs of the applications.

In conclusion, this thesis is a first proof on the potentiality of monolithic lab-on-a-chip realized in lithium niobate. A well defined fabrication protocol was developed for the realization of an optofluidic coupling between microchannel and Ti-indiffused waveguides, which represents the main building block for several integrated devices in lab-on-a-chip technology and optofluidics. In both fields, this coupling was succesfully exploited for achieving novel interesting results. Moreover, the device was integrated with a photovoltaic tweezers, demonstrating the feasibility of a integration of a complete toolkit on the same $LiNbO_3$ substrate, exploiting its multiple properties. These promising results represent only the first step of a long and wide way to bring lithium niobate lab-on-a-chip inside to people pockets. However, the large variety and unique combination of properties of this material could be a breakthrough to pave the way for a revolution in this field.

Bibliography

[1] Mariano Jubera, I Elvira, A García-Cabañes, et al. “Trapping and patterning of biological objects using photovoltaic tweezers”. In: *Applied Physics Letters* 108.2 (2016), p. 023703.

[2] S Grilli, L Miccio, O Gennari, et al. “Active accumulation of very diluted biomolecules by nano-dispensing for easy detection below the femtomolar range”. In: *Nature communications* 5 (2014), p. 5314.

[3] Pietro Ferraro, Simonetta Grilli, Lisa Miccio, et al. “Wettability patterning of lithium niobate substrate by modulating pyroelectric effect to form microarray of sessile droplets”. In: *Applied Physics Letters* 92.21 (2008), p. 213107.

[4] David J Collins, Adrian Neild, and Ye Ai. “Highly focused high-frequency travelling surface acoustic waves (SAW) for rapid single-particle sorting”. In: *Lab on a Chip* 16.3 (2016), pp. 471–479.

[5] Annamaria Zaltron, Giacomo Bettella, Gianluca Pozza, et al. “Integrated optics on lithium niobate for sensing applications”. In: *Optical Sensors 2015*. Vol. 9506. International Society for Optics and Photonics. 2015, p. 950608.

[6] Giacomo Bettella, Gianluca Pozza, Sebastian Kroesen, et al. “Lithium niobate micromachining for the fabrication of microfluidic droplet generators”. In: *Micromachines* 8.6 (2017), p. 185.

[7] G Bettella, R Zamboni, G Pozza, et al. “LiNbO3 integrated system for opto-microfluidic sensing”. In: *Sensors and Actuators B: Chemical* 282 (2019), pp. 391–398.

[8] Nam-Trung Nguyen, Sumantri Lassemono, and Franck Alexis Chollet. “Optical detection for droplet size control in microfluidic droplet-based analysis systems”. In: *Sensors and actuators B: Chemical* 117.2 (2006), pp. 431–436.

[9] Carlo Liberale, G Cojoc, F Bragheri, et al. “Integrated microfluidic device for single-cell trapping and spectroscopy”. In: *Scientific reports* 3 (2013), p. 1258.

[10] Emanuel Weber, Dietmar Puchberger-Enengl, Franz Keplinger, et al. "In-line characterization and identification of micro-droplets on-chip". In: *Optofluidics, Microfluidics and Nanofluidics* 1.1 (2014).

[11] Yu-Wen Hsieh, An-Bang Wang, Xuan-Yi Lu, et al. "High-throughput on-line multi-detection for refractive index, velocity, size, and concentration measurements of micro-two-phase flow using optical microfibers". In: *Sensors and Actuators B: Chemical* 237 (2016), pp. 841–848.

[12] Casper Kunstmann-Olsen, Martin M Hanczyc, James Hoyland, et al. "Uniform droplet splitting and detection using Lab-on-Chip flow cytometry on a microfluidic PDMS device". In: *Sensors and Actuators B: Chemical* 229 (2016), pp. 7–13.

[13] PK Shivhare, A Prabhakar, and AK Sen. "Optofluidics based lab-on-chip device for in situ measurement of mean droplet size and droplet size distribution of an emulsion". In: *Journal of Micromechanics and Microengineering* 27.3 (2017), p. 035003.

[14] Xudong Fan and Ian M White. "Optofluidic microsystems for chemical and biological analysis". In: *Nature photonics* 5.10 (2011), p. 591.

[15] Sung Hwan Cho, Jessica M Godin, Chun-Hao Chen, et al. "Recent advancements in optofluidic flow cytometer". In: *Biomicrofluidics* 4.4 (2010), p. 043001.

[16] Yi-Chung Tung, Nien-Tsu Huang, Bo-Ram Oh, et al. "Optofluidic detection for cellular phenotyping". In: *Lab on a Chip* 12.19 (2012), pp. 3552–3565.

[17] Luis Arizmendi. "Photonic applications of lithium niobate crystals". In: *physica status solidi (a)* 201.2 (2004), pp. 253–283.

[18] Ka-Kha Wong. *Properties of lithium niobate*. 28. IET, 2002.

[19] S Grilli, L Miccio, V Vespini, et al. "Liquid micro-lens array activated by selective electrowetting on lithium niobate substrates". In: *Optics Express* 16.11 (2008), pp. 8084–8093.

[20] M Chauvet, L Al Fares, B Guichardaz, et al. "Integrated optofluidic index sensor based on self-trapped beams in LiNbO3". In: *Applied Physics Letters* 101.18 (2012), p. 181104.

[21] Michael Esseling, Annamaria Zaltron, Wolfgang Horn, et al. "Optofluidic droplet router". In: *Laser & Photonics Reviews* 9.1 (2015), pp. 98–104.

[22] Simonetta Grilli and Pietro Ferraro. "Dielectrophoretic trapping of suspended particles by selective pyroelectric effect in lithium niobate crystals". In: *Applied Physics Letters* 92.23 (2008), p. 232902.

[23] Angel García-Cabañes, Alfonso Blázquez-Castro, Luis Arizmendi, et al. "Recent achievements on photovoltaic optoelectronic tweezers based on lithium niobate". In: *Crystals* 8.2 (2018), p. 65.

[24] Barry E Jones. "Optical fibre sensors and systems for industry". In: *Journal of Physics E: Scientific Instruments* 18.9 (1985), p. 770.

[25] Demetri Psaltis, Stephen R Quake, and Changhuei Yang. "Developing optofluidic technology through the fusion of microfluidics and optics". In: *nature* 442.7101 (2006), p. 381.

[26] Aaron R Hawkins and Holger Schmidt. *Handbook of optofluidics*. CRC Press, 2010.

[27] Uriel Levy and Romi Shamai. "Tunable optofluidic devices". In: *Microfluidics and nanofluidics* 4.1-2 (2008), pp. 97–105.

[28] C Monat, P Domachuk, C Grillet, et al. "Optofluidics: a novel generation of reconfigurable and adaptive compact architectures". In: *Microfluidics and Nanofluidics* 4.1-2 (2008), pp. 81–95.

[29] Christelle Monat, P Domachuk, and BJ Eggleton. "Integrated optofluidics: A new river of light". In: *Nature photonics* 1.2 (2007), p. 106.

[30] Holger Schmidt and Aaron R Hawkins. "The photonic integration of non-solid media using optofluidics". In: *Nature photonics* 5.10 (2011), p. 598.

[31] Nam-Trung Nguyen. "Micro-optofluidic lenses: a review". In: *Biomicrofluidics* 4.3 (2010), p. 031501.

[32] Xudong Fan and Seok-Hyun Yun. "The potential of optofluidic biolasers". In: *Nature methods* 11.2 (2014), p. 141.

[33] Ruopeng Yan, Yunran Yang, Xin Tu, et al. "Optofluidic light routing via analytically configuring streamlines of microflow". In: *Microfluidics and Nanofluidics* 23.8 (2019), p. 101.

[34] Guangrui Li, Matthias Zeisberger, and Markus A Schmidt. "Guiding light in a water core all-solid cladding photonic band gap fiber–an innovative platform for fiber-based optofluidics". In: *Optics express* 25.19 (2017), pp. 22467–22479.

[35] Howard A Stone, Abraham D Stroock, and Armand Ajdari. "Engineering flows in small devices: microfluidics toward a lab-on-a-chip". In: *Annu. Rev. Fluid Mech.* 36 (2004), pp. 381–411.

[36] Dirk Janasek, Joachim Franzke, and Andreas Manz. "Scaling and the design of miniaturized chemical-analysis systems". In: *Nature* 442.7101 (2006), p. 374.

[37] Andréas Manz, N Graber, and H áM Widmer. “Miniaturized total chemical analysis systems: a novel concept for chemical sensing”. In: *Sensors and actuators B: Chemical* 1.1-6 (1990), pp. 244–248.

[38] Darwin R Reyes, Dimitri Iossifidis, Pierre-Alain Auroux, et al. “Micro total analysis systems. 1. Introduction, theory, and technology”. In: *Analytical chemistry* 74.12 (2002), pp. 2623–2636.

[39] Søren Balslev, AM Jorgensen, B Bilenberg, et al. “Lab-on-a-chip with integrated optical transducers”. In: *Lab on a Chip* 6.2 (2006), pp. 213–217.

[40] David Erickson, David Sinton, and Demetri Psaltis. “Optofluidics for energy applications”. In: *Nature Photonics* 5.10 (2011), p. 583.

[41] Yih-Fan Chen, Li Jiang, Matthew Mancuso, et al. “Optofluidic opportunities in global health, food, water and energy”. In: *Nanoscale* 4.16 (2012), pp. 4839–4857.

[42] Arthur Ashkin. “Acceleration and trapping of particles by radiation pressure”. In: *Physical review letters* 24.4 (1970), p. 156.

[43] Arthur Ashkin, James M Dziedzic, and T Yamane. “Optical trapping and manipulation of single cells using infrared laser beams”. In: *Nature* 330.6150 (1987), p. 769.

[44] Hamish C Hunt and James S Wilkinson. “Optofluidic integration for microanalysis”. In: *Microfluidics and Nanofluidics* 4.1-2 (2008), pp. 53–79.

[45] David G Grier. “A revolution in optical manipulation”. In: *nature* 424.6950 (2003), p. 810.

[46] Jeffrey R Moffitt, Yann R Chemla, Steven B Smith, et al. “Recent advances in optical tweezers”. In: *Annu. Rev. Biochem.* 77 (2008), pp. 205–228.

[47] Jesper Glückstad. “Microfluidics: Sorting particles with light”. In: *Nature Materials* 3.1 (2004), p. 9.

[48] Nicola Bellini, KC Vishnubhatla, F Bragheri, et al. “Femtosecond laser fabricated monolithic chip for optical trapping and stretching of single cells”. In: *Optics Express* 18.5 (2010), pp. 4679–4688.

[49] Jonathan Leach, Hasan Mushfique, Roberto di Leonardo, et al. “An optically driven pump for microfluidics”. In: *Lab on a Chip* 6.6 (2006), pp. 735–739.

[50] Armin Rauber. “Chemistry and physics of lithium niobate”. In: *Current topics in materials science* 1 (1978), pp. 481–601.

[51] Chihiro Koyama, Jun Nozawa, Kozo Fujiwara, et al. “Effect of point defects on Curie temperature of lithium niobate”. In: *Journal of the American Ceramic Society* 100.3 (2017), pp. 1118–1124.

[52] Uwe Schlarb and Klaus Betzler. “Refractive indices of lithium niobate as a function of temperature, wavelength, and composition: A generalized fit”. In: *Physical Review B* 48.21 (1993), p. 15613.

[53] E Bernal, GD Chen, and TC Lee. “Low frequency electro-optic and dielectric constants of lithium niobate”. In: *Physics Letters* 21.3 (1966), pp. 259–260.

[54] Ed L Wooten, Karl M Kissa, Alfredo Yi-Yan, et al. “A review of lithium niobate modulators for fiber-optic communications systems”. In: *IEEE Journal of selected topics in Quantum Electronics* 6.1 (2000), pp. 69–82.

[55] RS Weis and TK Gaylord. “Lithium niobate: summary of physical properties and crystal structure”. In: *Applied Physics A* 37.4 (1985), pp. 191–203.

[56] AM Glass, D von der Linde, and TJ Negran. “High-voltage bulk photovoltaic effect and the photorefractive process in LiNbO3”. In: *Landmark Papers On Photorefractive Nonlinear Optics*. World Scientific, 1995, pp. 371–373.

[57] Emmett N Leith and Juris Upatnieks. “Reconstructed wavefronts and communication theory”. In: *JOSA* 52.10 (1962), pp. 1123–1130.

[58] Bolin Fan, Feifei Li, Lipin Chen, et al. “Photovoltaic manipulation of water microdroplets on a hydrophobic LiNbO 3 substrate”. In: *Physical Review Applied* 7.6 (2017), p. 064010.

[59] P Ferraro, S Coppola, S Grilli, et al. “Dispensing nano–pico droplets and liquid patterning by pyroelectrodynamic shooting”. In: *Nature nanotechnology* 5.6 (2010), p. 429.

[60] DR Morgan. “Surface acoustic wave devices and applications: 1. Introductory review”. In: *Ultrasonics* 11.3 (1973), pp. 121–131.

[61] Trung Dung Luong and Nam Trung Nguyen. “Surface acoustic wave driven microfluidics-a review”. In: *Micro and Nanosystems* 2.3 (2010), pp. 217–225.

[62] Xiaoyun Ding, Peng Li, Sz-Chin Steven Lin, et al. “Surface acoustic wave microfluidics”. In: *Lab on a Chip* 13.18 (2013), pp. 3626–3649.

[63] Chia-Yen Lee, Chin-Lung Chang, Yao-Nan Wang, et al. “Microfluidic mixing: a review”. In: *International journal of molecular sciences* 12.5 (2011), pp. 3263–3287.

[64] Thomas Franke, Adam R Abate, David A Weitz, et al. “Surface acoustic wave (SAW) directed droplet flow in microfluidics for PDMS devices”. In: *Lab on a Chip* 9.18 (2009), pp. 2625–2627.

[65] Zhuochen Wang and Jiang Zhe. "Recent advances in particle and droplet manipulation for lab-on-a-chip devices based on surface acoustic waves". In: *Lab on a Chip* 11.7 (2011), pp. 1280–1285.

[66] Ghulam Destgeer and Hyung Jin Sung. "Recent advances in microfluidic actuation and micro-object manipulation via surface acoustic waves". In: *Lab on a Chip* 15.13 (2015), pp. 2722–2738.

[67] Richie J Shilton, Marco Travagliati, Fabio Beltram, et al. "Microfluidic pumping through miniaturized channels driven by ultra-high frequency surface acoustic waves". In: *Applied Physics Letters* 105.7 (2014), p. 074106.

[68] George M Whitesides. "The origins and the future of microfluidics". In: *Nature* 442.7101 (2006), p. 368.

[69] Shia-Yen Teh, Robert Lin, Lung-Hsin Hung, et al. "Droplet microfluidics". In: *Lab on a Chip* 8.2 (2008), pp. 198–220.

[70] Jako Greuters and Nadeem Hasan Rizvi. "UV laser micromachining of silicon, indium phosphide, and lithium niobate for telecommunications applications". In: *Opto-Ireland 2002: Optics and Photonics Technologies and Applications*. Vol. 4876. International Society for Optics and Photonics. 2003, pp. 479–486.

[71] Rafael R Gattass and Eric Mazur. "Femtosecond laser micromachining in transparent materials". In: *Nature photonics* 2.4 (2008), p. 219.

[72] Roberto Osellame, Giulio Cerullo, and Roberta Ramponi. *Femtosecond laser micromachining: photonic and microfluidic devices in transparent materials*. Vol. 123. Springer Science & Business Media, 2012.

[73] Jintian Lin, Yingxin Xu, Zhiwei Fang, et al. "Fabrication of high-Q lithium niobate microresonators using femtosecond laser micromachining". In: *Scientific reports* 5 (2015), p. 8072.

[74] A Malshe, D Deshpande, E Stach, et al. "Investigation of femtosecond laser-assisted micromachining of lithium niobate". In: *CIRP Annals* 53.1 (2004), pp. 187–190.

[75] Manoj Sridhar, Devendra K Maurya, James R Friend, et al. "Focused ion beam milling of microchannels in lithium niobate". In: *Biomicrofluidics* 6.1 (2012), p. 012819.

[76] Stephen Winnall and Saul Winderbaum. *Lithium niobate reactive ion etching*. Tech. rep. DEFENCE SCIENCE and TECHNOLOGY ORGANIZATION SALISBURY (AUSTRALIA), 2000.

[77] Zeyad Yousif Abdoon Al-Shibaany, John Hedley, Dehong Huo, et al. "Micromachining lithium niobate for rapid prototyping of resonant biosensors". In: *IOP Conference Series: Materials Science and Engineering*. Vol. 65. 1. IOP Publishing. 2014, p. 012030.

[78] Dehong Huo, Zi Jie Choong, Yilun Shi, et al. “Diamond micro-milling of lithium niobate for sensing applications”. In: *Journal of Micromechanics and Microengineering* 26.9 (2016), p. 095005.

[79] Ryo Takigawa, Eiji Higurashi, Tetsuya Kawanishi, et al. “Lithium niobate ridged waveguides with smooth vertical sidewalls fabricated by an ultra-precision cutting method”. In: *Optics express* 22.22 (2014), pp. 27733–27738.

[80] Mathieu Chauvet, Fabien Henrot, Florent Bassignot, et al. “High efficiency frequency doubling in fully diced LiNbO3 ridge waveguides on silicon”. In: *Journal of Optics* 18.8 (2016), p. 085503.

[81] Luai Al Fares, Fabrice Devaux, Blandine Guichardaz, et al. “Self-trapped beams crossing tilted channels to induce guided polarization separators”. In: *Applied Physics Letters* 103.4 (2013), p. 041111.

[82] RWRL Gajasinghe, SU Senveli, S Rawal, et al. “Experimental study of PDMS bonding to various substrates for monolithic microfluidic applications”. In: *Journal of Micromechanics and Microengineering* 24.7 (2014), p. 075010.

[83] Dhananjay Bodas and Chantal Khan-Malek. “Formation of more stable hydrophilic surfaces of PDMS by plasma and chemical treatments”. In: *Microelectronic engineering* 83.4-9 (2006), pp. 1277–1279.

[84] Sean M Langelier, Leslie Y Yeo, and James Friend. “UV epoxy bonding for enhanced SAW transmission and microscale acoustofluidic integration”. In: *Lab on a Chip* 12.16 (2012), pp. 2970–2976.

[85] Jan A Dziuban. *Bonding in microsystem technology*. Vol. 24. Springer Science & Business Media, 2007.

[86] Andreas Plößl and Gertrud Kräuter. “Wafer direct bonding: tailoring adhesion between brittle materials”. In: *Materials Science and Engineering: R: Reports* 25.1-2 (1999), pp. 1–88.

[87] Marin Alexe and Ulrich Gösele. *Wafer bonding: applications and technology*. Vol. 75. Springer Science & Business Media, 2013.

[88] KM Knowles and ATJ Van Helvoort. “Anodic bonding”. In: *International materials reviews* 51.5 (2006), pp. 273–311.

[89] Hsueh-An Yang, Mingching Wu, and Weileun Fang. “Localized induction heating solder bonding for wafer level MEMS packaging”. In: *Journal of Micromechanics and Microengineering* 15.2 (2004), p. 394.

[90] Yu-Ting Cheng, Liwei Lin, and Khalil Najafi. “Localized silicon fusion and eutectic bonding for MEMS fabrication and packaging”. In: *Journal of Microelectromechanical Systems* 9.1 (2000), pp. 3–8.

[91] D Tulli, D Janner, and V Pruneri. “Room temperature direct bonding of LiNbO3 crystal layers and its application to high-voltage optical sensing”. In: *Journal of Micromechanics and Microengineering* 21.8 (2011), p. 085025.

[92] Giacomo Bettella. “Integrated opto-microfluidic lab-on-a-chip in lithium niobate for droplet generation and sensing”. PhD thesis. University of Padova, Physics and Astronomy Department ‘Galileo Galilei’, 2016.

[93] Jonathan Bennès, Sylvain Ballandras, and Frederic Cherioux. “Easy and versatile functionalization of lithium niobate wafers by hydrophobic trichlorosilanes”. In: *Applied Surface Science* 255.5 (2008), pp. 1796–1800.

[94] Sneha A Kulkarni, Satishchandra B Ogale, and Kunjukrishanan P Vijayamohanan. “Tuning the hydrophobic properties of silica particles by surface silanization using mixed self-assembled monolayers”. In: *Journal of Colloid and Interface Science* 318.2 (2008), pp. 372–379.

[95] Simone Silvestrini, Davide Ferraro, Tamara Tóth, et al. “Tailoring the wetting properties of thiolene microfluidic materials”. In: *Lab on a Chip* 12.20 (2012), pp. 4041–4043.

[96] Pingan Zhu and Liqiu Wang. “Passive and active droplet generation with microfluidics: a review”. In: *Lab on a Chip* 17.1 (2017), pp. 34–75.

[97] Zhuang Zhi Chong, Shu Beng Tor, Ngiap Hiang Loh, et al. “Acoustofluidic control of bubble size in microfluidic flow-focusing configuration”. In: *Lab on a Chip* 15.4 (2015), pp. 996–999.

[98] Darren R Link, Erwan Grasland-Mongrain, Agnes Duri, et al. “Electric control of droplets in microfluidic devices”. In: *Angewandte Chemie International Edition* 45.16 (2006), pp. 2556–2560.

[99] Patrick Tabeling. *Introduction to microfluidics*. OUP Oxford, 2005.

[100] Nam-Trung Nguyen, Steven T Wereley, and Seyed Ali Mousavi Shaegh. *Fundamentals and applications of microfluidics*. Artech house, 2019.

[101] Gordon F Christopher and Shelly L Anna. “Microfluidic methods for generating continuous droplet streams”. In: *Journal of Physics D: Applied Physics* 40.19 (2007), R319.

[102] Gordon F Christopher, N Nadia Noharuddin, Joshua A Taylor, et al. “Experimental observations of the squeezing-to-dripping transition in T-shaped microfluidic junctions”. In: *Physical Review E* 78.3 (2008), p. 036317.

[103] Nathalie Tarchichi, Franck Chollet, and Jean-François Manceau. “New regime of droplet generation in a T-shape microfluidic junction”. In: *Microfluidics and nanofluidics* 14.1-2 (2013), pp. 45–51.

[104] Junfeng Zhang. “Lattice Boltzmann method for microfluidics: models and applications”. In: *Microfluidics and Nanofluidics* 10.1 (2011), pp. 1–28.

[105] Todd Thorsen, Richard W Roberts, Frances H Arnold, et al. "Dynamic pattern formation in a vesicle-generating microfluidic device". In: *Physical review letters* 86.18 (2001), p. 4163.

[106] Piotr Garstecki, Michael J Fuerstman, Howard A Stone, et al. "Formation of droplets and bubbles in a microfluidic T-junction scaling and mechanism of break-up". In: *Lab on a Chip* 6.3 (2006), pp. 437–446.

[107] M De Menech, P Garstecki, F Jousse, et al. "Transition from squeezing to dripping in a microfluidic T-shaped junction". In: *journal of fluid mechanics* 595 (2008), pp. 141–161.

[108] Howard A Stone. "On lubrication flows in geometries with zero local curvature". In: *Chemical engineering science* 60.17 (2005), pp. 4838–4845.

[109] Volkert van Steijn, Chris R Kleijn, and Michiel T Kreutzer. "Predictive model for the size of bubbles and droplets created in microfluidic T-junctions". In: *Lab on a Chip* 10.19 (2010), pp. 2513–2518.

[110] Riccardo Zamboni. *Caratterizzazione microfluidica di un generatore di gocce a T-junction integrato in niobato di litio*. 2014.

[111] Adrian Daerr and Adrien Mogne. "Pendent-drop: an imagej plugin to measure the surface tension from an image of a pendent drop". In: *Journal of Open Research Software* 4.1 (2016).

[112] Ran Li, Isao Kobayashi, Yanru Zhang, et al. "Preparation of monodisperse W/O emulsions using a stainless-steel microchannel emulsification chip". In: *Particulate Science and Technology* 37.1 (2019), pp. 68–73.

[113] Evandro Piccin, Davide Ferraro, Paolo Sartori, et al. "Generation of water-in-oil and oil-in-water microdroplets in polyester-toner microfluidic devices". In: *Sensors and Actuators B: Chemical* 196 (2014), pp. 525–531.

[114] Lei Zhang, Wei Wang, Xiao-Jie Ju, et al. "Fabrication of glass-based microfluidic devices with dry film photoresists as pattern transfer masks for wet etching". In: *RSC Advances* 5.8 (2015), pp. 5638–5646.

[115] JH Xu, SW Li, J Tan, et al. "Preparation of highly monodisperse droplet in a T-junction microfluidic device". In: *AIChE journal* 52.9 (2006), pp. 3005–3010.

[116] Thomas Cubaud and Thomas G Mason. "Capillary threads and viscous droplets in square microchannels". In: *Physics of Fluids* 20.5 (2008), p. 053302.

[117] J Tan, JH Xu, SW Li, et al. "Drop dispenser in a cross-junction microfluidic device: Scaling and mechanism of break-up". In: *Chemical Engineering Journal* 136.2-3 (2008), pp. 306–311.

[118] Taotao Fu, Yining Wu, Youguang Ma, et al. "Droplet formation and breakup dynamics in microfluidic flow-focusing devices: from dripping to jetting". In: *Chemical engineering science* 84 (2012), pp. 207–217.

[119] Stéphanie Van Loo, Serguei Stoukatch, Michael Kraft, et al. "Droplet formation by squeezing in a microfluidic cross-junction". In: *Microfluidics and Nanofluidics* 20.10 (2016), p. 146.

[120] Xiaoming Chen, Tomasz Glawdel, Naiwen Cui, et al. "Model of droplet generation in flow focusing generators operating in the squeezing regime". In: *Microfluidics and Nanofluidics* 18.5-6 (2015), pp. 1341–1353.

[121] Haihu Liu and Yonghao Zhang. "Droplet formation in microfluidic cross-junctions". In: *Physics of Fluids* 23.8 (2011), p. 082101.

[122] Ali Lashkaripour, Christopher Rodriguez, Luis Ortiz, et al. "Performance tuning of microfluidic flow-focusing droplet generators". In: *Lab on a Chip* 19.6 (2019), pp. 1041–1053.

[123] Peter Friis, Karsten Hoppe, Otto Leistiko, et al. "Monolithic integration of microfluidic channels and optical waveguides in silica on silicon". In: *Applied optics* 40.34 (2001), pp. 6246–6251.

[124] Klaus B Mogensen, Jamil El-Ali, Anders Wolff, et al. "Integration of polymer waveguides for optical detection in microfabricated chemical analysis systems". In: *Applied Optics* 42.19 (2003), pp. 4072–4079.

[125] M Khoury, Christoph Vannahme, Kristian Tølbøl Sørensen, et al. "Monolithic integration of DUV-induced waveguides into plastic microfluidic chip for optical manipulation". In: *Microelectronic Engineering* 121 (2014), pp. 5–9.

[126] Jonathan T Butement, Hamish C Hunt, David J Rowe, et al. "Integrated optical waveguides and inertial focussing microfluidics in silica for microflow cytometry applications". In: *Journal of Micromechanics and Microengineering* 26.10 (2016), p. 105004.

[127] Marco Bazzan and Cinzia Sada. "Optical waveguides in lithium niobate: Recent developments and applications". In: *Applied Physics Reviews* 2.4 (2015), p. 040603.

[128] MN Armenise. "Fabrication techniques of lithium niobate waveguides". In: *IEE Proceedings J (Optoelectronics)* 135.2 (1988), pp. 85–91.

[129] G Griffiths and R Esdaile. "Analysis of titanium diffused planar optical waveguides in lithium niobate". In: *IEEE Journal of Quantum electronics* 20.2 (1984), pp. 149–159.

[130] R Alferness, V Ramaswamy, S Korotky, et al. "Efficient single-mode fiber to titanium diffused lithium niobate waveguide coupling for λ= 1.32 μm". In: *IEEE Journal of Quantum Electronics* 18.10 (1982), pp. 1807–1813.

[131] Ovidio Peña-Rodríguez, José Olivares, Mercedes Carrascosa, et al. "Optical waveguides fabricated by ion implantation/irradiation: A review". In: *Ion implantation* (2012), pp. 267–314.

[132] Masaharu Fukuma, Juichi Noda, and Hiroshi Iwasaki. "Optical properties in titanium-diffused LiNbO3 strip waveguides". In: *Journal of Applied Physics* 49.7 (1978), pp. 3693–3698.

[133] S Fouchet, Alain Carenco, C Daguet, et al. "Wavelength dispersion of Ti induced refractive index change in LiNbO 3 as a function of diffusion parameters". In: *Journal of Lightwave Technology* 5.5 (1987), pp. 700–708.

[134] LV Ioganson. "THEORY OF RESONANT ELECTROMAGNETIC SYSTEMS WITH TOTAL INTERNAL REFLECTION. 3." In: *SOVIET PHYSICS TECHNICAL PHYSICS-USSR* 11.11 (1967), p. 1529.

[135] PK Tien and R Ulrich. "Theory of prism–film coupler and thin-film light guides". In: *JOSA* 60.10 (1970), pp. 1325–1337.

[136] JH Harris and R Shubert. "Variable tunneling excitation of optical surface waves". In: *IEEE Transactions on microwave theory and techniques* 19.3 (1971), pp. 269–276.

[137] CH Bulmer, SK Sheem, RP Moeller, et al. "High-efficiency flip-chip coupling between single-mode fibers and LiNbO3 channel waveguides". In: *Applied Physics Letters* 37.4 (1980), pp. 351–353.

[138] E Murphy, T Rice, Leon McCaughan, et al. "Permanent attachment of single-mode fiber arrays to waveguides". In: *Journal of lightwave technology* 3.4 (1985), pp. 795–799.

[139] JM Hammer, RA Bartolini, A Miller, et al. "Optical grating coupling between low-index fibers and high-index film waveguides". In: *Applied Physics Letters* 28.4 (1976), pp. 192–194.

[140] C Bulmer and M Wilson. "Single mode grating coupling between thin-film and fiber optical waveguides". In: *IEEE Journal of Quantum Electronics* 14.10 (1978), pp. 741–749.

[141] PK Tien, G Smolinsky, and RJ Martin. "Radiation fields of a tapered film and a novel film-to-fiber coupler". In: *IEEE Transactions on Microwave Theory and Techniques* 23.1 (1975), pp. 79–85.

[142] GA Teh and George I Stegeman. "Coupling from a thin film to an optical fiber". In: *Applied optics* 17.16 (1978), pp. 2483–2484.

[143] SC Gupta. *Optoelectronic Devices and Systems*. PHI Learning Pvt. Ltd., 2014.

[144] Fernanda Irrera and Marco Valli. "Characterization of planar Ti: LiNbO3 optical waveguides in the visible and near-infrared spectral range". In: *Journal of applied physics* 64.4 (1988), pp. 1704–1708.

[145] Sedat Nizamoglu, Kyung-Bok Lee, Malte C Gather, et al. "A simple approach to biological single-cell lasers via intracellular dyes". In: *Advanced Optical Materials* 3.9 (2015), pp. 1197–1200.

[146] Petra S Dittrich and Andréas Manz. "Lab-on-a-chip: microfluidics in drug discovery". In: *Nature reviews Drug discovery* 5.3 (2006), p. 210.

[147] Pascale Aussillous and David Quéré. "Quick deposition of a fluid on the wall of a tube". In: *Physics of fluids* 12.10 (2000), pp. 2367–2371.

[148] LK Chin, AQ Liu, YC Soh, et al. "A reconfigurable optofluidic Michelson interferometer using tunable droplet grating". In: *Lab on a Chip* 10.8 (2010), pp. 1072–1078.

[149] Michael Ian Lapsley, I-Kao Chiang, Yue Bing Zheng, et al. "A single-layer, planar, optofluidic Mach–Zehnder interferometer for label-free detection". In: *Lab on a Chip* 11.10 (2011), pp. 1795–1800.

[150] Andrea Crespi, Yu Gu, Bongkot Ngamsom, et al. "Three-dimensional Mach-Zehnder interferometer in a microfluidic chip for spatially-resolved label-free detection". In: *Lab on a Chip* 10.9 (2010), pp. 1167–1173.

[151] BJ Luff, James S Wilkinson, Jacob Piehler, et al. "Integrated optical mach-zehnder biosensor". In: *Journal of lightwave technology* 16.4 (1998), p. 583.

[152] Francisco Prieto, Borja Sepúlveda, A Calle, et al. "Integrated Mach–Zehnder interferometer based on ARROW structures for biosensor applications". In: *Sensors and actuators B: Chemical* 92.1-2 (2003), pp. 151–158.

[153] WK Burns, RP Moeller, CH Bulmer, et al. "Optical waveguide channel branches in Ti-diffused LiNbO 3". In: *Applied optics* 19.17 (1980), pp. 2890–2896.

[154] Masayuki Izutsu, Yoshiharu Nakai, and Tadasi Sueta. "Operation mechanism of the single-mode optical-waveguide Y junction". In: *Optics letters* 7.3 (1982), pp. 136–138.

[155] R Baets and PE Lagasse. "Calculation of radiation loss in integrated-optic tapers and Y-junctions". In: *Applied optics* 21.11 (1982), pp. 1972–1978.

[156] R Baets and PE Lagasse. "Loss calculation and design of arbitrarily curved integrated-optic waveguides". In: *JOSA* 73.2 (1983), pp. 177–182.

[157] W Burns and A Milton. "An analytic solution for mode coupling in optical waveguide branches". In: *IEEE Journal of Quantum Electronics* 16.4 (1980), pp. 446–454.

[158] H Sasaki and N Mikoshiba. "Normalised power transmission in single mode optical branching waveguides". In: *Electronics Letters* 17.3 (1981), pp. 136–138.

[159] Riccardo Zamboni. *Optofluidic application of a Mach-Zehnder interferometer integrated in lithium niobate for droplet sensing*. 2016.

[160] Adrien Bussonnière, Yannick Miron, Michaël Baudoin, et al. "Cell detachment and label-free cell sorting using modulated surface acoustic waves (SAWs) in droplet-based microfluidics". In: *Lab on a Chip* 14.18 (2014), pp. 3556–3563.

[161] NV Kukhtarev, VB Markov, SG Odulov, et al. "The physics and applications of photorefractive materials". In: *Ferroelectrics* 22 (1979), p. 949.

[162] Peter Günter, Jean-Pierre Huignard, and Alastair M Glass. *Photorefractive materials and their applications*. Vol. 1. Springer, 1988.

[163] R Orlowski and E Krätzig. "Holographic method for the determination of photo-induced electron and hole transport in electro-optic crystals". In: *Solid State Communications* 27.12 (1978), pp. 1351–1354.

[164] Annamaria Zaltron. "Local doping of lithium niobate by iron diffusion: a study of photorefractive properties". PhD thesis. University of Padova, Physics and Astronomy Department 'Galileo Galilei', 2011.

[165] JL Carns, G Cook, MA Saleh, et al. "Photovoltaic field-induced self-phase modulation of light in liquid crystal cells". In: *Molecular Crystals and Liquid Crystals* 453.1 (2006), pp. 83–92.

[166] Jennifer L Carns, Gary Cook, Mohammad A Saleh, et al. "Self-activated liquid-crystal cells with photovoltaic substrates". In: *Optics letters* 31.7 (2006), pp. 993–995.

[167] L Lucchetti, K Kushnir, A Zaltron, et al. "Light controlled phase shifter for optofluidics". In: *Optics letters* 41.2 (2016), pp. 333–335.

[168] L Lucchetti, K Kushnir, V Reshetnyak, et al. "Light-induced electric field generated by photovoltaic substrates investigated through liquid crystal reorientation". In: *Optical Materials* 73 (2017), pp. 64–69.

[169] Alexander Lorenz, Lin Jiao, and Dean R Evans. "Photovoltaic light valving induced in a vertically aligned nematic liquid crystal on a x-cut Fe: LiNbO3 substrate". In: *Optical Data Processing and Storage* 4.1 (2018), pp. 8–13.

[170] Silvio Bonfadini, Fabrizio Ciciulla, Luigino Criante, et al. "Optofluidic platform using liquid crystals in lithium niobate microchannel". In: *Scientific reports* 9.1 (2019), p. 1062.

[171] George William Gray, Kenneth J Harrison, and JA Nash. "New family of nematic liquid crystals for displays". In: *Electronics Letters* 9.6 (1973), pp. 130–131.

[172] PP Karat and NV Madhusudana. “Elastic and optical properties of some 4´n-alkyl-4-cyanobiphenyls”. In: *Molecular Crystals and Liquid Crystals* 36.1-2 (1976), pp. 51–64.

[173] Georges Friedel. “Les états mésomorphes de la matière”. In: *Annales de physique*. Vol. 9. 1922, pp. 273–474.

[174] Pierre-Gilles De Gennes and Jacques Prost. *The physics of liquid crystals*. Vol. 83. Oxford university press, 1995.

[175] Anupam Sengupta, Stephan Herminghaus, and Christian Bahr. “Liquid crystal microfluidics: surface, elastic and viscous interactions at microscales”. In: *Liquid Crystals Reviews* 2.2 (2014), pp. 73–110.

[176] Denis Andrienko. “Introduction to liquid crystals”. In: *Journal of Molecular Liquids* 267 (2018), pp. 520–541.

[177] R Clark Jones. “A new calculus for the treatment of optical systemsi. description and discussion of the calculus”. In: *Josa* 31.7 (1941), pp. 488–493.

[178] A Rastegar, M Škarabot, B Blij, et al. “Mechanism of liquid crystal alignment on submicron patterned surfaces”. In: *Journal of Applied Physics* 89.2 (2001), pp. 960–964.

[179] Anupam Sengupta, Benjamin Schulz, Elena Ouskova, et al. “Functionalization of microfluidic devices for investigation of liquid crystal flows”. In: *Microfluidics and nanofluidics* 13.6 (2012), pp. 941–955.

[180] Anupam Sengupta, Uroš Tkalec, Miha Ravnik, et al. “Liquid crystal microfluidics for tunable flow shaping”. In: *Physical review letters* 110.4 (2013), p. 048303.

[181] JG Cuennet, Andreas E Vasdekis, and D Psaltis. “Optofluidic-tunable color filters and spectroscopy based on liquid-crystal microflows”. In: *Lab on a Chip* 13.14 (2013), pp. 2721–2726.

Acknowledgments

I wish to acknowledge the people who helped me during these years and for the realization of this work. Firstly, I would like to thank my supervisor Cinzia Sada for giving me the possibility of the realization of this project and for her continuous support without denying any of mine autonomous idea. Secondly, a special thank is due to Mathieu Chauvet for the stimulating collaboration and for the precious opportunity of spending 6 months in FEMTO-ST.

I also want to thanks a lot Annamaria Zaltron, Giacomo Bettella and Gianluca Pozza, who introduce me to the laboratory work and for every precious suggestions and advises. I would like to acknowledge my family for the support during all my formation years.

I acknowledge all the students I followed during their thesis, and I hope them for a bright future. I'd like to thank all the Lafsi group for their precious answer to my numerous question about microfluidic. I would like to acknowledge all the technical supports provided by Luca Bacci, Nicola Argiolas and Ludovic Manuel Gauthier. Finally, I would like to thank all the Matter Physics group for the helpful discussion.

Last but not least, the acknowledgments have to be done to the all the people, that spent time in the room ”111” for the moral supports, and to all the kind people from FEMTO-ST that make known Besancon and spent joyful time together. Finally, I would like to thank all the ”TAVERNA” boys and all the people that help me for relieving the stress of these three years with some beers and laughs together.